Measurement of Turbulence-driven Reynolds Stress and Its Contribution to the Toroidal Intrinsic Rotation

by

Xijie Qin

A dissertation submitted in partial fulfillment of
the requirements for the degree of

Doctor of Philosophy

(Nuclear Engineering and Engineering Physics)

at the

UNIVERSITY OF WISCONSIN–MADISON

2024

Date of final oral examination: 03/15/2024

This report is reviewed by the Final Oral Examination Committee:

Benedikt Geiger, Professor, Nuclear Engineering and Engineering Physics
George McKee, Senior Scientist, Nuclear Engineering and Engineering Physicss
Raymond Fonck, Professor Emeritus, Nuclear Engineering and Engineering Physicss
Chris Hegna, Professor, Nuclear Engineering and Engineering Physics
Paul Terry, Professor, Physics
Cary Forest, Professor, Physics

ACKNOWLEDGMENTS

This dissertation marks the conclusion of a journey spanning over six and a half years, across two countries, and through a difficult period due to the pandemic. It would have been impossible for me to complete it without help from many people. First, I would like to express my gratitude to my advisors, George McKee, Benedikt Geiger, and Raymond Fonck, for their unwavering support, insightful feedback, and invaluable mentorship throughout this research journey.

Ray was my undergraduate advisor more than 10 years ago. He taught me with patience and attention, inspired my initial interest in fusion science, and generously provided opportunities for further study in graduate school. To this day, he continues to assist me in refining my research on intrinsic rotation, helps me with writing and presenting, and occasionally shares fun stories with me.

Following Ray's retirement, Benedikt graciously took me under his wing. He is a conscientious and responsible advisor, always offering help promptly, guiding my research direction, planning my graduation, and patiently revising my thesis and papers. He cares for his students; after I strained my back, he added a yoga ball to our office, which quickly became a favorite among the four of us and other office regulars.

Meeting George might be the best thing that happened to me in graduate school. He supported me in all aspects of my research, allowed me to choose the topics that aligned with my interests, and dedicated himself to providing guidance while granting me autonomy and the freedom to plan my work. I admire his serious attitude toward research and am deeply moved by his care for students. Words cannot fully express my gratitude to George; I aspire to one day become a researcher like him.

In addition to my three advisors, I received tremendous support from my colleagues and other scientists. Matt Kriete and Dinh Truong com-

ABSTRACT

Self-generated toroidal flow due to turbulent Reynolds stress is important in fusion plasmas since rotation and its shear improve confinement and stability. This study reports the first measurement of the turbulent Reynolds stress in fusion-grade plasma cores via correlated density and velocity fluctuations in the DIII-D tokamak. Experiments are conducted with both co- and counter-current Neutral Beam Injection (NBI) to control the net torque input and achieve a near-zero flat rotation profile. Electron Cyclotron Heating (ECH) is applied to alter the ion and electron heat fluxes and therefore the mixture of turbulence modes. High-quality fluctuation measurements are obtained via Beam Emission Spectroscopy (BES) and Ultra-Fast Charge Exchange Recombination Spectroscopy (UFCHERS). Following the application of ECH, the toroidal rotation reverses from counter-current to co-current direction, and the turbulence instability shifts from dominant electron modes to a mixture of electron and ion modes. Residual stress is extracted from the measured toroidal Reynolds stress, and the resulting intrinsic torque is determined. During the NBI-only stage, the volume-integrated intrinsic torque is nearly zero. Upon the application of ECH, a strong rotation drive is identified at the plasma edge, resulting in a net co-current intrinsic torque of 0.40 ± 0.05 Nm, which is comparable to the -0.75 Nm counter-current NBI torque. The toroidal rotation profiles reconstructed using the inferred intrinsic torques align well with experimental observations, successfully reproducing the rotation changes with the application of ECH. These results provide valuable insights into the relationship between turbulence and plasma rotation, demonstrate convincing consistency with the theory of turbulence-driven intrinsic torque, and support the use of turbulence models to predict rotation profiles for future magnetic fusion facilities like ITER.

CONTENTS

1   INTRODUCTION

1.1   Fusion Energy and Tokamaks

Based on the forecasts of population and economic growth for different regions of the world, an estimation was made by the International Atomic Energy Agency (IAEA) in the early 90s for global energy consumption in the years 2000, 2020, and 2060. In the estimated scenario with medium Gross Domestic Product (GDP) growth, electricity generation capacity in 2020 will increase to 6590 GW at an annual growth rate of 3% [1]. Concerns about the rapidly rising energy demand appear justified. Data and statistics collected by the International Energy Agency (IEA) indicate that in 2020, the global electricity generation reached 7800 GW, with an annual growth rate of 3.6% since 1990 [2].

Despite the large global fossil fuel reserves, it is possible to anticipate stock shortages and increasing mining costs in the near future. At the same time, the expansion of other energy sources faces various limitations. The hydroelectric capacity is affected by geographic environmental conditions and is expected to have an expansion factor of less than 3. The biomass is mainly limited by its heavy demand for productive land. Renewable energy sources such as solar and wind occupy considerable space and are strongly influenced by geographic and seasonal factors. The large-scale usage of nuclear fission power is motivated by the significant reduction of domestic fossil fuel production in many developed countries but also brings problems like long-lasting nuclear waste and public concerns about the potential risk of reactor accidents and radiation leakage.

Researchers suggested that desirable energy sources in the 21st century should depend on several factors besides the longevity and magnitude of the reserves. These factors are the commercial cost of the energy, the environmental cost to humanity in waste production, airborne pollutants,

accidents, and consumption of land, the geographical availability, and the relation to military hardware [1]. The limitations on traditional fossil fuel, hydroelectric energy, and nuclear fission power motivate the development of a new energy source, fusion. Fusion offers abundant fuel supplies, zero greenhouse gas emissions, minimal land requirement, significantly reduced risk of major radioactivity incidents, and reliable power generation against geographic and seasonal factors.
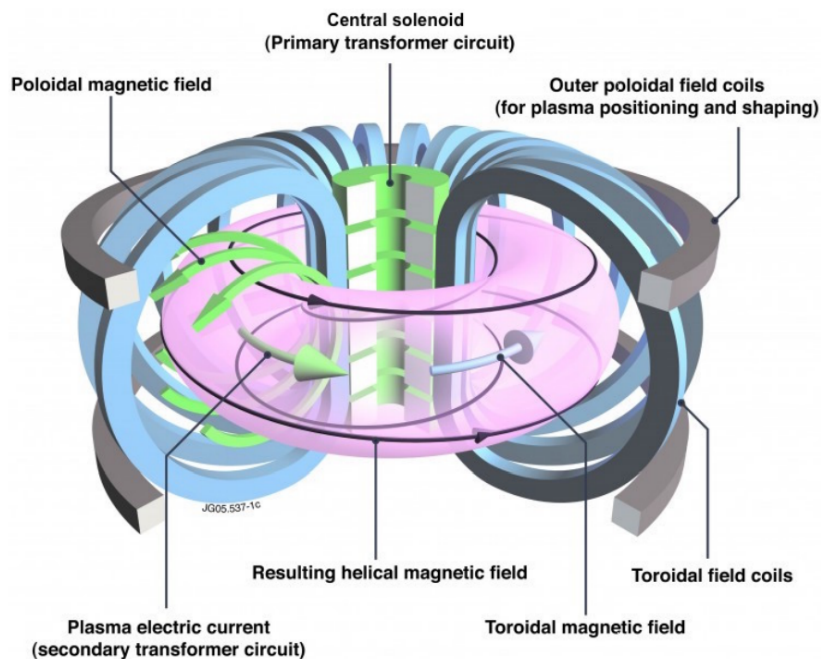
Figure 1.1: Tokamak magnetic field structure and major magnets [3].

The capability of producing a significant amount of thermal fusion power under controlled nuclear fusion was demonstrated in the 1990s by the US Tokamak Fusion Test Reactor (TFTR) and the Joint European Torus (JET) experiments [5]. The goal of achieving net energy gain and demonstrating the feasibility of fusion as a new energy source is pursued by the International Thermonuclear Experimental Reactor (ITER), which
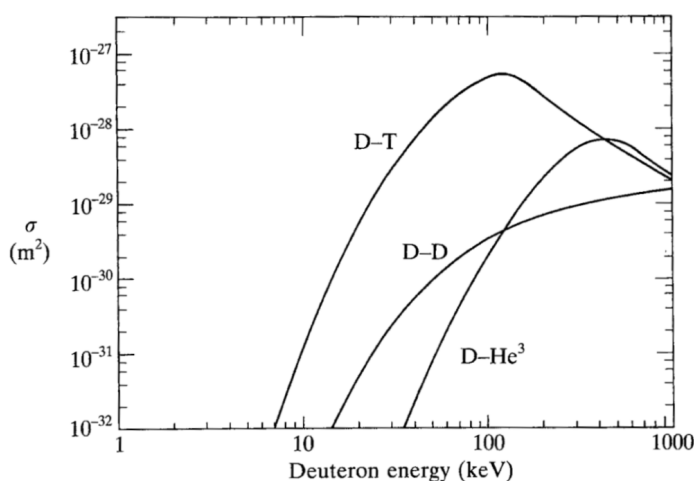
Figure 1.2: Fusion reaction cross-section for D-T fusion [4]

is projected to be a fusion device built in France that produces 500 MW of fusion power from 50 MW heating input [6]. It is expected to test the current technology and push the fusion related research to a new regime.

The design of ITER is based on the tokamak concept, which uses a strong magnetic field to confine the hot plasma and thereby protect the reactor wall structures [6]. As shown in Fig. 1.1, tokamaks generate helical magnetic field lines through coils surrounding the vacuum chamber and plasma current flowing in the toroidal direction. The helical magnetic field line is necessary to balance particle drifts and achieve stable plasma equilibrium. The high temperature required for fusion reactions is sustained by various auxiliary heating systems, including ohmic heating, Neutral Beam Injection (NBI), and electromagnetic waves in various frequency ranges. Those heating systems are also used to induce and maintain the plasma current required for confinement [6].

Among many possible candidates for fusion reactor fuels, deuterium-tritium (D-T) fusion is the most desirable choice due to its high fusion reaction cross-section [7], as shown in Fig. 1.2. The fusion reaction of deuterium and tritium produces a 3.5 MeV alpha particle and releases a
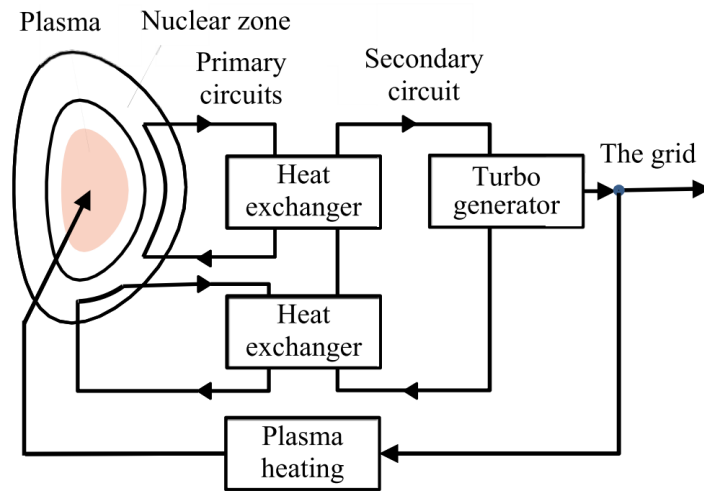
Figure 1.3: Fusion power plant scheme [5]

14.1 MeV neutron. The high-energy neutron flux and intense heat radiation emitted during the fusion process are absorbed by critical components such as the first wall, blanket, and divertors [7]. These components are efficiently cooled by multiple primary cooling circuits. The absorbed heat in the primary cooling circuit is then transferred to a secondary circuit via heat exchangers and used to produce electricity through turbo generators. A schematic diagram of a fusion power plant is shown in Fig. 1.3.

1.2 Motivation to Study Intrinsic Rotation

As the D-T plasma is heated to thermonuclear conditions, fusion reactions occur, and the emitted 3.5 MeV α-particles start to heat the plasma. When sufficient fusion reaction rate and confinement conditions are reached, the plasma energy loss can be completely compensated by the α-particle heating. At this point, the plasma is self-sustaining, and no externally applied heating is required, which is called ignition by the analogy with burning fossil fuel [4]. The so-called Lawson criterion is used to describe

the necessary condition required to reach ignition, which states that the triple product of the plasma density n, plasma temperature T, and energy confinement time τ_E should be at least $nT\tau_E > 3 \times 10^{21}$ m^{-3}keVs [4].

As fusion experiments continue to advance, increasingly higher plasma densities and temperatures are attained in various machines, but the ignition condition has not been achieved [8]. The fusion community recognizes that merely increasing the auxiliary heating power is insufficient to reach ignition. As more external heating power is injected into the plasma, the density and temperature gradients are steepened, which enhances the radial turbulent transport caused by micro-instabilities. As a result, the turbulence level increases significantly, and more coherent structures are formed, which seriously degrades the confinement and inhibits the plasma from reaching ignition. Hence, the study of plasma turbulence and its mitigation becomes one of the most important subjects in fusion research. It has hereby been found that the sheared poloidal and toroidal flows suppress turbulence and contribute to the reduction of heat and particle transport in magnetic fusion devices [9].

Sheared poloidal and toroidal flows can build a strong nonuniform radial electric field, which in turn generates a sheared $E \times B$ flow. It should be noted that the poloidal and toroidal flows refer to the bulk ion mass flow in the respective directions, which are determined by the momentum input and transport [10]. Meanwhile, the $E \times B$ flow refers to the drift motion of charged particles in the plasma resulting from the Lorentz force, which is determined by the radial force balance [10].

Among the various flows in plasma, the $E \times B$ flow is responsible for the suppression of turbulence and turbulent transport. Theoretical calculations show that the $E \times B$ flow is the sole advectant of fluctuations in particle density, energy, and momentum [10]. This perpendicular flow will tear apart turbulence eddy structure, accelerate turbulence decorrelation, and suppress turbulent transport [10, 11]. This mechanism is believed to

effectively reduce the overall anomalous transport inside the plasma and contribute to the formation of transport barriers during the transition from low to high confinement mode [9]. Compared with the low confinement mode, or L-mode, the high confinement mode, or H-mode, has significantly increased global particle and thermal energy confinement time. The transition from L-mode to H-mode occurs when the input power exceeds a specific threshold, which has been observed to be strongly dependent on rotation in experiments [12].

In present-day experiments, toroidal rotation is typically driven by external momentum sources such as tangential NBI. While external momentum sources are sufficient in current medium-scale experiments, they may not drive sufficient rotations to stabilize the plasma and suppress turbulent transport in future large-scale tokamaks, such as ITER. This limitation is due to the substantial moment of inertia and the reduced efficiency of torque injection from high-energy neutral beams in larger systems. Therefore, understanding the mechanisms of self-generated rotation becomes critical in such contexts.

Spontaneous rotation is observed across many machines and under various confinement regimes [13, 14, 15, 16, 17]. Experiments conducted in the Alcator C-Mod tokamak have demonstrated that strong intrinsic rotations can be generated during the transition of confinement regime from L-mode to H-mode in ohmic-heated plasmas with no external momentum injection[16]. As shown in Fig. 1.4, the change in core toroidal rotation from L-mode to H-mode can reach up to 100 km/s and exhibits strong linear dependency on the stored energy normalized to the plasma current. Work on the DIII-D tokamak suggests that intrinsic torque is localized at the plasma edge and can be comparable to the external torque from tangential NBI [18]. Velocity profile evolution indicates that the intrinsic rotation originates at the plasma edge and propagates into the core on a momentum confinement time scale [17].
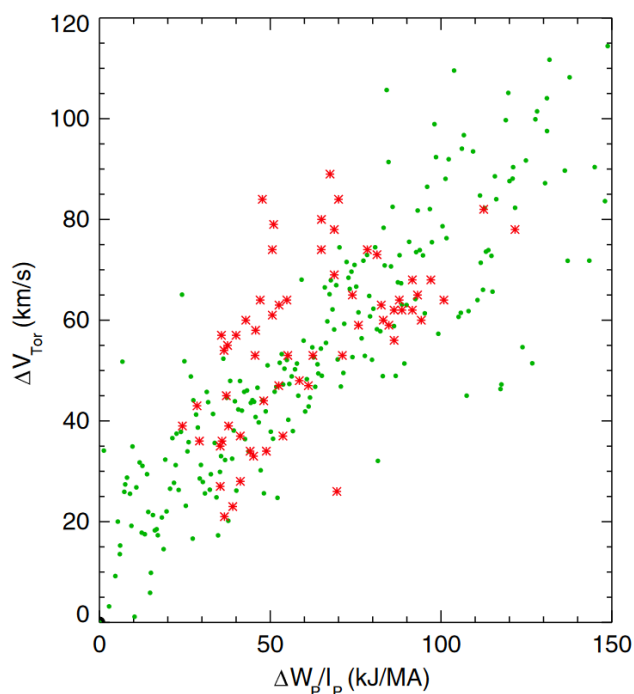
Figure 1.4: The change in the core toroidal rotation from L-mode to I-mode (red) and to H-mode (green) [16]

The theoretical explanation is that, as thermal energy is injected into the plasma via various heating methods, it creates steeper density and temperature gradients, which in turn induce turbulence. This turbulence drives local velocity fluctuations and generates a spatially nonuniform Reynolds stress $\langle \tilde{v}_r \tilde{v}_\phi \rangle$ when symmetry breaking mechanisms change the phase angle between the velocity fields. Residual stress, defined as the part of Reynolds stress that is independent of velocity and its gradient, plays a critical role. The divergence of this residual stress acts as an intrinsic torque, leading to the observed spontaneous rotation. This physical process effectively converts heat flux into parallel flow via the mechanism of turbulent Reynolds stress [19, 20].

This theory of turbulence-driven intrinsic rotation has not been experimentally demonstrated. While significant theoretical and experimental

efforts have been dedicated to this subject, the fundamental mechanism driving the generation of intrinsic rotation remains elusive and is not fully understood. To reliably predict and control plasma rotation for achieving the desired confinement, it is essential to investigate the complex mechanism between turbulence, turbulent momentum transport, Reynolds stress, and intrinsic torque from a microscopic standpoint, a level of understanding that previous studies have not yet attained.

1.3   Research Goals

To study the generation of intrinsic rotation, a comprehensive understanding of diverse momentum sources and transport mechanisms in plasmas is crucial. Classical and neoclassical momentum transport have been extensively studied and well understood. While turbulence remains challenging and complex in many aspects, substantial research efforts have established a foundational understanding of its nature and the mechanisms by which it induces turbulent momentum transport and generates intrinsic torque via turbulent stress.

Previous experiments on intrinsic rotation mainly focus on the various global effects on rotation, and not much has been done to study the mechanism between local flow generation and the underlying turbulence at ion gyroscales. This research seeks to bridge this gap by measuring the relevant fluctuating velocity fields and examining the interaction between turbulence, Reynolds stress, and flow generation in L-mode plasmas in the DIII-D tokamak. This is achieved by the high-quality fluctuation measurements obtained using Beam Emission Spectroscopy (BES) and Ultra-Fast Charge Exchange Recombination Spectroscopy (UF-CHERS).

The 64-channel BES system measures long-wavelength density fluctuations by detecting Doppler-shifted D_α emissions [21]. Velocimetry analysis is applied to track turbulence eddies and infer radial and poloidal veloc-

ity fluctuations [22]. The UF-CHERS diagnostic observes the $n = 8 \rightarrow 7$ transitions in hydrogenic carbons $C^{(5+)*}$ with 1 µs time resolution at two spatial locations [23]. The spectral widths and line shifts provides measurements of ion temperature and toroidal velocity fluctuations. The cross-field correlation analysis, combining the BES and UF-CHERS measurements, allows us to directly determine the Reynolds stress.

The structure of this thesis is outlined as follows. Chapter 2 provides a theoretical background and reviews previous experimental studies on plasma rotations. It discusses the mechanisms of momentum transport, including classical, neoclassical, and turbulent transport. Additionally, this chapter examines two important momentum sources: intrinsic torque generated by turbulence-driven Reynolds Stress and external torque from neutral beams.

Chapter 3 introduces the DIII-D tokamak, along with the major diagnostics, BES and UF-CHERS. It also details the data analysis techniques employed in this research.

Chapter 4 describes the experiments carried out at DIII-D. It compares turbulence characteristics under different plasma conditions and presents multifield cross-correlation results to demonstrate the generation of Reynolds stress by turbulence.

Chapter 5 extracts the residual stress from the measured Reynolds stress and derives the resulting intrinsic torque. The rotation profile is then reconstructed using the momentum balance equation with and without this intrinsic torque, and compared with experimental observations.

Finally, Chapter 6 offers a detailed summary, highlights diagnostic and methodological advancements, concludes major physics results, and explores potential scientific questions for future research.

2   BACKGROUND AND THEORY

This chapter begins by reviewing the theoretical background of rotation in tokamak plasmas. It introduces crucial momentum sources and transport mechanisms. A leading theory of intrinsic rotation, which suggests that intrinsic torque can be generated from turbulence-driven nonuniform Reynolds stress, is explored in depth. Supporting experimental findings and simulation results are presented, which motivate the design of experiments and measurements conducted at the DIII-D tokamak in the framework of this thesis project.

2.1   Rotation in Tokamak Plasmas

In this section, an analytical model is developed based on the fluid moments of a general plasma kinetic equation to establish the equations governing the generation of toroidal flow by turbulent Reynolds stress in the context of finite aspect ratio, non-circular cross-section, and axisymmetric toroidal geometry [24].

In this framework, plasma is assumed to have two species, electrons and hydrogenic ions. The continuity and momentum conservation equations, derived from the two-fluid moments of the full plasma kinetic equations, are used to describe the plasma parameters [24, 25].

$$\frac{\partial n}{\partial t} + \nabla \cdot n\mathbf{v} = S_n \tag{2.1}$$

$$m\frac{\partial}{\partial t}n\mathbf{v} + \nabla \cdot (mn\mathbf{v}\mathbf{v}) = nZe\left(\mathbf{E} + \mathbf{v} \times \mathbf{B}\right) - \nabla p - \nabla \cdot \pi + \mathbf{R} + \mathbf{S}_m \tag{2.2}$$

where n is the plasma density, $\mathbf{v}$ is the flow velocity, $\mathbf{E}$ is the electric field, $\mathbf{B}$ is the magnetic field, $p = nT$ is the plasma pressure, $-\nabla \cdot \pi$ is the viscous force density, $\mathbf{R}$ is the Coulomb collision dynamical friction force density,

S_n and $\mathbf{S}_m$ are the source terms for particle and momentum. These two equations apply to both ions and electrons, and the species label 's' will be added as needed.

A toroidal coordinate system (r, θ, ϕ) is used to describe the geometry, where r is the minor radius, θ is the poloidal angle and ϕ is the toroidal angle. The structure of axisymmetric equilibrium magnetic field $\mathbf{B}_0$ can be described as [25]

$$\mathbf{B}_0 = \mathbf{B}_\phi + \mathbf{B}_\theta = \nabla \times (\psi_\phi \nabla \theta - \psi_\theta \nabla \phi) \tag{2.3}$$

where $2\pi\psi_\phi$ and $2\pi\psi_\theta$ are the equilibrium toroidal and poloidal magnetic fluxes. The dimensionless radial coordinate $\rho \equiv \sqrt{\psi_\phi/\psi_\phi(a)}$ is defined based on the toroidal flux and ranges from zero (at the magnetic axis) to unity (at the plasma separatrix).

Small gyroradius expansion is applied to derive the magnetohydrodynamic (MHD) force balance equilibrium at the zeroth order, flows within flux surfaces at the first order, and radial transport fluxes at the second order [25]. To the lowest order in the gyroradius expansion, the density n, temperature T, and pressure p of both species will be constant on the magnetic flux surfaces. To the first order, poloidal variation in the toroidal-averaged plasma parameters and toroidal variations due to three-dimensional nonaxisymmetric (NA) perturbations are allowed. Therefore, the plasma parameters n, T and p can be expanded as [25]

$$p = p_0(\rho) + \delta\left[\bar{p}_1(\rho, \theta) + \tilde{p}_1(\rho, \theta, \phi)\right] + O\{\delta^2\} \tag{2.4}$$

where $\delta \sim \rho_s/a \ll 1$ is the small gyroradius expansion parameter, $\rho_s = v_{th,s}/\omega_{c,s}$ is the average gyroradius for species 's' with thermal speed $v_{th,s} \equiv \sqrt{2T_s/m_s}$ and gyrofrequency $\omega_{c,s} \equiv q_s B_0/m_s$. The bar hat on $\bar{p}$ indicates that this quantity is averaged over the toroidal direction. The tilde hat on $\tilde{p}$ indicates that this is a perturbation quantity.

The electric field potential Φ and magnetic vector potential $\mathbf{A}$ can be expanded in a similar way. Equations governing the generation of flows are then derived by plugging the expanded plasma parameters back into Eqs. (2.1) and (2.2), and evaluate them in different orders of δ. Solving the zeroth order gives the axisymmetric portion of the flow [24]

$$\Omega(\psi) = \frac{\partial \bar{\Phi}}{\partial \psi} + \frac{1}{\bar{n} Z e} \frac{\partial \bar{p}}{\partial \psi} \tag{2.5}$$

which can be rearranged as the radial force balance equation [24]

$$\bar{E}_r = -\frac{\partial \bar{\Phi}}{\partial \psi} \nabla \psi = \left[\frac{1}{\bar{n} Z e} \frac{\partial \bar{p}}{\partial \psi} - \Omega(\psi) \right] \nabla \psi$$
$$= \frac{1}{\bar{n} Z e} \frac{\partial \bar{p}}{\partial \psi} \nabla \psi - \bar{v}_\phi B_\theta + \bar{v}_\theta B_\phi \tag{2.6}$$

This equation provides a relation between the averaged toroidal flow $\bar{v}_\phi$, poloidal flow $\bar{v}_\theta$, diamagnetic flow $v_* = 1/(Z e B^2) B \times \nabla p$, and lowest order radial electric field $\bar{E}_r$.

The analytic expression for turbulence-driven flow can be derived by evaluating the same equations to higher order in δ. The first-order toroidal component of Eqn. (2.2) is obtained by taking the dot product of $\hat{\mathbf{e}}_\phi$ and averaging it over the magnetic flux surface [24, 25, 26], resulting in

$$m\bar{n} \frac{\partial}{\partial t} \langle \bar{v}_\phi \rangle = \underbrace{- \frac{1}{V'(\psi)} \frac{\partial}{\partial \psi} V'(\psi) \left(m\bar{n} \langle \tilde{v}_r \tilde{v}_\phi \rangle + m \bar{v}_\phi \langle \tilde{n} \tilde{v}_r \rangle + m \langle \tilde{n} \tilde{v}_r \tilde{v}_\phi \rangle \right)}_{\text{turbulence-driven}}$$
$$+ \underbrace{\langle \mathbf{R}^1 \cdot \hat{\mathbf{e}}_\phi \rangle}_{\text{neoclassical}} + \underbrace{\left\langle \sum \bar{S}_m \cdot \hat{\mathbf{e}}_\phi \right\rangle}_{\text{mom. sources}} \tag{2.7}$$

Here, $V'(\psi) = dV/d\psi$ where V is the volume inside a given flux surface and 'mom. sources' refers to external momentum sources such as NBI

which will be introduced in Section 2.2. Moreover, 'neoclassical' refers to the classical and neoclassical transport fluxes which are discussed in Section 2.3. Finally, turbulence-driven momentum fluxes will be explained in detail in Section 2.4. With all three terms evaluated, the toroidal rotation profile can be reconstructed from the momentum balance equation.

Notably, there are several terms that are less significant or not applicable to this experimental condition and are therefore omitted in Eqn. (2.7), such as $\langle \nabla \cdot \overline{\pi}_\parallel^{NA} \cdot \hat{\mathbf{e}}_\phi \rangle$ which represents the neoclassical toroidal viscosity (NTV) due to non-resonant NA magnetic fields. NTV exerts a damping effect on toroidal and poloidal flows, but the damping of the poloidal flow can also act as a driving force for toroidal flow due to the coupling term [26]. However, since no error fields are applied in this experiment, NTV torque is considered negligible and is not addressed in this thesis work. The same rationale applies to resonant NA magnetic fields, fluctuation-induced Maxwell stress, and poloidal magnetic flux transients [25].

2.2   Momentum Sources from NBI

NBI is applied to heat, fuel, and rotate tokamak plasmas, and it is planned for the ITER experiment. Typically, a neutralized beam of high energy atoms, with atom energies on the order 100 keV, velocities around $v/c \sim 0.01$, and power levels ranging from 1 to 10 MW, is injected into plasmas. Tangential NBI is the most common external source of toroidal momentum in tokamak plasmas. The mechanisms of momentum transfer from neutral beams to the bulk plasma include the collisional friction between plasma and beam-generated fast ions and the $\mathbf{j} \times \mathbf{B}$ torque due to beam-induced radial plasma current [27]. This current originates from a relative displacement of the electron and fast ions created when a neutral beam atom is ionized. While electrons will mainly remain bound to the flux surfaces, fast ions exhibit significant drifts off the flux surfaces.

To quantify the NBI torque, a convenient form of the momentum conservation equation Eqn. (2.2) is obtained by multiplying $\mathbf{v}$ with the continuity equation Eqn. (2.1) and subtracting it from Eqn. (2.2).

$$mn\frac{\partial}{\partial t}\mathbf{v} + mn\left(\mathbf{v}\cdot\nabla\right)\mathbf{v} = nZe\left(\mathbf{E}+\mathbf{v}\times\mathbf{B}\right) - \nabla p - \nabla\cdot\pi + \mathbf{R} \qquad (2.8)$$

The toroidal component of Eqn. (2.8) is obtained by taking the dot product with $\hat{\mathbf{e}}_\phi$ and then averaging it over the magnetic flux surface. The resulting equation is further simplified by the fact that the convective derivative term vanishes when it is averaged over the magnetic flux surface, $\langle\mathbf{v}\cdot\nabla\rangle\mathbf{v} = 0$, due to incompressible flow. The simplified toroidal momentum conservation equation for ion can be written as [27]

$$m_i n_i \frac{\partial}{\partial t}\langle\mathbf{v}_\phi\rangle + \langle\nabla\cdot\pi_i\cdot\hat{\mathbf{e}}_\phi\rangle = \frac{1}{c}\langle\mathbf{j}\cdot\nabla\psi\rangle + \langle\mathbf{R}\cdot\hat{\mathbf{e}}_\phi\rangle \qquad (2.9)$$

where π_i is the ion viscous stress tensor and $\mathbf{R} = \mathbf{R}_{if} + \mathbf{R}_{ef}$ is the sum of collisional momentum transport rate from fast ions to plasma ions and electrons. The radial current due to fast ions, $\mathbf{j}_f$, is canceled by a radial current, $\mathbf{j}$, flowing in the bulk plasma to satisfy the flux surface averaged Maxwell's equation, $\langle\mathbf{j}\cdot\nabla\psi\rangle = -\langle\mathbf{j}_f\cdot\nabla\psi\rangle$. The collisional momentum transport rate on plasma ions and electrons can be expressed in terms of fast ions using the momentum conservation $\mathbf{R}_{if} + \mathbf{R}_{ef} = -\left(\mathbf{R}_{fi} + \mathbf{R}_{fe}\right)$. Therefore, the right-hand side of Eqn. (2.9) can be written as [27]

$$\tau_{\mathrm{NBI}} = -\frac{1}{c}\langle\mathbf{j}_f\cdot\nabla\psi\rangle - \langle(\mathbf{R}_{fi} + \mathbf{R}_{fe})\cdot\hat{\mathbf{e}}_\phi\rangle \qquad (2.10)$$

The toroidal torque from NBI, τ_{NBI}, is determined by the collisional forces on fast ions, $\mathbf{R}_{fi} + \mathbf{R}_{fe}$, and the radial fast ion current, $\mathbf{j}_f$, which can be calculated using the fast ion distribution function from the drift kinetic equation. The flux surface averaged fast ion current density and friction forces are defined as the following [27].

$$\langle \mathbf{j}_f \cdot \nabla \psi \rangle = e_f \left\langle \int d^3 v \ \mathbf{v}_d \cdot \nabla \psi f \right\rangle \qquad (2.11)$$

$$\mathbf{R}_{fi} + \mathbf{R}_{fe} = \int d^3 v \ m_f \mathbf{v} C_f f_{-1} \qquad (2.12)$$

where $\mathbf{v}_d$ is the guiding center drift velocity, C_f is the collision cross-section, f is the fast ion distribution function, and f_{-1} is the lowest order distribution function in expansion of δ, $f = f_{-1} + f_0 + f_1 + \cdots$.

The beam-generated fast ions can be injected into either trapped or untrapped orbits. For fast ions injected into trapped orbits, the lowest order of the fast ion distribution function averaged over a bounce period is independent of the poloidal angle, θ, and the bounce arc length, σ, due to the continuity at the turning points. Therefore, the resulting torque is time-independent, corresponding to the prompt torque observed in experiments after NBI is applied [27].

To calculate the torque input from fast ions injected into untrapped orbits, a time-dependent fast ion distribution function is used. In this case, the fast ion birth rate varies with time instead of following a simple step function. This results in a transient increase in the NBI torque input. The system approaches a steady state exponentially within a few slowing-down times, corresponding to the gradually increasing torque observed in experiments [27].

The mechanisms of NBI torques are well understood and can be effectively modeled by analysis codes such as NUBEAM [28]. NUBEAM is a computational model to calculate NBI power deposition, driven radial current, momentum transfer, fueling and other effects on plasmas [28], and is integrated in the transport analysis code TRANSP (see Appendix A for details about TRANSP). Figure 2.1 shows the various NBI torques calculated using the NUBEAM module in TRANSP for a representative discharge in this thesis, with both co- and counter-NBI.
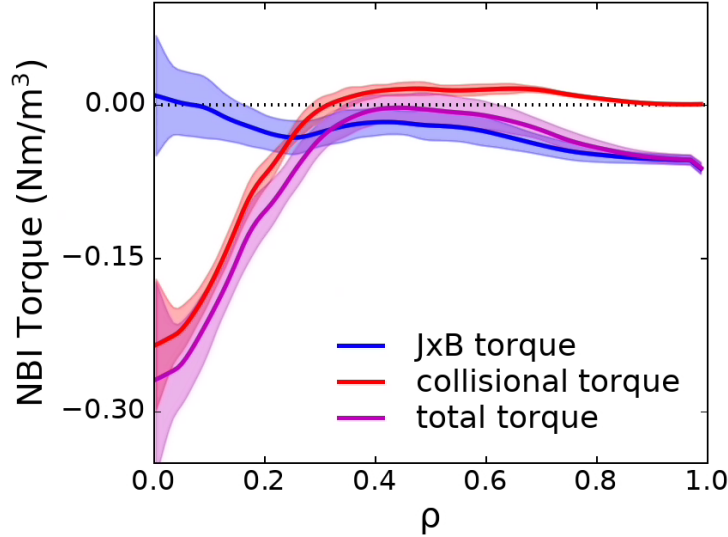
Figure 2.1: NBI torques deposition profile for DIII-D discharge #193082, calculated using NUBEAM module in TRANSP

2.3 Classical and Neoclassical Transport

Collisions and gyro-motions produce net fluxes of particle, heat, and momentum across the magnetic field lines. Classical transport theory is developed based on the fluid theory to study the transport due to collisions and gyro-motions for a cylindrical plasma with an axial magnetic field and axial currents. Neoclassical transport theory includes the consideration of the poloidal asymmetry effects when a cylindrical plasma is deformed into a torus [29].

For a source-free, steady-state plasma with isotropic pressure, the momentum conservation equation Eqn. (2.2) is reduced to [29]

$$\nabla p = nZe(\mathbf{E} + \mathbf{v} \times \mathbf{B}) + \mathbf{R}^1 \tag{2.13}$$

For a cylindrical plasma, classical cross-field particle transport, Γ_r^C, can be obtained from the poloidal component of Eqn. (2.13), with $\partial p/\partial \theta = 0$ and $E_\theta = -\frac{1}{r}\partial \Phi/\partial \theta = 0$ due to the poloidal symmetry [29]

$$\Gamma_r^C = n v_r = \frac{R_\theta^1}{ZeB_z} = \frac{m\nu_{s,s'}}{(ZeB_z)^2} \frac{\partial p}{\partial r} \tag{2.14}$$

Here, the collisional operator is evaluated as $R_{s,\theta}^1 = -n_s m_s \nu_{s,s'}(v_{s,\theta} - v_{s',\theta})$, and $\nu_{s,s'}$ is the collisional frequency between two species. When the cylindrical plasma is deformed into an axisymmetric torus, the poloidal symmetry is lost, which brings back the $\partial p/\partial\theta$ and $\partial\Phi/\partial\theta$ terms [29]. The neoclassical cross-field particle transport, Γ_r^{NEO}, can then be derived as

$$\begin{aligned} \Gamma_r^{NEO} = n v_r &= \frac{R_\theta^1}{ZeB_\phi} - \frac{1}{ZeB_\phi}\left(\frac{1}{r}\frac{\partial p}{\partial\theta} + nZe\frac{1}{r}\frac{\partial\Phi}{\partial\theta}\right) \\ &= \Gamma_r^C + \Gamma_r^{PS} + \Gamma_r^{BP} \end{aligned} \tag{2.15}$$

The first term in Eqn. (2.15) corresponds to the classical transport flux driven by the poloidal collisional friction, as shown in Eqn. (2.14). The second term represents the neoclassical transport flux due to the toroidal geometry effect, which is known as Pfirsch–Schlüter (PS) flux [29]. The Pfirsch–Schlüter flux is derived by including thermal force in the parallel collisional operator, $R_{s,\parallel}^1 = -n_s m_s \nu_{s,s'}(v_{s,\parallel} - v_{s',\parallel}) - n_s \nabla_\parallel T_s$ [29].

$$\Gamma_r^{PS} = -\frac{2\epsilon^2 m\nu_{s,s'}}{(ZeB_\theta)^2}\left(\frac{\partial p}{\partial r} - n\frac{\partial T}{\partial r}\right) \tag{2.16}$$

where $\epsilon = a/R$ is the inverse aspect ratio. The Pfirsch–Schlüter flux is always present in the plasma due to the toroidal geometry but only becomes dominant when the particle orbit effects are negligible, which requires the effective time for small-angle collisional deflection, $\epsilon(\nu_{90})^{-1}$, that scatters into or out of a trapped particle orbit to be smaller than the time required for untrapped particle orbit, qR_0/v_{th}.

The Pfirsch–Schlüter flux shares many characteristics with the classical flux. The relative magnitude of the Pfirsch–Schlüter flux and classical flux is estimated as $\Gamma_r^{PS} \approx 2q^2\Gamma_r^C$. For a typical value of $q \approx 1$ at the center

and q ≈ 3 at the edge, the Pfirsch–Schlüter flux is much larger than the classical flux and significantly enhances the cross-field transport [29].

The last term represents the neoclassical transport flux due to the contribution of trapped-particles effects in the collisional operator R^1, which is known as the Banana-Plateau (BP) flux [29].

$$\Gamma_r^{BP} = -\epsilon^{-\frac{1}{2}}\overline{\nu}\left(\frac{m\nu_{th}}{eB_\theta}\right)^2\frac{\partial n}{\partial r} \tag{2.17}$$

where $\overline{\nu}$ is the effective collision frequency. The Banana-Plateau flux becomes important when the effective scattering time is greater than the time required to complete a marginally trapped particle orbit, $qR_0/\sqrt{\epsilon}\nu_{th}$, in which case the effect of the trapped particle orbit is dominant and is referred as the Banana regime, as shown in Fig. 2.2. For an effective scattering time smaller than the time required for a marginally trapped particle orbit, but larger than the time required for an untrapped particle orbit, qR_0/ν_{th}, the effect of the untrapped particle orbit is dominant and is referred as the Plateau regime, where the magnitude of the Banana-Plateau fluxes do not depend on collisionality [29], as shown in Fig. 2.2.
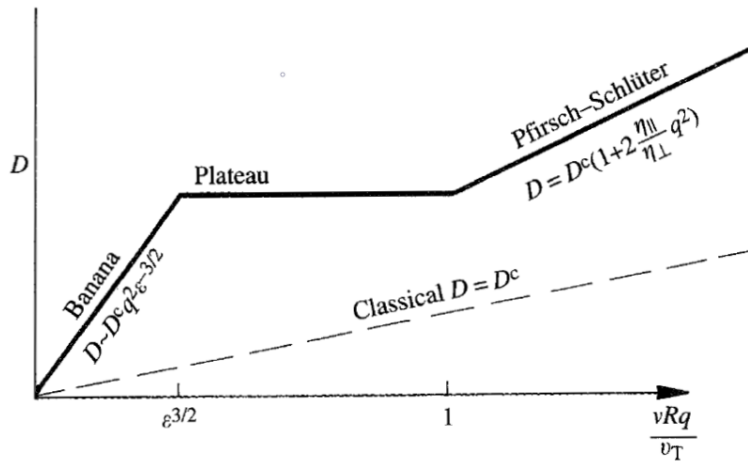
Figure 2.2: Variation of diffusion coefficient with collision frequency for different transport regimes [4]

Assume the scattering time is long enough for finishing the trapped particle orbit, $\nu^* = \nu_{90} q R_0 / \nu_{th} \ll 1$, and the effect of the temperature gradient is negligible, the relative magnitude of the Banana-Plateau flux and the classical flux is estimated as $\Gamma_r^{BP} \approx q^2 \epsilon^{-\frac{3}{2}} \Gamma_r^C$ [29].

The classical and neoclassical cross-field momentum transport consist of a convective component due to the particle flux and a diffusive part driven by the radial velocity gradient. The radial flux of the toroidal momentum Γ_ϕ^{NC} can be written as [29]

$$\Gamma_\phi^{NC} = m(\Gamma_r^C + \Gamma_r^{PS} + \Gamma_r^{BP})v_\phi - mn\chi_\phi^{NC}\frac{\partial v_\phi}{\partial r} \qquad (2.18)$$

where χ_ϕ^{NC} is the neoclassical perpendicular viscosity coefficient. The mechanisms of classical and neoclassical transport are well understood, and the corresponding transport coefficients can be calculated by analysis codes such as NEO [30] and NCLASS [31] module in TRANSP.

2.4   Turbulence and Turbulent Transport

In tokamaks, the measured transport is almost always larger than the prediction from the neoclassical transport theory. The excess part is usually referred to as "anomalous" transport due to the lack of a complete understanding. It is widely believed that this anomalous transport is associated with the small-scale turbulent fluctuations of density, temperature, electric field, and magnetic field. One of the most frequently discussed mechanisms is that turbulence and turbulent transport result from electrostatic drift waves, which are introduced in detail in this section.

2.4.1   Drift Waves

Drift waves exist universally in magnetized plasmas and are a dominant mechanism governing the turbulent transport of particles, energy, and

momentum across magnetic field lines. Drift wave instabilities can be driven by gradients in plasma parameters such as density and temperature, and trapped particle effects [32].

In the presence of radial ion and electron pressure gradients, a magnetized plasma develops the corresponding ion and electron diamagnetic currents in the poloidal direction to maintain the plasma equilibrium, $\mathbf{j} \times \mathbf{B}/c = \nabla(p_e + p_i)$ [33]. If a small perturbation appears in the ion and electron pressure gradients, the corresponding ion and electron diamagnetic currents will respond to this perturbation. This perturbed current is carried by ions whose guiding center moves in the poloidal direction at the ion polarization drift velocity associated with the radial electric field. The resulting perturbations propagate predominantly in the ion and electron diamagnetic drift directions and are called drift waves [34].

To sustain the plasma quasineutrality, the divergence of the total perturbed current must vanish, $\sum_s \nabla \cdot \mathbf{j}_s = 0$. Due to the high mobility of electrons parallel to the magnetic field, a corresponding perturbed parallel current is developed. In the absence of dissipation of the parallel electron motion, the resulting drift wave density fluctuations will be in phase with the wave plasma potential fluctuations, $\tilde{n}/\bar{n} \approx e\tilde{\Phi}/kT_e$. The resulting time-averaged cross-field convective particle flux is zero, and no net transport is induced, as shown in Fig. 2.3(a).

If the electrons lose momentum to the background plasma via dissipation mechanisms such as ion-electron Coulomb collisions, wave-particle interactions, and collisions with trapped electrons, an out-of-phase addition, $i\delta$, will be introduced to the electron response, $\tilde{n}/\bar{n} \approx e\tilde{\Phi}/kT_e(1-i\delta)$, and cause a phase shift relative to the wave plasma potential fluctuations. In this case, the phase shift produces an imbalance between the upward and downward convective particle fluxes across the confining magnetic field. With a positive phase shift, a net plasma transport flux toward lower density is induced, as shown in Fig. 2.3(b).
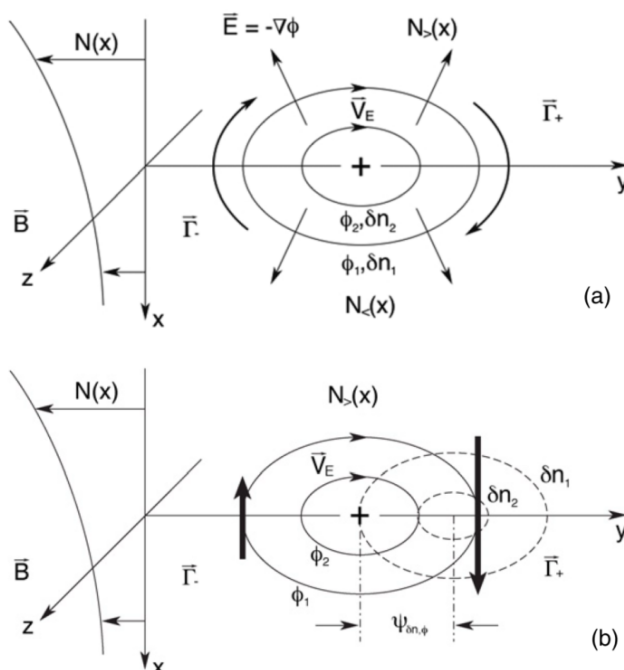
Figure 2.3: Drift wave mechanism showing E × B convection in a nonuniform, magnetized plasma [33]. (a) Density and potential fluctuations in drift wave without parallel electron dissipation. (b) Density and potential fluctuations in drift wave with finite parallel electron dissipation.

The drift wave transport fluxes universally exist for different regimes of plasma collisionality and various confinement geometries [33]. Figure 2.3 describes the development of density gradient driven turbulent transport in an isothermal plasma. This analogy can also be applied to a temperature gradient driven turbulent transport in an inhomogeneous plasma.

The electrostatic drift wave kinetic dispersion relation for multiple charged species with Maxwellian distribution is [32]

$$D(\mathbf{k}, \omega) = \sum_s \frac{n_s e_s^2}{T_s} \left[1 - \left\langle \frac{\omega \omega_s^*(\epsilon_s)}{\omega - \omega_{D,s} - k_\parallel v_\parallel} J_0^2 \right\rangle \right] \qquad (2.19)$$

where $\langle \, \rangle$ is an average over the Maxwellian distribution, J_0 is the Bessel

function, and the density and temperature gradients are included in [32]

$$\omega_s^*(\epsilon_s) = \frac{k_y T_s}{e_s n_{0,s} B} \left(\frac{\partial n_{0,s}}{\partial r} \right) \left[1 + \eta_s \left(\epsilon_s - \frac{3}{2} \right) \right] \qquad (2.20)$$

and

$$\epsilon_s = \frac{m_s v^2}{2 T_s} \qquad (2.21)$$

$$\eta_s = \frac{1}{T_s} \frac{\partial T_s}{\partial r} \bigg/ \frac{1}{n_{0,s}} \frac{\partial n_{0,s}}{\partial r} = \frac{L_{n,s}}{L_{T,s}} \qquad (2.22)$$

Here, $L_{n,s}$ is the density gradient scale length and $L_{T,s}$ is the temperature gradient scale length. The wave-particle resonance is determined by the denominator $\omega - k_{\parallel} v_{\parallel} = \omega_{D,s}$, where the guiding center drift frequency $\omega_{D,s}$ can be written as [32]

$$\omega_{D,s} = \frac{k_y T_s}{e_s B R} \left(\frac{m_s v_{\perp}^2}{2 T_s} + \frac{m_s v_{\parallel}^2}{T_s} \right) \qquad (2.23)$$

Using the quasilinear approach, the various plasma parameters in the fluid equations are written as a time-independent equilibrium solution plus a first-order fluctuation. The expression for the flux surface averaged particle transport arising from electrostatic drift wave turbulence is [32]

$$\Gamma_s^{turb} = \frac{1}{A} \int \tilde{n}_s \mathbf{v}_{E \times B} \cdot d\mathbf{A} \qquad (2.24)$$

In a cylindrical model, assuming the dissipation term is small, the particle flux can be calculated using Eqn. (2.24)

$$\Gamma_s^{turb} = -L_{n,s}^2 \gamma \left\langle \left(\frac{\tilde{n}_s}{n_{0,s}} \right)^2 \right\rangle \frac{\partial n_{0,s}}{\partial r} = \chi_s^{turb} \frac{\partial n_{0,s}}{\partial r} \qquad (2.25)$$

where $\gamma = \delta \omega^*$ is the linear growth rate of the drift wave, $\tilde{n}_s$ is the density fluctuation, and χ_s^{turb} is the turbulent diffusion coefficient [32].

The typical procedures to theoretically study drift wave driven turbulent transport begin first with identifying the conditions for which kind of instabilities will be unstable, then calculating the linear growth rate, and finally estimating the density saturation fluctuation level and its corresponding transport coefficients [32]. If the density saturation fluctuations are experimentally measured, the corresponding turbulent transport fluxes can be estimated using Bohm or gyro-Bohm scaling, depending on the spatial scale of the turbulence.

There are many types of drift wave instabilities existing in tokamak plasmas, such as ion temperature gradient modes (ITG), trapped electron modes (TEM), drift Alfven modes, thermal instabilities, electron temperature gradient modes, and drift resistive ballooning modes. For the purpose of relevance, two main long-wavelength electrostatic drift wave instabilities in plasmas, ITG and TEM, are discussed in this thesis.

2.4.2 Ion Temperature Gradient Modes

The ion temperature gradient modes are considered as a dominant drift wave instability that causes the observed anomalous ion transport in tokamak plasmas. ITGs are expected to propagate along the ion diamagnetic direction and become unstable above a certain ion temperature gradient. Assume $k_{\parallel} v_{th,i} / \omega_{D,i} \to 0$, the critical temperature gradient to destabilize ITG modes can be estimated by [32]

$$\eta_{crit} = \left(\frac{L_{n,i}}{L_{T,i}} \right)_{crit} = \frac{4}{3} \frac{L_n}{R} \left(1 + \frac{T_i}{T_e} \right) \left(1 + k_y^2 \rho_i^2 \right) \tag{2.26}$$

Using gyro-Bohm model to estimate the heat diffusivity of the ITG mode with $k_{\perp} \rho_i = 2$ and χ_i^{ITG} can be expressed as [32]

$$\chi_i^{ITG} = \frac{5}{4} \left(\frac{1}{R L_{Ti}} \right)^{\frac{1}{2}} \left(\frac{\rho_i T_e}{e_i B} \right) \tag{2.27}$$

ITGs can be suppressed by the $E \times B$ shear and magnetic shear [32, 10, 35]. The spatial structure of the turbulence is a convective vortex cell. A sheared flow would tilt and distort the vortexes. For example, a poloidal sheared flow would elongate the vortex cell in the poloidal direction and shorten its radial width. Since the ITG transport rate is proportional to the radial correlation length, distortion due to sheared flow would reduce the transport. The $E \times B$ shearing rate can be written as [32]

$$\omega_{E \times B} = \frac{RB_\theta}{B_\phi} \frac{\partial}{\partial r} \left(\frac{E_r}{RB_\theta} \right) \tag{2.28}$$

The ITG transport can be significantly reduced when the $E \times B$ shearing rate is comparable or greater than the maximum linear growth rate of the mode spectrum, γ_{max}^{ITG}. This effect can be expressed by multiplying a $E \times B$ shear suppression factor [32]

$$F_s^{ITG}(\omega_{E \times B}) = \left(1 + \left(\omega_{E \times B} / \gamma_{max}^{ITG} \right)^2 \right)^{-1} \tag{2.29}$$

A similar suppression factor $G(S_m) = S_m^{-1.8}$ is also introduced to the suppressed transport rate due to magnetic shear [32]

$$S_m = \frac{r}{q} \frac{dq}{dr} \tag{2.30}$$

Therefore, the effective transport rate can be written as [32]

$$\chi_i^{ITG,eff} = G(S_m) F_s^{ITG}(\omega_{E \times B}) \chi_i^{ITG} \tag{2.31}$$

The stabilization effects of $E \times B$ shear and magnetic shear have been experimentally demonstrated, showing a reduction in the turbulent heat diffusivity with increasing $E \times B$ shear and magnetic shear [36, 37]. This mechanism plays a crucial role in the self-regulating behavior of turbulence and contributes to the formation of transport barriers during the L-H transition.

2.4.3 Trapped Electron Modes

The most important electron drift instability, characterized by $k_\perp c_s \leqslant \Omega_i$, are the trapped electron modes, arising from trapped particle orbits. TEMs diverge into collisionless and dissipative branches based on electron dynamics. The collisionless TEM occurs when the collisionality is smaller than the bounce frequency, while the dissipative TEM occurs when the collisionality is sufficiently high, where trapped particles scatter out of orbits before reaching a turning point, becoming passing particles. Both collisionless and dissipative TEMs are expected to propagate in the electron diamagnetic direction [32].

In comparison with ITG, the electron heat diffusivity of dissipative TEM with $k \approx 1/\rho_i$ using mixing length estimates can be written as [32]

$$\chi_e^{TEM} = \frac{f_{tr}\eta_e\rho_i^2\omega_e^{*2}(\nu_e/\epsilon)}{\omega_e^{*2} + (\nu_e/\epsilon)^2} \tag{2.32}$$

where $f_{tr} = (2\epsilon/(1+\epsilon))^{1/2}$ is the fraction of well-trapped particles, ν_e is the plasma collisionality, ρ_i is the ion gyroradius, and other parameters are introduced in Eqn. $(2.20)-(2.22)$.

TEM-driven long-wavelength turbulence is coupled to the ITG modes, and it is suppressed by the $E \times B$ sheared flow and magnetic shear through similar mechanisms. Therefore, the effective transport rate of TEMs can be expressed as [32]

$$\chi_e^{TEM,eff} = G(S_m)F_s^{ITG}(\omega_{E\times B})\chi_e^{TEM} \tag{2.33}$$

where the $E \times B$ shear suppression factor, F_s^{ITG}, and the magnetic shear suppression factor, $G(S_m)$, are the same as those for the ITG modes.

ITGs and TEMs are typically the most important instabilities in present-day laboratory tokamak plasmas, especially in the core regions where $r/a \leqslant 0.9$. Discriminating them enables us to study their respective effects on turbulent transport, rotation, and confinement. However, the differ-

entiation between ITG and TEM is often difficult because they usually coexist in the same range of spatial scale around $0.1 < k_\perp \rho_i < 1$. Several approaches can be used to identify the dominant instability, such as gyrokinetic simulations, transport analysis, spatiotemporal turbulence characteristics, and phase velocity estimation.

2.4.4 Momentum Transport and Reynolds Stress

The principle mechanism of electrostatic drift wave turbulence and its driven heat transport are discussed in the previous sections. Early theory and experiments suggest that turbulent momentum transport is strongly correlated with turbulent heat transport. Simultaneous profile measurements of the ion temperature and toroidal rotation during unbalanced neutral beam injection in TFTR show that the turbulent momentum diffusivity and heat diffusivity are comparable in magnitude and vary similarly with temperature and current [38].

However, later experiments reveal the existence of intrinsic rotation with observations of rotation profiles that are not determined solely by the momentum diffusivity and external momentum input [39]. The discovery of intrinsic rotation suggested that there must be an off-diagonal, non-diffusive component in the turbulent momentum transport. To further discuss this problem, we can start with the radial flux of toroidal momentum $\Gamma_\phi^{\text{turb}}$ generated by turbulence-driven density and velocity fluctuations, from Eqn. (2.7).

$$\Gamma_\phi^{\text{turb}}(r) = m_i n_i(r)\langle \tilde{v}_r \tilde{v}_\phi \rangle + m_i v_\phi(r)\langle \tilde{n}_i \tilde{v}_r \rangle + m_i \langle \tilde{n}_i \tilde{v}_r \tilde{v}_\phi \rangle \qquad (2.34)$$

where the first term $\langle \tilde{v}_r \tilde{v}_\phi \rangle$ is the toroidal Reynolds stress, the second term $\langle \tilde{n}_i \tilde{v}_r \rangle$ is the turbulent convection of toroidal momentum, and the third term $\langle \tilde{n}_i \tilde{v}_r \tilde{v}_\phi \rangle$ represents the nonlinear processes such as mode-mode coupling and turbulence spreading [40].

The toroidal Reynolds stress $\langle \tilde{v}_r \tilde{v}_\phi \rangle$ is expected to be the dominant contribution to the total turbulent momentum flux. A further decomposition of the toroidal Reynolds stress is derived from the ion transport matrix for particle, heat and momentum fluxes [40, 41]

$$\langle \tilde{v}_r \tilde{v}_\phi \rangle = -\chi_\phi^{turb} \frac{\partial v_\phi(r)}{\partial r} + V_{pinch}^{turb} v_\phi(r) + \Pi_\phi^{Res} \tag{2.35}$$

where χ_ϕ^{turb} is the turbulent momentum diffusivity or viscosity, V_{pinch}^{turb} is the momentum pinch velocity, and Π_ϕ^{Res} is the residual stress. The poloidal Reynolds stress can be expressed in a similar way as $\langle \tilde{v}_r \tilde{v}_\theta \rangle = -\chi_\theta^{turb} \frac{\partial v_\theta(r)}{\partial r} + V_{pinch}^{turb} v_\theta(r) + \Pi_\theta^{Res}$.

The diffusive term in Reynolds stress is proportional to the velocity gradient and therefore vanishes when the rotation profile is flat [40]. Two non-diffusive terms contribute to the Reynolds stress. The first is momentum pinch, which is driven by thermodynamic forces and proportional to the velocity. This term vanishes when the rotation is near zero. The second is residual stress, which is independent of the velocity gradient or the velocity itself [40]. Notably, both momentum pinch and residual stress are considered as off-diagonal terms in the transport matrix.

The turbulent viscosity χ_ϕ in the diffusive term can be estimated from the ion thermal diffusivity χ_i for drift wave turbulence. Theory and simulations predict that near the ITG marginality where transport is dominated by the resonant scattering of slightly suprathermal ions with $s = \omega/k_\parallel v_{thi}$, the relation between χ_ϕ and χ_i can be expressed as [40]

$$\frac{\chi_\phi}{\chi_i} \approx \frac{\langle s^2 \rangle}{1 + \langle s^2 \rangle/2 + \langle s^4 \rangle/2} \tag{2.36}$$

where the $\langle \rangle$ average is to be taken over the mean distribution function. The ratio of χ_ϕ and χ_i is called the Prandtl number. Theory and simulations predict that the Prandtl number will be close to unity at ITG or TEM dominated core plasma [40, 42, 43]. Experimental measurement of χ_ϕ is

consistent with theory prediction and shows that the Prandtl number is between $0.7 - 2.0$ at TFTR [38] and $0.7 - 1.2$ at ASDEX-U [44].

The momentum pinch is described by a physical model of the turbulent equipartition (TEP) of plasma angular momentum [40, 45, 46]. There are two mechanisms that contribute to the TEP pinch. The first mechanism is closely related to the localization of turbulence within regions of unfavorable magnetic curvature. In the case of turbulence with a ballooning structure, the magnitude of this pinch is inversely proportional to the major radius and becomes stronger toward the magnetic axis [26].

The second mechanism is derived from the translation of angular momentum to linear momentum in the presence of radially varying inertia density in toroidal geometry [46]. In general, the angular momentum can be written as $L_\phi = \lambda^{-1} P_\phi$, where λ^{-1} is related to the effective moment of inertia and is an increasing function of the minor radius due to the toroidal effects. With the inertia density decreasing toward the magnetic axis, when the momentum is homogenized by turbulence, the toroidal velocity of the plasma in regions with smaller moments of inertia has to be accelerated to maintain the angular momentum conservation [46].

These TEP pinch effects cause a peaking of toroidal rotation in the core regardless of the rotation direction. A physical model of the TEP pinch has been developed [45], and the pinch velocity can be expressed as [46]

$$V_{TEP} = 2\chi_\phi \left(-\frac{F + \epsilon r/a}{R} \right) \tag{2.37}$$

and

$$F = \frac{\langle |\tilde{v}_r|^2 (\cos\theta + S_m \sin\theta) \rangle}{\langle |\tilde{v}_r|^2 \rangle} \tag{2.38}$$

Here, F represents the poloidal asymmetry of the turbulence magnitude. $F = 0$ corresponds to poloidally symmetric flute-like turbulence intensity and $F \sim 1$ corresponds to turbulence with a strongly outward ballooning structure [46].

Other theoretical models for the pinch term include mechanisms like thermoelectric velocity, arising from ion thermal effects associated with ion temperature fluctuations [45], and the coupling between density and parallel flow velocity due to the Coriolis drift [47]. Experimental studies were conducted at ASDEX-U to extract momentum transport coefficients from NBI modulation experiments [48]. The pinch number, defined as $-RV_{pinch}/\chi_\phi$, has been found to lie between 0.5 and 4. Similar experiments at JT-60U, using the transient momentum transport analysis, reveal that the pinch velocity increases radially from near-zero at the magnetic axis to -20 m/s at the separatrix in a standard H-mode plasma [49]

In the last term of Eqn. (2.35), the residual stress Π_ϕ^{Res} is defined as the part of the Reynolds stress that is independent of the toroidal velocity and its gradient. A more detailed discussion of the residual stress and the resulting intrinsic torque is presented in the following section.

2.5 Residual Stress and Intrinsic Torque

Diffusive and convective terms in the toroidal Reynolds stress can alter the shape of the rotation profile but not produce net momentum. The residual stress, on the other hand, acts as a momentum source and drives intrinsic rotation. From a theoretical perspective, residual stress is a necessary consequence of the wave-particle momentum exchange. In this process, turbulence acts like an intermediary to produce toroidal torque from the radial force driven by ∇T_i or ∇P_i, analogous to a heat engine [26].

This heat engine paradigm is developed to explain plasma flows generated by heat flux driven turbulence via turbulent residual stress [19]. The underlying physics of the residual stress is governed by the resonant and non-resonant turbulent transport acting in the presence of broken parallel reflection symmetry [40]. The following derivations focus on the non-resonant or 'wave' contribution.

For a source-free plasma where the momentum transport is dominated by turbulence-driven Reynolds stress, Eqn. (2.7) can be reduced to [40]

$$m\bar{n}\frac{\partial}{\partial t}\langle\bar{v}_\phi\rangle = -\frac{\partial}{\partial r}m\bar{n}\left(-\chi_\phi\frac{\partial v_\phi(r)}{\partial r} + V_{pinch}v_\phi(r) + \Pi_\phi^{Res}\right) \qquad (2.39)$$

$$\Pi_\phi^{Res} = \int d\mathbf{k}\, v_{gr}k_\parallel N \qquad (2.40)$$

where Π_ϕ^{Res} is the net radial flux of parallel wave momentum, v_{gr} is the turbulence group velocity, $k_\parallel$ is the parallel wavenumber, and $N(\mathbf{x}, \mathbf{k}, t)$ is the particle population density from the standard wave-kinetic equations. Linearizing the wave kinetic equations yields the population response and thus Eqn. (2.40) can be written as [40]

$$\Pi_\phi^{Res} = \int d\mathbf{k}\, v_{gr}k_\parallel\tau_c\left[k_\theta\langle v_{E\times B}\rangle'\frac{\partial\langle N\rangle}{\partial k_r} - v_{gr}\frac{\partial\langle N\rangle}{\partial r}\right] \qquad (2.41)$$

where τ_c is the correlation time for population response, and $\langle v_{E\times B}\rangle' = \partial\langle v_{E\times B}\rangle/\partial r$ is the electric field shear modulation.

Equation (2.41) shows that the net residual stress is driven by the particle population gradients in both k_r and r. The radial wavenumber gradient of the population density, $\partial\langle N\rangle/\partial k_r$, induces a stress via shearing when the turbulence group velocity changes with respect to the radial wave number, $k_\theta\partial v_{gr}/\partial k_r \neq 0$. For drift waves, this term can be estimated as $k_\theta\partial v_{gr}/\partial k_r \simeq -2k_\theta^2\rho_s^2 v_*/(1 + k_\perp^2\rho_s^2)^2$, which indicates that k_θ and k_r have even contributions in the generation of this stress. The dependence on the diamagnetic flow v_* suggests that this term can change its sign with different turbulence modes such as ITG and TEM [40].

The radial gradient of the population density, $\partial\langle N\rangle/\partial r$, induces an inward radiative diffusive flux of wave momentum, which can be either co-current or counter-current direction, depending on the sign of $k_\parallel$. This

radiative diffusive flux can be also written in the form of $-D_r \partial \langle P_\parallel \rangle / \partial r$, where $\langle P_\parallel \rangle = k_\parallel \partial \langle N \rangle / \partial r$ is the parallel wave momentum density, and $D_r \sim v_{gr}^2 \tau_c$ is the quanta diffusivity [40]. The radial gradient of the residual stress works effectively as a local internal toroidal momentum source, referred to as the intrinsic torque [40]

$$\tau_{intrinsic} = -\frac{\partial}{\partial r} \left(m\bar{n}\Pi_\phi^{Res} \right) \tag{2.42}$$

In conclusion, residual stress is governed by the underlying turbulence and is a complicated function of the gradients of density, temperature, pressure, and current. The theoretical interpretation and analytical expression of the residual stress have been discussed. Relevant experimental studies are summarized in the following sections to present the current understanding of this subject.

2.5.1 Quantification of Intrinsic Torque

Previous experiments successfully demonstrated the existence of intrinsic torque by studying the change in rotation profile during L-H transitions in ohmic plasmas [50], modulating NBI to apply transient momentum transport analysis [48], and performing torque scan with co and counter neutral beams [18]. However, decoupling the three components in Reynolds stress is very difficult and one can argue that the observed rotation profile that can be explained by certain momentum diffusivity can also be explained by pinch, residual stress, or the combination of those terms.

To address this issue, experiments at DIII-D with unbalanced beam torque have achieved a near-zero flat toroidal rotation profile using 2 counter and 1 co-beam [18]. As depicted in Fig. 2.4(a), a flat rotation profile is observed, resulting in zero velocity and velocity gradient across the entire radial profile. In such cases, both the diffusive flux and the momentum pinch vanish, leaving only the residual stress.
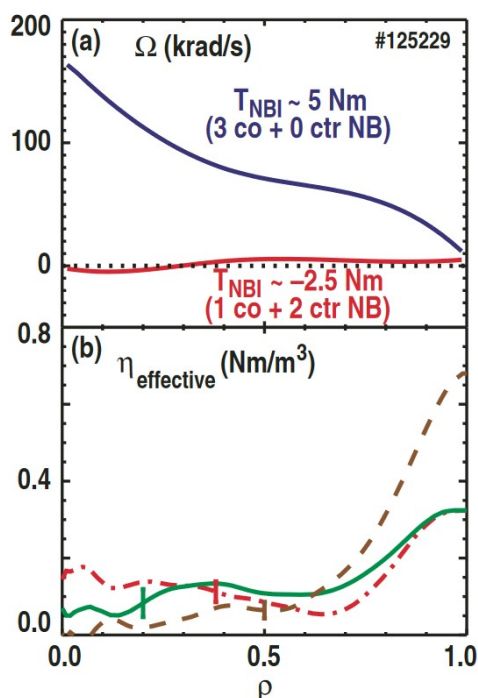
Figure 2.4: (a) Rotation and (b) the effective intrinsic torque profiles that are inferred differently based on the level and nature of anomalous fast ion transport: no anomalous fast ion diffusion (red), flat anomalous fast ion diffusion (green), and flat diffusion including additional non-ambipolar j × B torque (brown) [18]

Since the plasma is stationary with a non-evolving rotation profile, the net external momentum source from NBI must be counter-balanced by the internal momentum source generated by residual stress. In other words, a nonuniform residual stress produces an effective intrinsic torque in the co-Ip direction, with a magnitude equivalent to that of one beam [18].

Figure 2.4(b) demonstrates the effective intrinsic torque derived from the momentum balance between NBI driven flux and turbulent momentum flux. The torque profile of the neutral beam is calculated based on classical fast ion transport assumptions. The green and red curves represent different methods of calculating anomalous fast ion transport, while the brown curve includes additional considerations of the j × B torque. In

all scenarios, the derived intrinsic torque peaks at the plasma edge. This observation is consistent with theoretical predictions that residual stress is driven by strong edge gradients in the $E \times B$ velocity, resulting from parallel wavenumber symmetry breaking [18].

2.5.2 Correlation Between Rotation and Turbulence

The previous section has convincingly demonstrated the existence of intrinsic rotation in tokamak plasmas. This section investigates the correlation between intrinsic rotation and the underlying turbulence by studying an intriguing phenomenon observed in different devices called rotation reversal [51]. This rotation reversal refers to the change in the sign of rotation across specific critical plasma parameters in ohmic L-mode plasmas.

For instance, in divertor configurations, the core rotation shifts from co-current to counter-current as it crosses a critical density threshold, leading to a rotation reversal during density ramp-up [52]. Similarly, rotation reversal also appears while changing the plasma current, in which case the rotation is counter-current at low plasma current and co-current at high plasma current [53]. Additionally, an increase in the toroidal magnetic field beyond a certain magnitude induces rotation reversal as well, with counter-current rotation at high B_T and co-current rotation at low B_T [53].

All these critical plasma parameters are linked to plasma collisionality and coincide with the critical collisionality for the transition between linear ohmic confinement (LOC) and saturated ohmic confinement (SOC) [53]. The LOC-SOC transition is characterized by an increase in thermal energy confinement time with rising density until it reaches a saturation point, as shown in Fig. 2.5(a). This well-known plasma phenomenon has been extensively studied in many tokamaks [14, 54, 55, 56, 57].

Rotation reversals are consistently observed during the LOC-SOC transition [14], as shown in Fig. 2.5(b). Since there is no external momentum source, this change in rotation direction must be attributed to the plasma
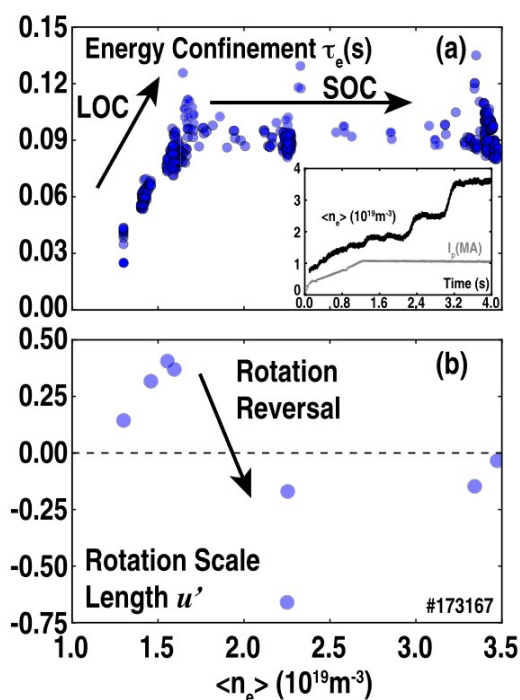
Figure 2.5: Observation of the LOC-SOC transition during a density ramp-up discharge with exclusive ohmic heating at DIII-D. (a) Energy confinement time, derived from the measured plasma profiles using TRANSP, alongside a time history of plasma density (shown in the lower right plot). (b) Carbon rotation gradient scale length at mid-radius [14]

itself. Considering that variations in turbulence viscosity χ_ϕ and momentum pinch V_{pinch} can only modify the profile shape but not produce net toroidal momentum, this observation strongly suggests a substantial shift in the residual stress and intrinsic torque in response to the changing plasma confinement regime.

Experiments at DIII-D utilize a slow density ramp-down across the narrow density range where both the LOC-SOC transition and rotation reversal occur. The results show that, at the beginning of the density ramp-down, toroidal rotation within $\rho < 0.6$ is in the counter-current direction with a hollow profile, corresponding to the SOC regime. As the density

continues to decrease, the core rotation reverses its direction to co-current with a flat profile, corresponding to the LOC regime. Additional electron heating is applied at the end of the density ramp-down, which drives the core rotation profile further toward the co-current direction. This alteration in the rotation profile correlates with the confinement regime transition from SOC to LOC [14].

The explanation is that ohmic heating and electron cyclotron heating (ECH) directly heat electrons and indirectly heat ions. At low density, the ions and electrons are thermally decoupled, and the majority of power flows through the electron transport channel. Because TEMs are dominant at low density, electron energy confinement is poor compared to ion energy confinement. When density increases, a larger fraction of power flows through the ion transport channel because the energy exchange between electrons and ions is proportional to $n_e^2(T_e - T_i)/T_e^{3/2}$. Since ions have better energy confinement, the stored energy increases when more and more power goes to ions [14]. The saturated energy confinement happens when sufficient energy flows through ions and eventually gives rise to ITG modes, which induces stiff ion and electron thermal transport [14].

Linear GYRO simulations were performed to identify the dominant turbulence mode during the LOC-SOC transition. As shown in Fig. 2.6(d), a mixture of ITG (blue) and TEM (red) is observed at high density, where ITG is the dominant instability but has a decreasing fraction as the radius increases. Figure 2.6(e) shows that as density drops, the TEM growth rate increases and becomes the dominant instability because the decreasing collisionality favors TEM. Figure 2.6(f) shows that when additional ECH is applied, ITGs completely disappear and TEMs dominate the entire k-spectrum [14]. The shift in the dominant turbulence mode could potentially explain the observed rotation reversal, as theory suggests that residual stress can change sign if the propagation direction of the underlying turbulence changes [40].
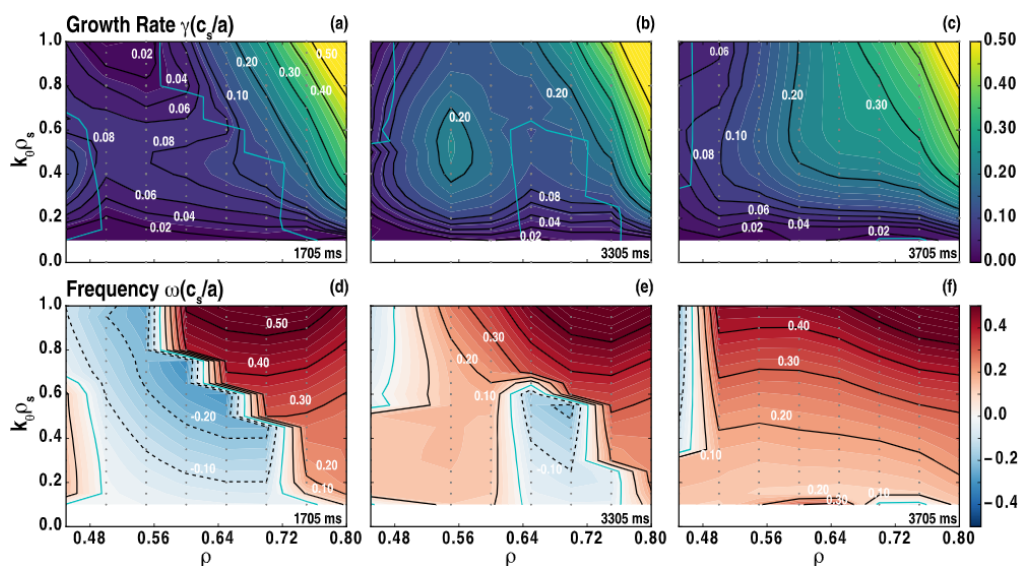
Figure 2.6: Evolution of the linear turbulence spectrum. Growth rate and frequency of the most unstable mode (a),(d) from 1705 ms at high density with ITG modes, (b),(e) from 3305 ms at low density with mostly TEMs, and (c),(f) from 3705 ms at low density with ECH and all TEMs. Ion direction modes are negative frequency (blue) and electron direction modes are positive frequency (red) [14]

Experimental evidence from other tokamaks also indicate that ion turbulence is predominant in the SOC regime and electron turbulence dominates in the LOC regime [57]. These observations suggest that, for LOC-SOC transition, the energy confinement is related to the change of the dominant instability, and rotation reversal is associated with the turbulence-driven residual stress generated by different turbulence modes. These observations and simulation results motivate the experimental design implemented in this thesis work. Various combinations of NBI and ECH are applied to alter the ion and electron heat fluxes, which changes the mixture of turbulence modes and thereby the resulting intrinsic torque. This approach is used to investigate the relationship between turbulence and flow generation.

2.5.3   Edge Momentum Source from the Residual Stress

To the best of our knowledge, no direct measurement of turbulent stresses and the resultant intrinsic torque in the tokamak plasma core has been achieved so far. Nevertheless, dedicated experiments have been performed in the Controlled Shear Decorrelation Experiment (CSDX) for cylindrical laboratory plasmas to quantify the turbulent Reynolds stress and investigate the relationship between turbulence and flow generation [58].

In this study, turbulent viscosity is expressed in terms of the radial velocity fluctuation, $\tilde{v}_r$, and the turbulence correlation time, τ_c, with $\chi_\theta = \langle \tilde{v}_r^2 \rangle \tau_c$. Assuming the convection pinch vanishes due to the azimuthal symmetry of plasma and the uniform magnetic field along the z-direction in a cylindrical configuration, the residual stress can be derived as [58]

$$\Pi_\theta^{Res} = \langle \tilde{v}_r \tilde{v}_\theta \rangle + \langle \tilde{v}_r^2 \rangle \tau_c \frac{\partial v_\theta(r)}{\partial r} \tag{2.43}$$

All terms in Eqn. (2.43) are measured in experiments. A 2D array of Langmuir probes is applied to measure the fluctuating plasma density, potential, and electric field. Turbulence characteristics and velocity fields are derived from the time-delay cross-correlation of the fluctuating quantities [59]. The measured Reynolds stress is shown in Fig. 2.7(b). The nonuniform Reynolds stress profile results from the radial variations in the turbulence intensity and the cross-phase relationship between radial and azimuthal velocity fluctuations.

Using the measured quantities in Fig. 2.7(a)−(d), a finite residual stress is identified, which locates at the plasma boundary, peaks at $r \sim 3.5$ cm, and changes sign near $r = 4.0$ cm, as shown in Fig. 2.7(e). The opposite signs indicate that the turbulent residual stress can act as both an energy sink and an energy source for the mean flow. This measured residual stress is validated by reconstructing the velocity profile via momentum balance equation and comparing it with the experimental measurement.
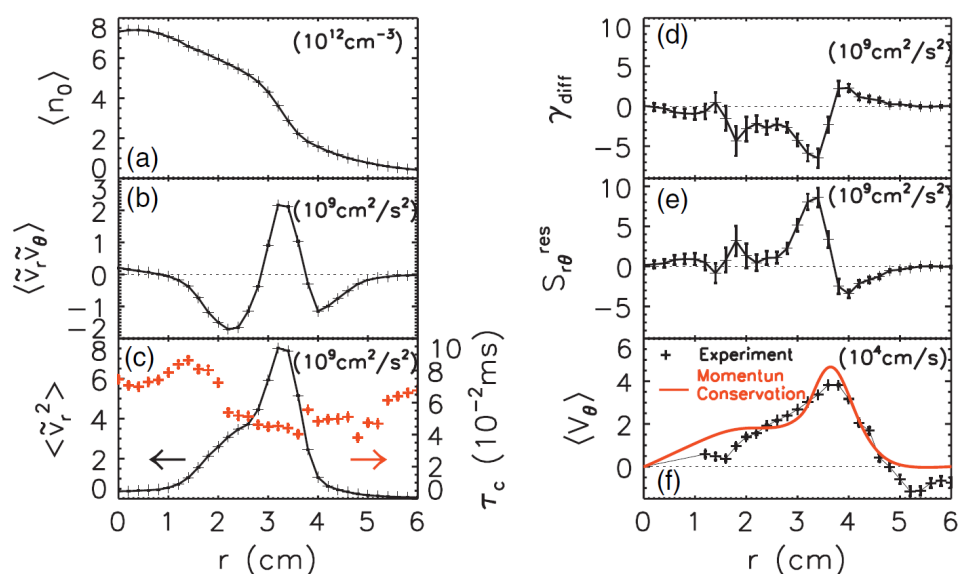
Figure 2.7: (a) Radial profiles of the mean density, (b) measured total azimuthal Reynolds Stress Π_θ^{RS}, (c) mean-squared radial turbulent velocity $\langle \tilde{v}_r^2 \rangle$ (black) and correlation time τ_C (red), (d) diffusive momentum flux $-\langle \tilde{v}_r^2 \rangle \tau_C \frac{\partial v_\theta(r)}{\partial r}$, (e) residual stress Π_θ^{Res}, (f) mean azimuthal flow $\langle V_\theta \rangle$ measured from experiment (black) and calculated from momentum conservation (red) at CSDX [58]

Figure 2.7(f) shows the reconstructed azimuthal velocity profile based on the measured residual stress, which shows good agreement with the experimental measurement.

Notably, turbulence stresses and toroidal flows within the separatrix of a tokamak H-mode plasma have been measured using a reciprocating multitip Langmuir probe at DIII-D [60]. Figure 2.8(a) and 2.8(b) show the toroidal momentum density near the separatrix. A strong co-current rotation layer is identified at the separatrix, followed by the development of co-current intrinsic rotation in the core. The measured Reynolds stress is effectively zero outside the separatrix and increasingly positive toward the inner region of the plasma [60], as shown in Fig. 2.8(c) and 2.8(d). However, these measurements have limited radial coverage, providing no data inside $\rho = 0.98$. The known Reynolds stress imposes a counter-

current torque onto the plasma core, which is in clear contradiction with the observed co-current core rotation development [60].

These findings provide valuable insights into the intricate structure of turbulent Reynolds stress and the resulting intrinsic torque. It is noteworthy that measuring turbulent stresses with Langmuir probes presents challenges due to their limited penetration depth and potential risk of perturbing the plasma. Therefore, in this research, we propose the use of spectroscopy diagnostics to measure fluctuation quantities, which are non-perturbing and offer extensive radial coverage.
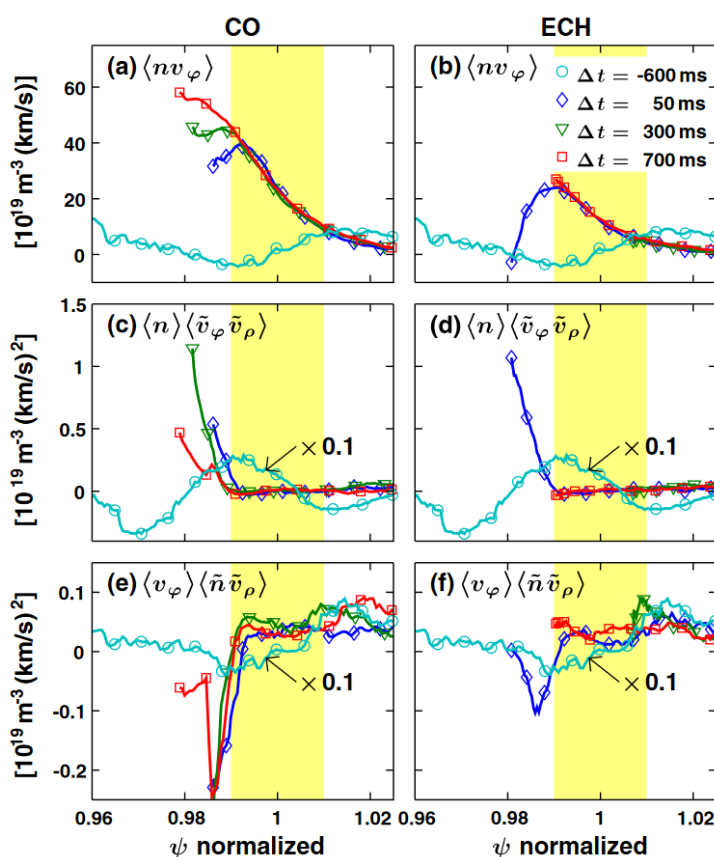
Figure 2.8: Edge profiles of (a),(b) the toroidal momentum density, (c),(d) the measured Reynolds stress, and (e),(f) the convective momentum flux in co-current NBI heated (left) and ECH heated (right) plasmas [60]

3   DEVICES, DIAGNOSTICS AND ANALYSIS TECHNIQUES

This chapter describes the tokamak device, diagnostic tools, and analysis techniques that are used in this thesis to study the various momentum transport mechanisms and the generation of intrinsic rotation. This chapter is structured as follows. An overview of the DIII-D tokamak is given in Section 3.1. The major diagnostic tools, Beam Emission Spectroscopy (BES) and Ultra-fast Charge Exchange Recombination Spectroscopy (UF-CHERS), are introduced in Section 3.2 and Section 3.3, including diagnostic hardware, noise-handling, and data processing.

These two sections also provide a comprehensive explanation of the analysis techniques utilized to characterize turbulence and calculate the turbulence-driven Reynolds stress. Radial and poloidal velocity fluctuations, $\tilde{v}_r$ and $\tilde{v}_\theta$, are inferred by BES velocimetry analysis, as demonstrated in Subsection 3.2.4. Toroidal velocity fluctuation, $\tilde{v}_\phi$, is derived from UF-CHERS data, as described in Subsection 3.3.2.

3.1   DIII-D

The DIII-D tokamak was commissioned in 1986 and upgraded from the Doublet III device [61]. It is designed to explore the benefits of noncircular plasma cross-section. Many field-shaping coils are employed to enable precise control of the plasma shape. DIII-D also provides flexible divertor configurations, facilitating the study of various plasma scenarios including limited, single-null divertor, and double-null divertor discharges [61].

A cross-section of the DIII-D tokamak, including contours of the flux surface of a representative lower single-null plasma, is shown in Fig. 3.1. Major components such as toroidal and poloidal field coils, field-shaping coils, and cryopumps are highlighted. The lower divertor, along with two upper divertors, is visible in the corners of the plasma chamber.
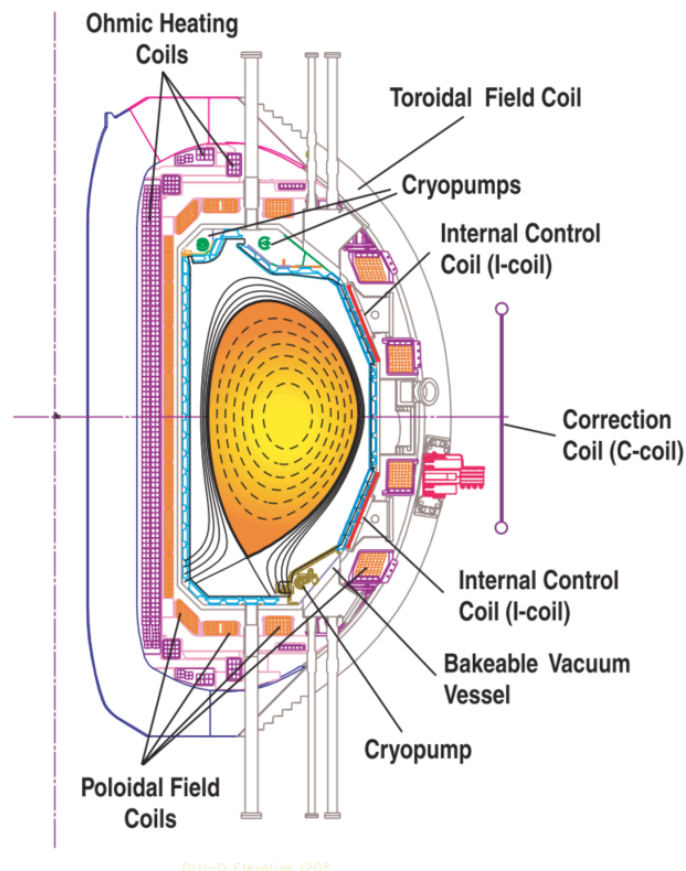
Figure 3.1: A cross-section of the DIII-D tokamak with an equilibrium reconstruction of a single-null discharge [61]

DIII-D has the capability to attain a wide range of plasma conditions and access various confinement regimes. The major DIII-D device parameters are presented in Table 3.1 and the range of important plasma parameters are summarized in Table 3.2. It's important to note that the plasma facing components are made of carbon because of their excellent heat conduction and erosion-resistant properties, but they also introduce impurities to the plasma. The naturally existing carbon impurities motivate and facilitate the development of carbon emission-based diagnostics but could also degrade the plasma confinement upon accumulation.

Table 3.1: DIII-D Characteristic Parameters [61]

Parameter	Symbol	Value
Plasma major radius	$R_0(m)$	1.66
Plasma minor radius	$a(m)$	0.67
Plasma height	$h(m)$	2.8
Plasma elongation	κ	$1.0 \sim 2.5$
Maximum magnetic field	$B_T(T)$	2.2
Maximum plasma current	$I_p(MA)$	2
Plasma initiation voltage	$V_1(V)$	3
Fuel gas		D, H, He
Wall material		Carbon
Wall coating material		Boron

Table 3.2: DIII-D Plasma Parameters [61]

Parameter	Simultaneous	Maximum
Electron temperature $T_e(keV)$	7.5	15
Ion temperature $T_i(keV)$	18	22
Density $n_e(\times 10^{20} m^{-3})$	1.0	3
Normalized density n_e/n_G	0.6	1.7
Confinement time $\tau_E(s)$	0.4	0.5
Normalized confinement H_{89p}	4.5	4.5
Plasma current $I_p(MA)$	2.25	3.0
Stored energy $W(MJ)$	4.2	4.2
Beta $\beta(\%)$	6.7	13
Normalized beta β_N	3.9	6.0
Fusion product $n\tau T(\times 10^{20} keV \cdot s \cdot m^{-3})$	7	7

Various auxiliary heating systems are employed at DIII-D. A set of four neutral beam injection systems is used to deliver up to 20 MW of heating power to the plasma at a maximum of 80 keV beam energy. Each beamline consists of two positive ion sources, labeled as left (L) and right (R). As shown in Fig. 3.2, the first two beamlines, 30° and 330°, are fixed on-axis co-injected beams that can deliver 10 MW of power. The third 150° beamline can be adjusted from 0° to 16.4° away from the horizontal plane and deliver 5 MW of co-injected power. The last 210° beamline is off-axis
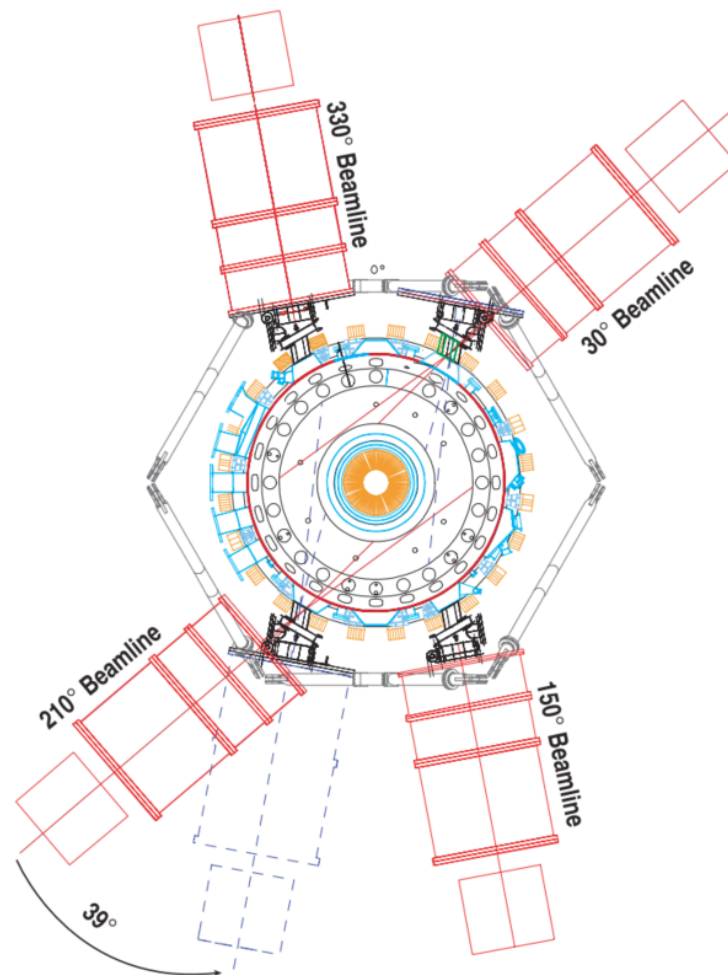
Figure 3.2: A top view of the four NBI systems in DIII-D [61]. The 150° beamline is used for BES and UF-CHERS diagnostics. The dashed line for the 210° beamline indicates that it can rotate to the counter-current direction, which provides the capability to adjust the net-injected torque.

by 18.4° and can rotate 39° to change from co-injection to counter-injection, which can be used to control the net injected torque [61].

These features are particularly important and beneficial for rotation studies. Many experiments in DIII-D employ balanced beams to control the total injected torque, achieve specific rotation profiles, or conduct

torque scans. Besides particle fueling, heating and rotation control, NBI
also provides the necessary emission sources for various spectroscopy
diagnostics, including BES and UF-CHERS.

In addition to NBI, a 110-GHz EC frequency power system is available
that can couple up to 3 MW of power at the second harmonic of the electron
cyclotron frequency to the plasma, which is helpful for localized heating,
current drive, and neoclassical tearing mode stabilization [62].

An extensive set of diagnostics is available on DIII-D. More than 50
instruments are designed, operated, and maintained by many groups from
different institutions [61]. The primary diagnostics used for this thesis,
BES and UF-CHERS, are introduced in detail in later sections. Other impor-
tant diagnostics for this thesis include Charge Exchange Recombination
(CER) spectroscopy for ion temperature and toroidal rotation profiles
[63], Thomson scattering diagnostic for electron density and temperature
profiles [64], Electron Cyclotron Emission (ECE) diagnostic for electron
temperature profiles [65], and magnetic diagnostics for equilibrium re-
construction [66].

3.2   Beam Emission Spectroscopy

The Beam Emission Spectroscopy (BES) diagnostic was first developed on
TFTR and is now featured on DIII-D and several other tokamaks worldwide
[67, 68, 21, 69, 70]. BES measures spatially localized, long wavelength
density fluctuations with $k_\perp \rho_i < 1$ at a typical frequency range of $10 \sim 400$
kHz. To cover the desired range of wavenumber and frequency, the DIII-D
BES diagnostic system is designed to achieve a spatial resolution of $\Delta x \sim 1$
cm and a temporal resolution of $\Delta t = 1$ μs [21].

BES detects the Doppler-shifted D_α emission in the range of 652 to
655 nm, originating from excited deuterium atoms produced by neutral
beam injection during the $n = 3 \rightarrow 2$ transition [21]. The Doppler shift

observed from the fast-moving beam neutrals separates the signal from the background D_α light. A diagram of BES viewing geometry and major components is shown in Fig. 3.3. The DIII-D BES light collection optics are viewing towards the neutral beam, which introduces a blueshift to the observed neutral beam D_α emissions [21].
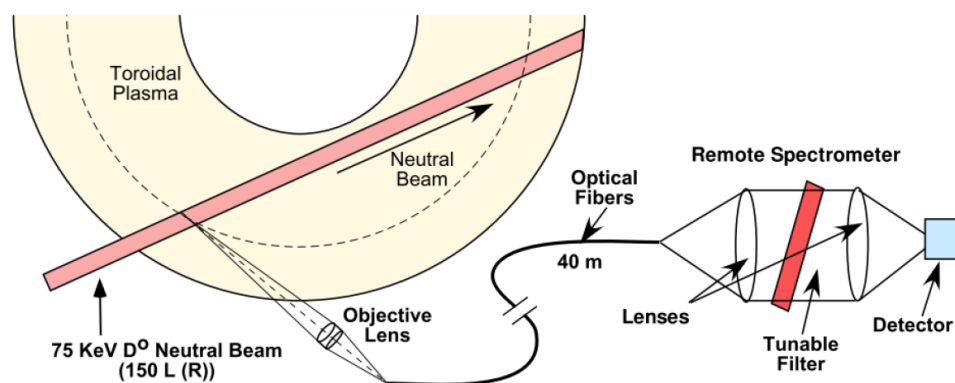
Figure 3.3: A diagram of BES viewing geometry and major components [71]

As shown in Fig. 3.3, emission lights are collected by a f/2, 40 cm diameter objective lens and projected onto an array of 64 fiber bundles which can be reconfigured based on requirements [21]. The optical sightline is aligned to intersect with the neutral beam at a location nearly tangential to a magnetic flux surface to provide good spatial resolution in the radial-poloidal plane. Each BES channel consists of eleven 1-mm optical fibers arranged in a 4:3:4 configuration (see Fig. 3.15), covering an area of approximately 2.9 mm horizontally by 4.2 mm vertically on the lens image plane. The 40-meter fiber bundles then transmit the collected light from the tokamak to detectors that are located in a separate diagnostic lab.

Within the detector, an optical system collimates, filters (with a 3 nm bandpass $\lambda_0 = 654$ nm interference filter), and focuses the light onto PIN photodiodes which convert the D_α light signals into current signals that vary with beam power and plasma density and are typically on the order of ~ 10 nA [21]. These current signals are then converted to voltage signals

through high-gain low-noise preamplifier circuits, which are further amplified by signal conditioning electronics and digitized at a sampling rate of 1 MHz [72]. The measured photon emission fluctuation is related to the local plasma density fluctuation by $\tilde{I}/I = C\tilde{n}/n$, where C is a function of the neutral beam energy E_{NBI}, plasma density n, electron temperature T_e, ion temperature T_i, and the effective charge Z_{eff} [67]. In the typical range of plasma density and temperature, this conversion factor has been calculated to be approximately $C \approx 0.5$.

Currently, there are 64 BES channels available at DIII-D, which cover a wide region of 8 (radial) × 12 (poloidal) cm from the scrape-off layer (SOL) to the plasma core. The channel arrangement can be customized by inserting fibers on a flexible 2D motorized fiber-mounting array. This fiber array can be scanned radially to observe different spatial regions of the plasma on a shot-to-shot basis [73]. Figure 3.4 illustrates the BES channel arrangement applied in the DIII-D experiment presented in this thesis.
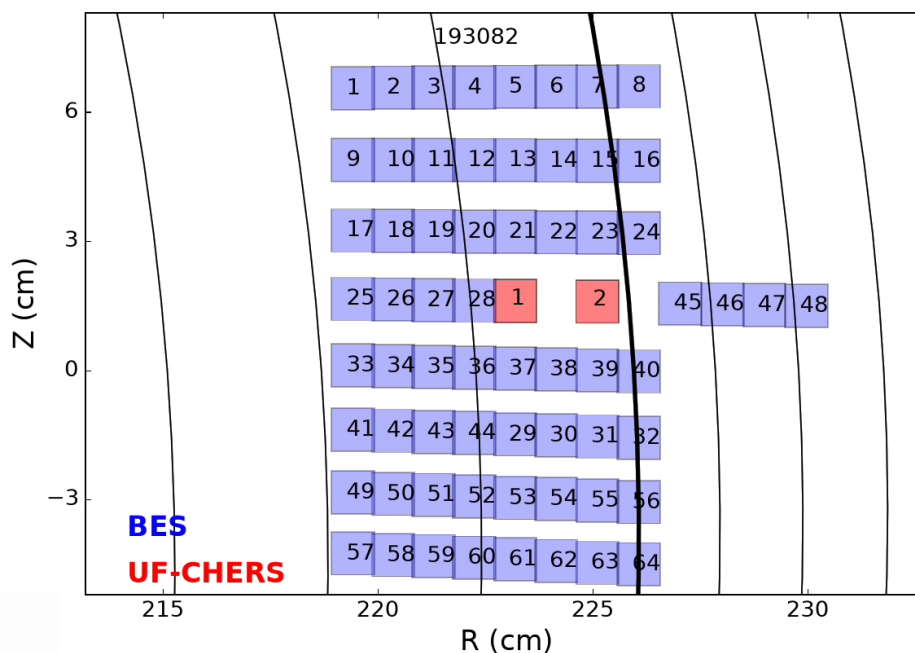
Figure 3.4: BES and UF-CHERS channel arrangement for DIII-D discharge 193082

3.2.1 BES Signal and Noise Handling

To accurately process BES data and interpret turbulence measurements, it is crucial to comprehend the primary noise contamination sources in the BES signal. These sources include amplifier noise $\tilde{n}_{amp}$, photon noise $\tilde{n}_\gamma$, upstream noise $\tilde{n}_{upstream}$, and beam noise $\tilde{n}_{beam}$ [74]. In general, the measured BES signal $\tilde{S}(t)$ can be expressed as the summation of the interested turbulence fluctuation signal, $\tilde{f}$, and various noise sources since they are mutually uncorrelated [74]

$$\tilde{S}(t) = \tilde{f}(t) + \tilde{n}_\gamma(t) + \tilde{n}_{amp}(t) + \tilde{n}_{beam}(t) + \tilde{n}_{upstream}(t) \qquad (3.1)$$

The amplifier noise and photon noise are incoherent noise. Amplifier noise, or dark noise, is a type of incoherent noise introduced by the amplifier circuit. Thermal motion of the electrons in the feedback resistor and thermal effects within the amplifier itself result in voltage noise, $\tilde{v}_a$, and current noise, $\tilde{i}_a$. Those two effects induce a total noise current of $\tilde{i} = \tilde{i}_{v_a} + \tilde{i}_a$, where $\tilde{i}_{v_a} = \tilde{v}_a C_d f$ and C_d is the photodiode capacitance. Therefore, the amplifier noise increases with frequency in the power spectrum. Another source of the amplifier noise is the flicker noise, which has a $1/f$ power spectral density dependency and therefore is most pronounced at low frequencies. Amplifier noise is identified by the auto-power of the dark measurement, as shown in Fig. 3.5.

Photon noise is a statistical noise associated with the photocurrent produced at the detector photodiode due to the discrete nature of the photon flux. The counting of discrete charge carriers follows Poisson statistics. Photon noise has a uniform power distribution in the frequency space. The magnitude of photon noise depends on the direct current I_{DC} and bandwidth B, with $\tilde{I}_{RMS}/I_{DC} = \sqrt{2eB/I_{DC}}$. Due to their incoherent nature, photon noise and amplifier noise can be largely suppressed by taking the cross-power between channels, provided that the optical light throughput
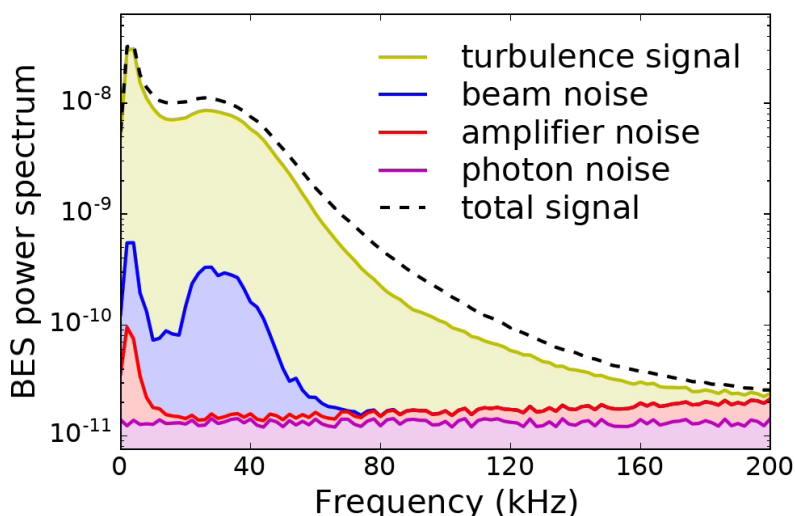
Figure 3.5: Power spectrum of the BES turbulence signal and noise sources collected from DIII-D discharge 193082 at $\rho = 0.96$ and t $= 3.0 - 5.0$ s

is sufficiently high to ensure a high signal-to-noise ratio. As shown in Fig. 3.5, the turbulence signal is estimated using the cross-power between poloidally adjacent channels. The total incoherent noise is estimated as the difference between the auto-power and the cross-power. The contribution of photon noise is then identified by subtracting the previously determined amplifier noise from this total incoherent noise.

The upstream noise and beam noise are coherent noises. Upstream noise is introduced by the beam attenuation caused by interactions with plasma ions and electrons as the neutral beam penetrates the plasma. Due to the time dependence of the plasma density fluctuations, the beam attenuation also exhibits a time dependence, proportional to an appropriated weighted sum of all the plasma density fluctuations in the upstream regions. This modulated beam intensity propagates into the plasma and can be observed in the downstream regions. The upstream noise can be identified through correlations between radially distant channels using two-pair analysis or four-pair analysis [74]. In most cases, the contribution of upstream noise only becomes significant for channels that are located

deeper in the plasma radially when strong edge fluctuations are present. Since the noise spectrum presented is obtained from BES channels near the edge at $\rho = 0.96$, upstream noise is not included in the figure.

The beam noise is introduced by fluctuations in the neutral beam density due to the oscillation of beam power supplies. Capacitance mismatching in the beam power supplies results in modulation of beam intensity by two harmonic frequencies at DIII-D, 360 Hz (dominant) and 60 Hz (subdominant), with ripples that extend up to 50 kHz. The inherent beam noise can be removed from the raw data through comb-filtering of certain fundamental frequencies, in which the data at the integer multiples of fundamental frequencies are replaced by the average power near the harmonic. As shown in Fig. 3.5, the beam noise is estimated using the cross-power between channels that are both radially and poloidally distant. This ensures that they do not share any turbulence signal or upstream noise, thereby isolating the beam noise.

3.2.2 Spatial Localization of the BES Measurements

The BES system measures the Doppler-shifted D_α light emissions in a 3D sample volume, which is determined by the intersection of the beamline and the optical sample volume of the collection optics relative to the magnetic geometry. The point spread function (PSF) is used to describe this spatial localization of the BES measurement and is influenced by various factors, including the beam sight line geometry, magnetic flux surface geometry, local magnetic field pitch angle, local plasma density, local beam density, and atomic transition rates.

The determination of the PSF is essential for a proper interpretation of the BES data. The measured intensity distribution, $M(\mathbf{x})$, of an optical system is written as the convolution of the true intensity function (e.g.

spatial emissivity profile of the plasma), $I(\mathbf{x})$, with the PSF, $P(\mathbf{x})$, [75]

$$M(\mathbf{x}) = I(\mathbf{x}) * P(\mathbf{x}) \tag{3.2}$$

where $\mathbf{x}$ is the 3D spatial coordinate. The calculation of PSF is simplified from a 3D problem to a sequence of 2D calculations on successive image planes [75]. Figure 3.6 shows a series of 1D projections of the point spread functions in the direction perpendicular to the optical axis in the mid-plane. Multiple image delocalization effects are considered through convolutions of the image functions. After each convolution, the resulting image function is normalized to conserve the total light intensity passing through each circular cross-section [75].
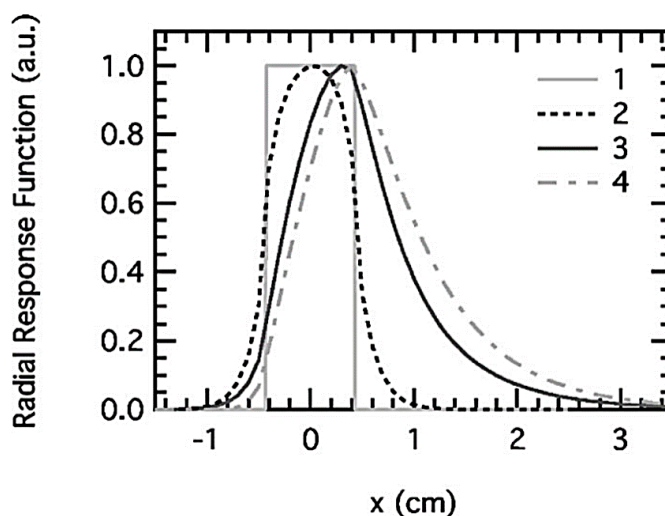
Figure 3.6: (1) Cross sections of magnified fiber image. (2) Convolution of fiber image with circular cross sections of light cone along optical axis and neutral beam profile. (3) Convolution of image function with finite lifetime effects. (4) Point spread function transformation into tokamak geometry [75]

In Fig. 3.6, Trace 1 shows the radial projection of the PSF from the magnified fiber image, which is obtained through a 2D convolution between the rectangular image collected by the fiber bundle and the circular cross-section of the light cone produced by the objective lens [75].

Trace 2 shows the effects of beam density profile. The neutral beam at DIII-D has a Gaussian width profile with a vertical Full Width at Half Maximum (FWHM) of 27 cm and a horizontal FWHM of 13 cm. This beam density profile determines the resulting light intensity at each location within the plasma [75].

Trace 3 shows the beam smearing effect. The excited beam atoms, which generate the observed emissions, move a finite distance before decaying due to their finite excited lifetime and high velocity. This movement results in spatial delocalization along the direction of beam injection. A multistate collisional radiative model is applied to estimate this effect [75].

Trace 4 shows the projection of the image function transformed from the lab frame to the tokamak coordinate. Since turbulence eddies are elongated along the magnetic field lines, the diagnostic optical axis is angled by about 5° relative to the mid-plane and aligns with the magnetic field pitch angle to obtain higher spatial resolution of turbulence measurements in the plane perpendicular to the magnetic field. However, variations in the q profile, magnetic field configuration, and measurement's radial location may cause slight deviations between the magnetic field pitch angle and the diagnostic viewline. These variations are compensated by the coordinate transformation of image functions [75].

Figure 3.7 shows the 2D point spread functions for BES channels at different radial locations, calculated with experimental measurements from DIII-D discharge 173400 [76]. The radial and poloidal widths of the diagnostic sample volume are defined as the nominal FWHM of the PSF in the corresponding directions. Notably, the radial width is 1.8 cm for BES, while the ideal fiber image width is 0.9 cm. This radial extension primarily results from the beam smearing effect. In the poloidal direction, the PSF FWHM is 1.3 cm for BES, close to the ideal fiber image height of 1.2 cm. These effects impose an upper limit on the wavenumber ($k \leqslant 3$ cm^{-1}) of the turbulence that BES can measure.
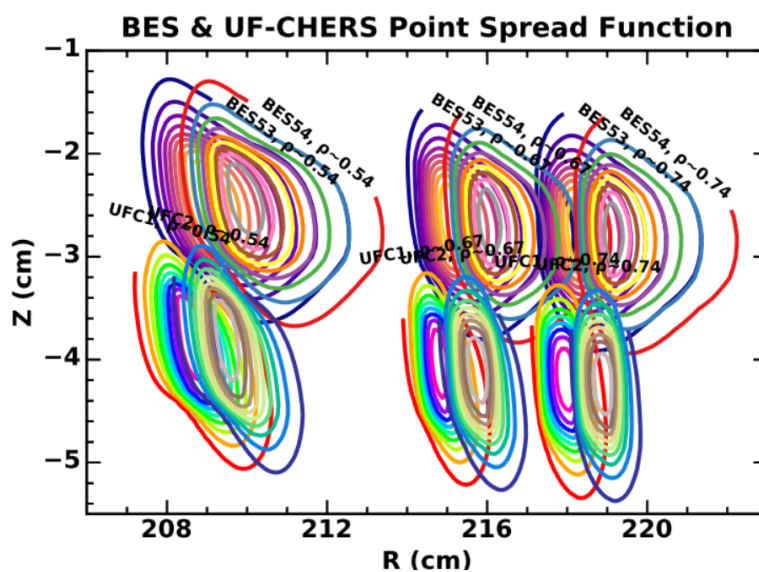
Figure 3.7: Example of point spread function for BES (upper) and UF-CHERS (lower) channels on DIII-D [76]

3.2.3 Analysis Techniques

There are two common analysis techniques for BES data, cross-spectral and cross-correlation analyses. In cross-spectral analysis, the auto-power spectrum represents the power associated with frequency for a single channel, denoted as 'a', and can be expressed as [74]

$$P_{a,a} = |F[I_a(t)]|^2 \tag{3.3}$$

where F represents the Fourier transform. The auto-power spectrum calculated from the Fourier transform of a single measurement typically has a large statistical error from photon and amplifier noise. To overcome this problem, the bin-averaging technique based on the central limit theorem is applied to reduce the uncertainty [74].

The central limit theorem states that for a population with a mean μ and standard deviation σ, when sufficiently large random samples are taken from the population with replacement, the distribution of these

sample means will approximate a normal distribution. This holds true regardless of the population's original distribution shape, provided the sample size is large enough.

Based on this theorem, the bin-averaging technique divides a large data sequence into many smaller overlapping subsequences of equal length called bins. For each bin, the auto-power spectrum is calculated using the Fourier transform. The results from these bins are then averaged, leading to a more reliable estimate of the power spectrum. With the assumption of stationarity in data, all subsequent Fourier-transform-determined auto-power spectra are expected to be identical. Therefore, the average of all auto-power spectra is equal to the underlying spectrum, but the variance is greatly reduced due to the central limit theorem. For a sufficiently large number of bins N, the variance associated with each frequency component decreases as N^{-1} [74]. However, as a trade-off, each bin will have a reduced number of samples. Therefore, the frequency resolution of the resulting auto-power spectrum will also be reduced.

The cross-power spectrum is defined as the common power shared by two different channels, 'a' and 'b', and can be expressed as [74]

$$P_{a,b} = \langle F[I_a(n\Delta t)] \cdot F[I_b(n\Delta t)]^* \rangle \tag{3.4}$$

where * represents the complex conjugate and $\langle \rangle$ means averaging over all bins. The cross-power can be used to calculate additional metrics, such as coherence $\gamma_{a,b}$ and cross-phase $\phi_{a,b}$ [74]

$$\gamma_{a,b}(\omega) = \frac{|P_{a,b}(\omega)|}{[|P_{a,a}(\omega)| \cdot |P_{b,b}(\omega)|]^{1/2}} \tag{3.5}$$

$$\phi_{a,b}(\omega) = \tan^{-1}\left[\frac{\mathrm{Im}(P_{a,b}(\omega))}{\mathrm{Re}(P_{a,b}(\omega))}\right] \tag{3.6}$$

Coherence represents the fraction of common power in channel 'a' and channel 'b'. The magnitude of coherence between the most adjacent

channels typically reflects the strength of turbulence fluctuations, while the spatial variance of coherence among radially and poloidally separated channels provides insights into the spatial structure of the turbulence [74].

Cross-phase represents the phase lag between the common power shared by channel 'a' and channel 'b'. Since the channel spatial separation is fixed and the various modes within turbulence move as a packet at the same speed, modes with higher frequencies have a larger phase lag. Therefore, the sign and magnitude of the cross-phase slope infer the turbulence propagation direction and phase velocity. For $P_{a,b} = \langle F[I_a] \cdot F[I_b]^* \rangle$, if the slope of cross-phase is positive, channel 'a' leads in phase and the propagation direction is $a \to b$. Vice versa, a negative slope of the cross-phase indicates that channel 'b' leads in phase, and the propagation direction is $b \to a$ [74]. The cross-phase spectrum is particularly important for distinguishing turbulence modes since it reflects the magnitude and direction of turbulence flow in the laboratory frame.

Figure 3.8 provides an example of cross-spectral analysis results from DIII-D BES data of discharge 193082. In Fig. 3.8(a), the arrangement of the BES channels is displayed, with BES37 as the reference channel (channel 'a') and BES29/53/61 as the target channels (channel 'b'). The cross-power spectrum in Fig. 3.8(b) and the coherence spectrum in Fig. 3.8(c) show a prominent peak and a maximum coherence of 0.8, suggesting that high-quality turbulence signals are obtained. The coherence spectrum further reveals that the frequency range of this turbulence lies between 10 and 150 kHz, which provides important information for the following cross-correlation and velocimetry analysis.

Finally, in Fig. 3.8(d), the monotonic increasing cross-phase indicates a downward turbulence propagation in the lab frame, which is the electron diamagnetic direction based on the magnetic field configuration employed in this specific plasma. Notably, the presence of cross-phase jumps between π and $-\pi$ is a direct consequence of the arctan function and is not

associated with any changes in the turbulence. In the calculation of turbu-
lence phase velocity using the slope of the cross-phase, this jump between
π and $-\pi$ is corrected to ensure continuity in the cross-phase.
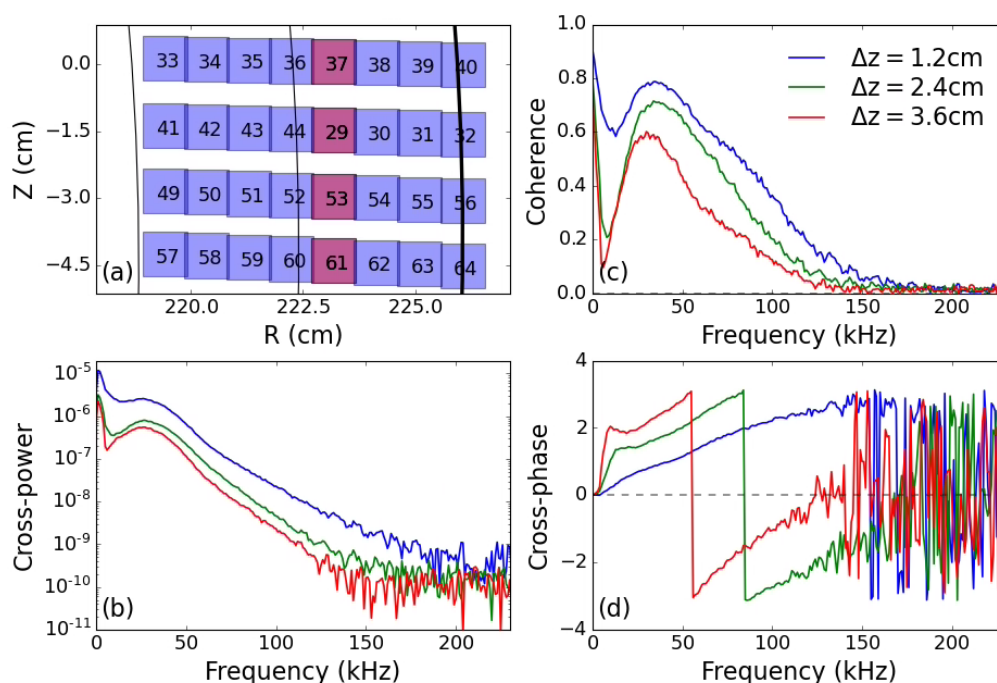
Figure 3.8: Example of spectral analysis results for DIII-D BES data, including (a)
BES channel arrangement, (b) cross-power, (c) coherence, and (d) cross-phase

Cross-correlation is applied as a more advanced analysis technique
to examine turbulence structures. Correlation coefficient $\rho_{a,b}(\tau)$ between
two channels measures their similarity as a function of time delay τ. Corre-
lation analysis is applied to estimate the spatiotemporal characteristics of
turbulence, including phase velocities, group velocities, correlation length
L_c, and correlation time τ_c. The correlation coefficient can be calculated
using the time-delayed correlation function $C_{a,b}(\tau)$ [74]

$$\rho_{a,b}(\tau) = \rho(\Delta x, \tau) = \frac{C_{a,b}}{[C_{a,a}(0) \cdot C_{b,b}(0)]^{1/2}} \tag{3.7}$$

where $C_{a,b}$ can be expressed as the real part of the inverse Fourier transform of the cross-power spectrum [74]

$$C_{a,b}(\tau) = \langle \tilde{I}_a(t) \cdot \tilde{I}_b(t+\tau) \rangle = \text{Re}\langle F^{-1}[P_{a,b}(\omega)] \rangle \qquad (3.8)$$

The auto correlation at zero time delay $C_{a,a}(0)$ is equal to the total auto-power, $C_{a,a}(0) = \sum_i P_{a,a}(\omega_i)$. The correlation envelope $A[\rho(\Delta x, \tau)] = \sqrt{\rho^2 + H(\rho)^2}$ is calculated to obtain the total correlation, where H stands for Hilbert transform [74]. Figure 3.9(a) shows an example of the correlation coefficients and their envelopes. In practice, turbulence parameters are estimated using correlation results between a reference channel and multiple spatially separated channels either along the radial or poloidal direction. The time lag τ_{max} is defined as the time delay where the corre-
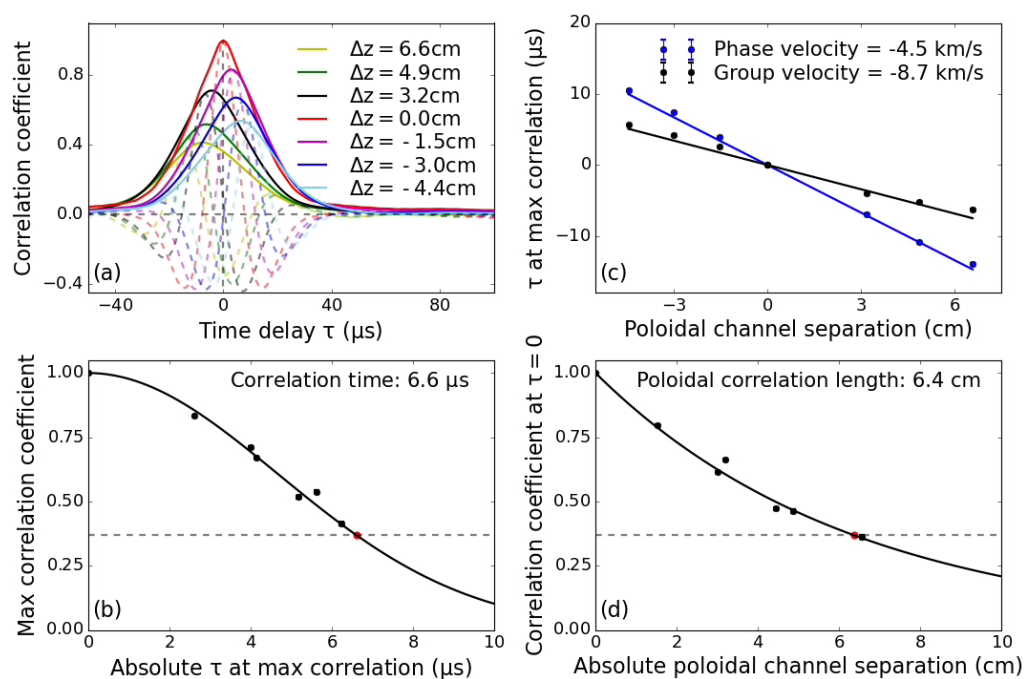
Figure 3.9: Example of cross-correlation analysis results for DIII-D BES data, including (a) correlation coefficients and their envelops, (b) correlation time, (c) group and phase velocity, and (d) correlation length

lation coefficient or its envelope is maximized. The corresponding value of the envelope is called the maximum correlation coefficient A_{max}.

Turbulence propagation velocity is calculated simply by taking the ratio of channel separation and time delay τ_{max}, as shown in Fig. 3.9(c). Using τ_{max} from the correlation function yields phase velocity and using τ_{max} from the correlation envelope yields group velocity. The correlation length L_c is defined as the distance where the maximum correlation coefficient $A_{max}(\Delta x)$ falls to $1/e$ of its original value as channel separation increases [74], as shown in Fig. 3.9(d). Similarly, the correlation time τ_c is defined as the time it takes for the maximum correlation coefficient $A_{max}(\tau)$ to fall to $1/e$ as time delay increases, as shown in Fig 3.9(c).

3.2.4 Velocimetry

Velocimetry is applied to density fluctuation images obtained by BES to derive the 2D turbulent fluctuating velocity field, $\tilde{v}_r$ and $\tilde{v}_\theta$, and therefore the Reynolds Stress. A particular velocimetry technique called orthogonal dynamic programming (ODP) is used due to its good spatial resolution, accuracy, and capability to resolve amorphous structures [77]. The ODP algorithm determines the optimal displacement map between two subsequent density fluctuation images and divides it by the time separation to derive the velocity field.

As shown in Fig. 3.10, two subsequent images I_0 and I_1 are divided into parallel overlapping strips. The corresponding strips in two images are aligned by minimizing the Minkowski distance L_n [77]

$$L_n = \sum_{i,j} |I_0(i,j) - I_1(i,j)|^n \tag{3.9}$$

where $I_0(i,j)$ represents the pixel point at the i-th row and j-th column in image 0, I_1 represents image 1, and n is typically taken to be 1 or 2.
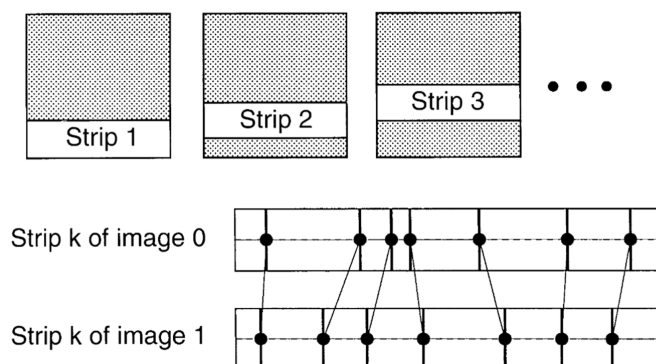
Figure 3.10: Image slicing and strip alignment to find optimal match [77]
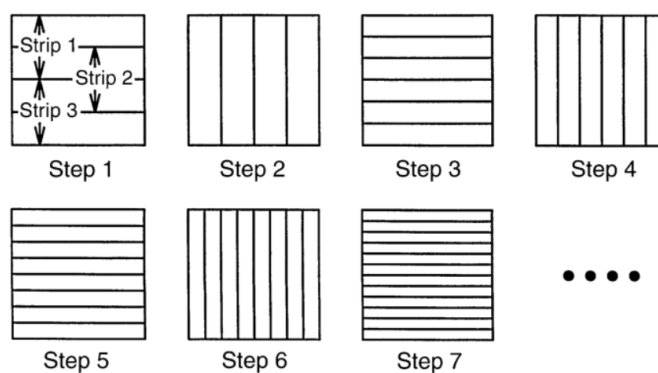
Figure 3.11: Strip configuration at different iterations using ODP [77]

Minimizing the sum of separation distances over all pixels provides a displacement map $(v_x(i,j), v_y(i,j))$ that best matches the two strips. This displacement map is then used to calculate an initial low spatial resolution estimate of velocity in the slicing direction. This initial estimate is applied to deform image 1 to match image 0, resulting in a new image, $I_1' = I_1(i + v_x(i,j), j + v_y(i,j))$. The new image I_1' and I_0 are then sliced into strips in a direction orthogonal to the first. The same procedures are repeated along alternating orthogonal directions using progressively narrower strip widths in each iteration to refine the displacement map $(v_x(i,j), v_y(i,j))$ [77], as shown in Fig. 3.11.

Ensuring the accuracy of the velocimetry analysis is essential for calculating the Reynolds stress, which constitutes the primary research objective of this thesis. To evaluate the performance of the ODP algorithm, synthetic turbulence images with a prescribed flow field are generated and analyzed in previous work [78]. The synthetic turbulence images are created to simulate the experimentally measured broadband turbulence data.

An example of synthetic turbulence images and the inferred velocity field at a single frame is shown in Fig. 3.12(a), where the red and blue colors in the background indicate positive and negative density fluctuations, and the overlaid arrows represent the derived velocities. Figure 3.12(b) shows the comparison between the estimated flow field and the imposed flow field. The mean flow and wavenumber are correctly estimated but the amplitude is slightly underestimated.

The ratio of the estimated velocity to the imposed velocity is defined as the transfer function in velocimetry analysis [78]. The transfer function has been extensively investigated using synthetic data. The simulation results show a strong dependency of the transfer function on both the turbulence wavenumber k_x and the signal-to-noise ratio (SNR) [78].
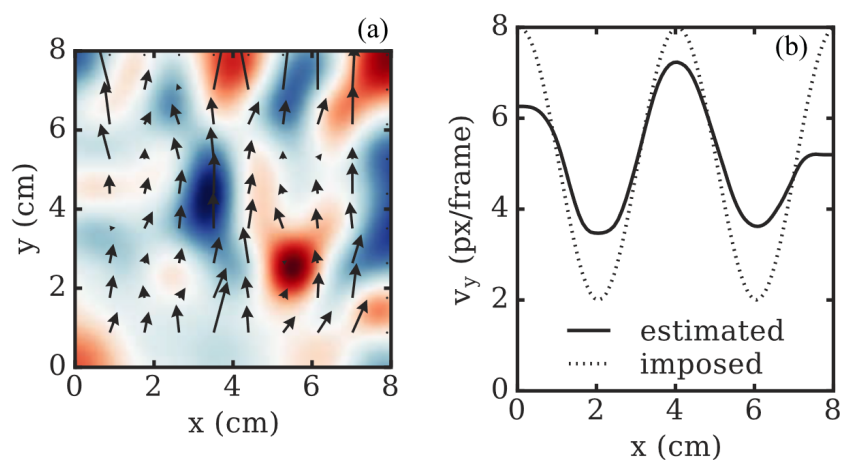
Figure 3.12: Velocimetry results for (a) synthetic turbulence images with prescribed flow field and (b) time and poloidally averaged flow profile [78]

Figure 3.13(a) shows that the ODP algorithm has good accuracy at low k_x but rapidly loses sensitivity as k_x increases. The sensitivity of the ODP algorithm on SNR is evaluated at a specific wavenumber of $k_x = 1.57$ cm^{-1}. As shown in Fig. 3.13(b), the ODP algorithm has good performance when SNR is above 10, degrades significantly when SNR falls below 10, and eventually becomes completely random at SNR < 1. These results elucidate the wavenumber limitation ($k_x \leqslant 2 \ cm^{-1}$) and SNR requirement (SNR $\geqslant 10$) for using the velocimetry analysis to infer the fluctuating flow field induced by turbulence[78].
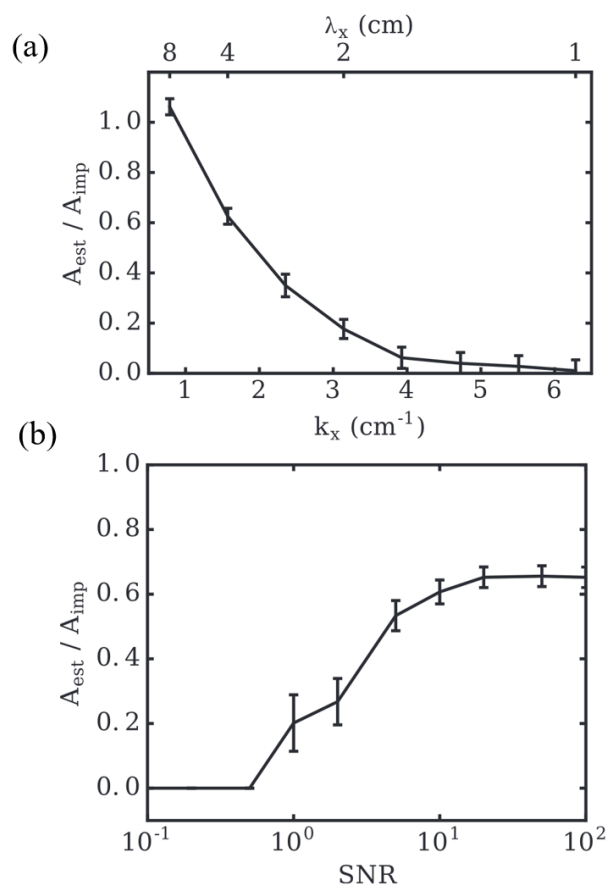
Figure 3.13: Dependence of the velocimetry-estimated flow amplitude, normalized by the imposed flow, on (a) radial wavenumber k_x, and (b) SNR [78]

To maximize the signal-to-noise ratio in BES data, the density fluctuations are filtered to pass the frequency range where the majority of turbulence data is located at [71]. This frequency range is typically consistent for channels along the poloidal direction but varies across the radial direction, due to different Doppler shifts from plasma rotations and variations in the underlying turbulence properties. To determine the appropriate frequency filter, coherence spectra from cross-power analysis between poloidally adjacent channels are often used.

To further improve the signal-to-noise ratio, the 2D turbulence images measured by BES can also be interpolated over space and averaged over time to suppress spurious displacement vectors and random noise, introducing the smoothing width and multi-frame factor [78].

The smoothing width defines the number of points in a boxcar smoothing function used in each iteration. A larger smoothing width is more effective in suppressing spurious displacement vectors but also averaging out the small spatial structure of the turbulent flow field. Meanwhile, the multi-frame factor sets the number of images used to estimate a single flow field. Increasing the multi-frame factor suppresses random noise but also decreases the spectral resolution by averaging out the velocity fluctuations at higher frequencies.

The impact of these two important input parameters is investigated using synthetic data with varying turbulence wavenumber and flow amplitudes [78]. To quantitatively evaluate the accuracy of the ODP results, two types of errors are characterized, bias error and random error. Bias error is defined as the discrepancy between the estimated and imposed flow amplitudes, while random error is defined as the standard deviation of the estimated flows.

It has been observed that increasing the multi-frame factor in the velocimetry algorithm leads to an increase in bias error but a reduction in random error [78]. On the other hand, increasing the smoothing

width initially reduces both bias and random error, but this effect plateaus for smoothing widths exceeding approximately 1.5 channel widths [78]. These findings provide valuable insights into the optimization of input parameters for the velocimetry algorithm based on the specific turbulence characteristics and research objectives.

Figure 3.14 shows an example of real turbulence images with red for positive and blue for negative density fluctuations [22]. The data is collected from an approximately 5.5×7 cm region near the outboard midplane of an L-mode discharge. To illustrate the gradual evolution of the turbulent eddies and the derived flow field (superimposed arrows), every fourth original image is displayed. Results show that the evolution of turbulence eddies is consistent with the derived flow field [22].
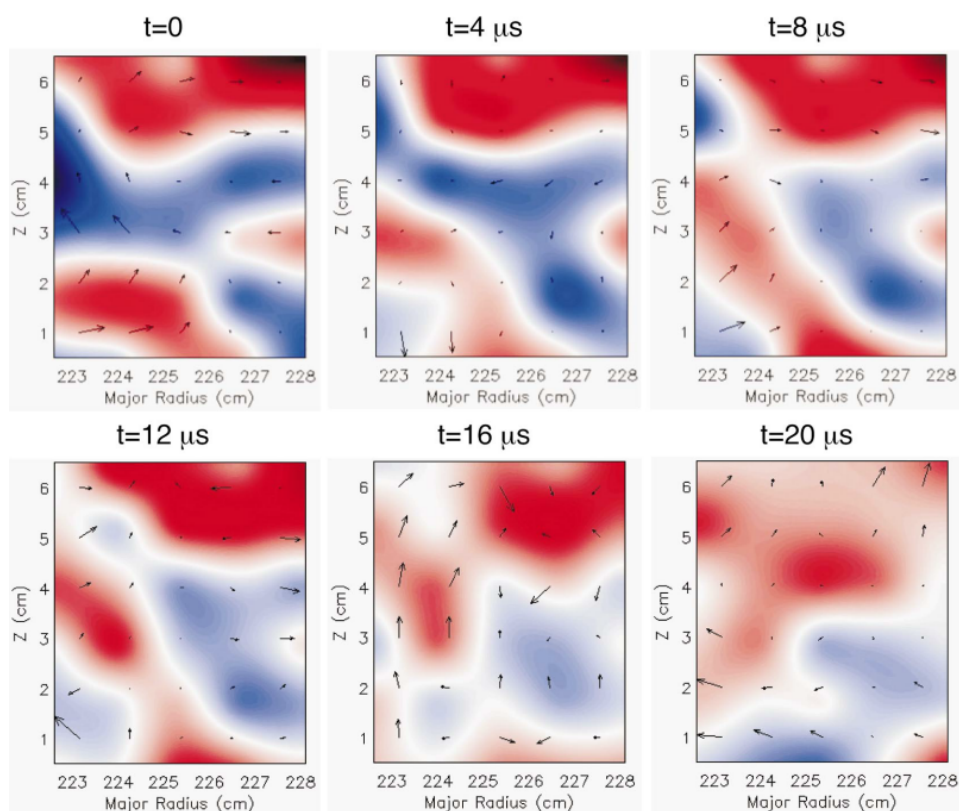
Figure 3.14: Turbulence images with superimposed velocity field [22]

3.3 Ultra-fast Charge Exchange Recombination Spectroscopy

UF-CHERS is a high light throughput, high transmission spectrometer that measures ion temperature fluctuations and toroidal velocity fluctuations with a spatial resolution of $\Delta x \sim 1\,cm$ and a temporal resolution of $\Delta t = 1\,\mu s$. UF-CHERS observes the Doppler-broadened $n = 8 \rightarrow 7$ transition at $\lambda_0 = 529.05\,nm$ of hydrogenic carbons $C^{(5+)*}$ [76]. The ion temperature can be determined from the spectral broadening of the emission lines, while the toroidal velocity can be extracted from the Doppler shift of the emission lines. At present, two spatial UF-CHERS channels are installed in DIII-D, with each spatial channel consisting of eight spectral channels. The UF-CHERS channel arrangement used in the experiments analyzed in this thesis is shown in Fig. 3.4.
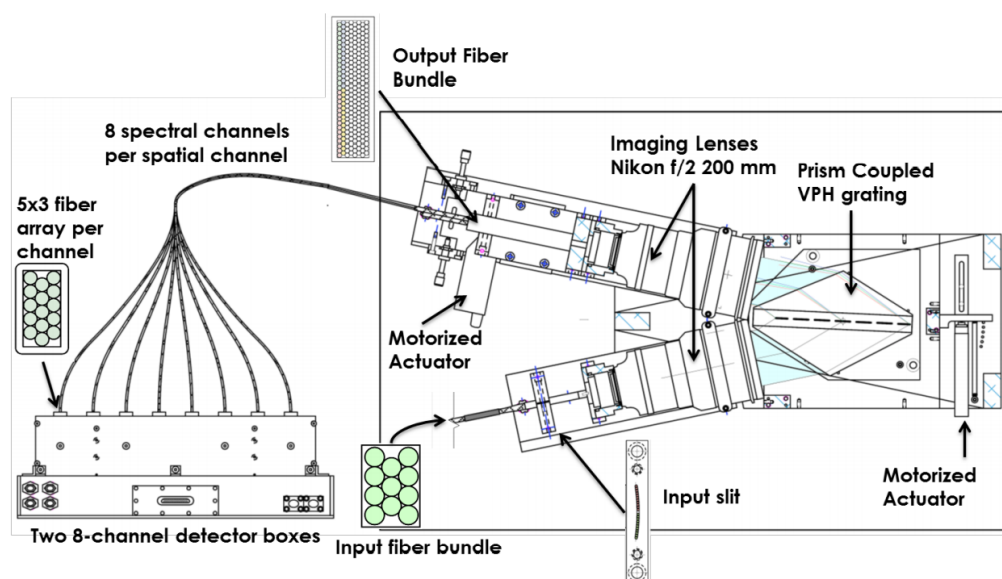
Figure 3.15: Diagram of the UF-CHERS major components [76]

A diagram of the major components in the UF-CHERS spectrometer is shown in Fig. 3.15. UF-CHERS shares the same front-end optics with BES

and uses two 4:3:4 fiber bundles (same as those used by BES) to guide the light to the spectroscopy lab. Each fiber bundle comprises eleven 1 mm diameter optical fibers [76]. In total, 22 fibers are stacked radially adjacent along the input slit, as illustrated in Fig. 3.15.

The collected light from the input fibers is then collimated using a 200-mm F/2 Nikkor lens onto a volume phase holographic (VPH) transmission grating laminated between two BK7 glass prisms. The combination of the grating and prisms is called a "grism", which has an angular dispersion of 72 nm/radian and a linear dispersion of 0.36 nm/mm [76].

The spectrally dispersed light is focused by a second 200-mm F/2 Nikkor lens onto a rectangular output fiber bundle consisting of 8 (columns) $\times$ 30 (rows) optical fibers with 800 μm in diameter. The eight columns of fibers in the output fiber bundle correspond to the eight spectral channels. The top 15 rows constitute one spatial channel, while the bottom 15 rows form the other spatial channel [76].

In summary, the UF-CHERS front-end optics collect light at two spatial locations. The two spatial chords are labeled as UF-CHERS01 and UF-CHERS02. the UF-CHERS spectrometer then diffracts light collected by each spatial chord into eight spectral channels that cover a wavelength range from 528.0 to 530.0 nm at approximately 0.25 nm spectral resolution per channel. The first spatial chord consists of spectral channels from TIF01 to TIF08, while the second spatial chord consists of spectral channels from TIF09 to TIF16.

As shown in Fig. 3.15, the output fiber bundle from the spectrometer is connected with two 8-channel detector boxes. Light received by each spectral channel is collimated and magnified by the optical system inside the detector module to be measured by an avalanche photodiode (APD) detector. The operating voltages of APD detectors are tested to maximize the gain while minimizing the excess noise factor, thereby optimizing the signal-to-noise ratio [79].

The current signals from the APD detectors are converted to voltage signals by the preamplifier circuits, which are then amplified by the supporting electronics to achieve a sufficient signal amplitude and digitized at a 1 MHz sampling rate using a D-TACQ ACQ132 digitizer, which has a finite impulse response (FIR) anti-aliasing filter [76].

The spatial localization of UF-CHERS channels is similar to BES channels since they share the same front-end optics and light collection technique. Figure 3.7 shows that the average poloidal width is 1.3 cm for UF-CHERS channels. In the radial direction, the UF-CHERS channel covers about 1.1 cm. The radial expansion of the UF-CHERS PSF is in general narrower compared to BES PSF because there is no beam smearing effect for UF-CHERS measured carbon emissions. The low-energy thermal carbon ions move much slower than the fast beam particles and have a fast transition time of ~ 1 ns.
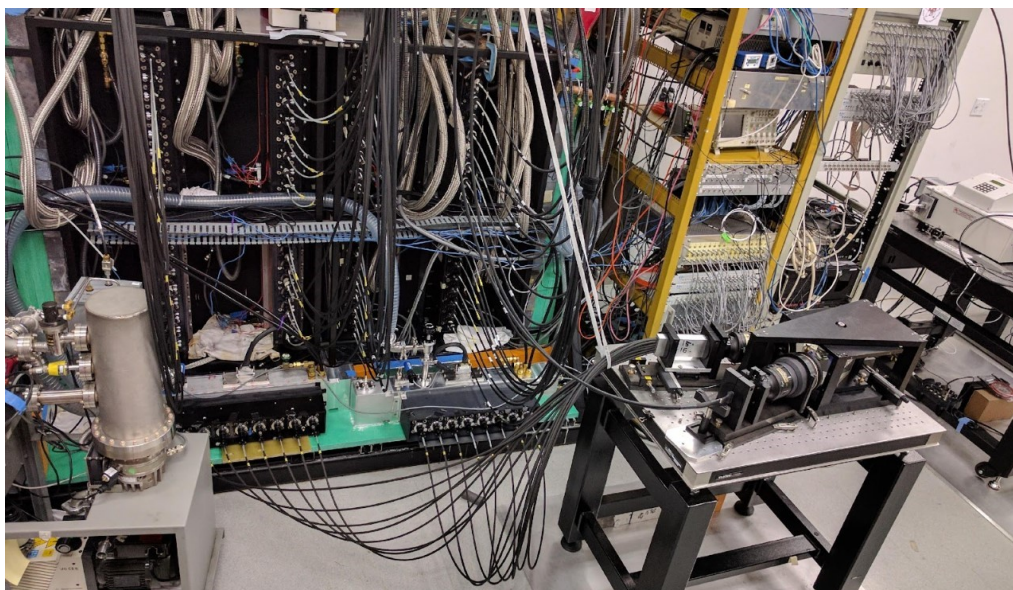
Figure 3.16: Photo of the UF-CHERS system installed on DIII-D. The spectrometer is placed on the optical table and connected to the two 8-channel detectors on the floor. It also shows the BES detectors in the background.

In 2021, the UF-CHERS detector boxes suffered a failed internal coolant line that flooded one detector box and vented the other detector box while the high voltage power supply was still applied to APDs. The detector boxes were then sent back to Madison. The cause of the failed coolant line was identified and addressed to prevent future failure. The damaged APDs were replaced and tested at different operating temperatures. The high voltage filter was also redesigned and achieved substantial improvement in noise reduction. After the repair, the UF-CHERS detector boxes are now maintained at 0°C using thermoelectric cooler (TEC) under atmospheric pressure, while the excess heat from TEC is dissipated by an external chiller. Figure 3.16 shows a photo of the UF-CHERS and BES systems currently deployed at DIII-D.

3.3.1   Calibrations and Data Pre-processing

To derive ion temperature and toroidal velocity fluctuations from the UF-CHERS raw data, two essential calibrations are required to precisely determine the wavelength and sensitivity of each spectral channel [76]. Wavelength calibration is performed using a UVP Pen-Ray Neon Lamp. The two neon emission lines, $\lambda_1 = 528.00853$ nm and $\lambda_2 = 529.81891$ nm, fall within the spectrometer's passband, which can be used as references to adjust or measure the range of wavelength observed by each spectral channel [76]. Determining the wavelength of spectral channels is crucial for deriving toroidal velocity since toroidal velocity is calculated based on the Doppler shift of the carbon emission line.

Sweeping the neon emission lines across the detector arrays also provides a measure of the instrument function (IF) of the spectrometer. The instrument function is the intensity distribution of the spectrometer output from a monochromatic input. The spectral line measured from UF-CHERS can be expressed as a convolution between the spectrometer's instrument function and the actual emission line [76]. Therefore, knowing the in-

strument function is essential for accurately fitting the emission line and deriving the ion temperature.

White field calibration is performed with a labsphere to measure the sensitivity of each spectral channel. Due to manufacturing variations, the gain and wavelength dependence will differ among APDs. Furthermore, small deficits and fractures in optical fibers can result in varying transmission rates [76]. To account for these factors, measurements are taken from all spectral channels using the same light intensity input. Figure 3.17 shows the normalized sensitivity of all spectral channels for box1 (left) and box2 (right), which is determined through white field calibration.
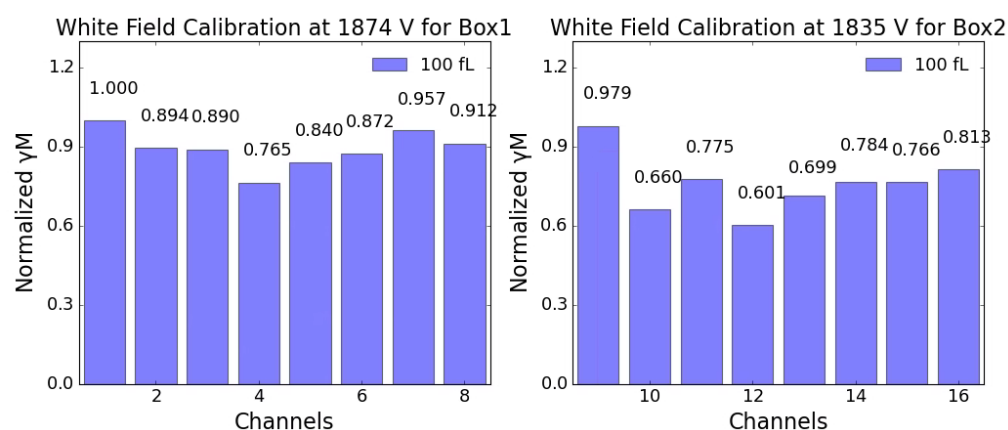
Figure 3.17: The normalized sensitivity of all spectral channels for box1 (left) and box2 (right), obtained from white field calibration

There are several data pre-processing procedures required before the UF-CHERS data can be used to fit into emission lines and perform spectral analysis. The first step is DC offset subtraction. UF-CHERS starts data acquisition 50 ms prior to the discharge to measure the voltage offset and detectors' dark noise. To obtain a uniform baseline, the raw data is subtracted from the average DC voltage recorded prior to the shot.

The second step is neutron spike removal. The UF-CHERS detectors are very sensitive and can become saturated due to neutrons, gamma rays,

and even natural background radiations hitting the APD. These spikes are much larger in magnitude than the true signal and can be removed by replacing the spikes with the average of their nearby data since they are typically only one or a few 1 μs time samples in width.

The third step is background subtraction. The measured signal is a combination of active charge exchange emissions from the NBI viewline and background emissions, including passive charge exchange emissions, electron impact excitations, and bremsstrahlung radiations. Therefore, NBI is modulated with short beam-off phases to obtain the background emissions. Assuming the background signal does not vary significantly between beam-off phases, a linear interpolation is performed to estimate the background signal level and subtract it from the data [76].

After completing these pre-processing steps, the UF-CHERS signals are normalized by dividing them by the respective detector sensitivities, which are determined from the white field calibrations. An example is provided in Fig. 3.18 to illustrate the raw and pre-processed UF-CHERS data, using channel TIF05 from DIII-D discharge 193082.
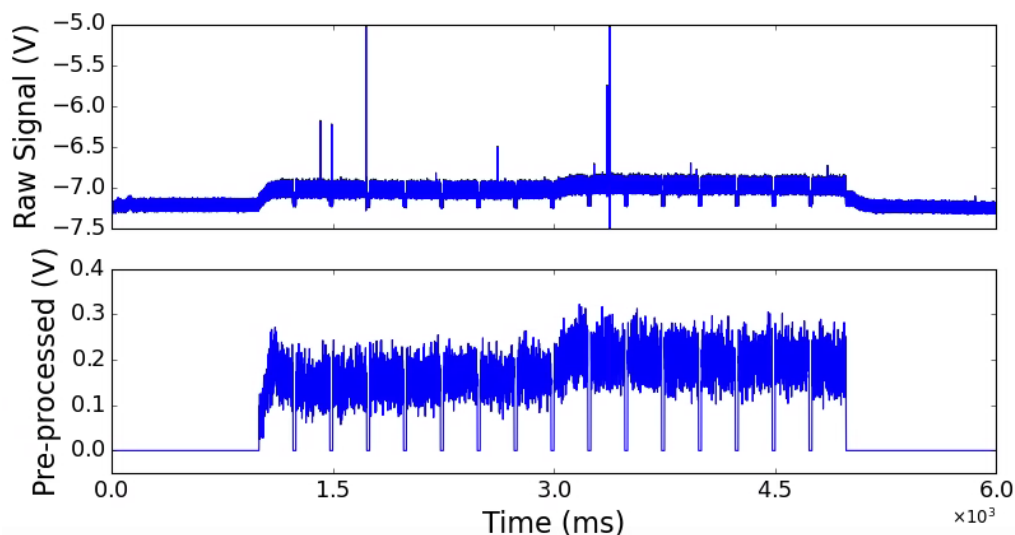
Figure 3.18: Comparison between raw and pre-processed UF-CHERS data

3.3.2 Noise Handling and Data Fitting

Gaussian fittings can be applied to the active charge exchange emission signals measured by UF-CHERS spectral channels to infer carbon density, temperature, and toroidal velocity fluctuations. To enhance the accuracy of Gaussian fitting, additional noise removal procedures are implemented beyond standard data pre-processing. Generally, three major noise sources exist in UF-CHERS data, dark (amplifier) noise, photon noise, and background carbon emissions. The power spectrum of the active turbulence signal and noise sources of spectral channel TIF13 for DIII-D discharge 193082 is shown in Fig. 3.19, where dark noise and photon noise are combined as incoherent noise.
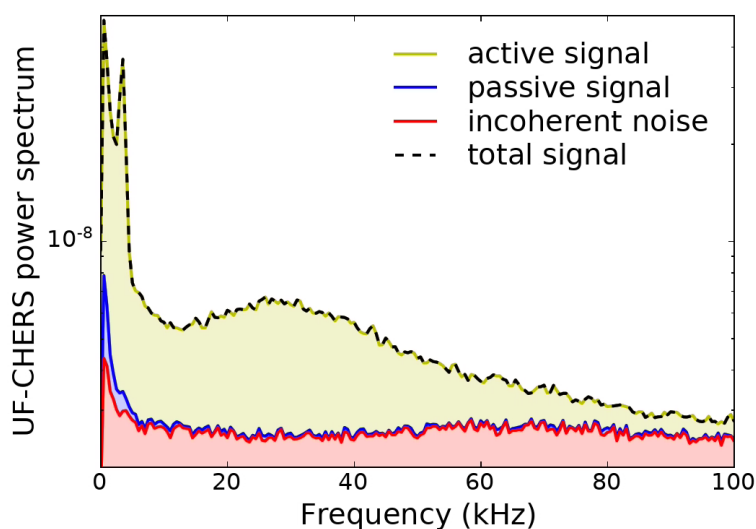
Figure 3.19: Power spectrum of active turbulence signal (yellow), background carbon emission (blue) and incoherence noise (red) of spectral channel TIF13 for DIII-D discharge 193082 at t $= 3.0 - 5.0$ s

While it is impossible to fully separate random dark noise and photon noise from the desired active charge exchange signals in the time domain, they can be partially separated in the frequency domain. Similar to the BES data, the frequency range of the turbulence signals measured by UF-

CHERS can be determined by performing cross-spectral analysis between spectral channels from the same spatial chord. Random noise outside this frequency range can be effectively eliminated by applying a band-pass frequency filter. Although this method does not entirely remove the contamination of dark noise and photon noise due to the overlapped frequency between turbulence signals and noise, it significantly enhances the signal-to-noise ratio and facilitates the Gaussian fitting.

The background carbon emissions in plasma arise from various sources, including passive charge exchange reactions and bremsstrahlung radiation. They are constantly present inside the plasma, both with and without the application of NBI. The equilibrium component of the background carbon emission is addressed during the data pre-processing when the background signal level is subtracted. The fluctuation component of the background emission cannot be directly separated from the turbulence signals in the time domain, but it is found to be localized at low frequency (< 10 kHz) and does not significantly overlap with the broad-band turbulence signal (typically between $10 - 200$ kHz), as shown in Fig. 3.19. The amplitude of the background carbon emissions is also significantly lower than the active turbulence signals, and therefore not a major concern of the data quality.

After applying the data pre-processing and noise removal procedures, the spectral data can be fitted by a modeling function Eqn. (3.10) to obtain the charge exchange recombination emission intensity, ion temperature, and toroidal velocity fluctuations for carbons [76]

$$S(\lambda) = P_3 + \frac{P_0}{\sqrt{2\pi(\sigma_{IF}^2 + P_2^2)}} \exp\left(-\frac{(P_1 - \lambda_0)^2}{2(\sigma_{IF}^2 + P_2^2)}\right) \qquad (3.10)$$

where $S(\lambda)$ is the fitting function of the modeled spectrum, P_0 is the signal intensity, P_1 is the spectral position that infers v_ϕ, P_2 is the spectral width that gives T_i, P_3 is a constant offset to account for residual background signal, and σ_{IF} is the instrument function.

An example of the Gaussian fits and derived quantities is shown in Fig. 3.20. These results are obtained at 1 µs time resolution for a representative DIII-D discharge 193082 analyzed in this thesis. The fitting curve demonstrates good accuracy, particularly for the central spectral channels, as indicated by the small residuals.
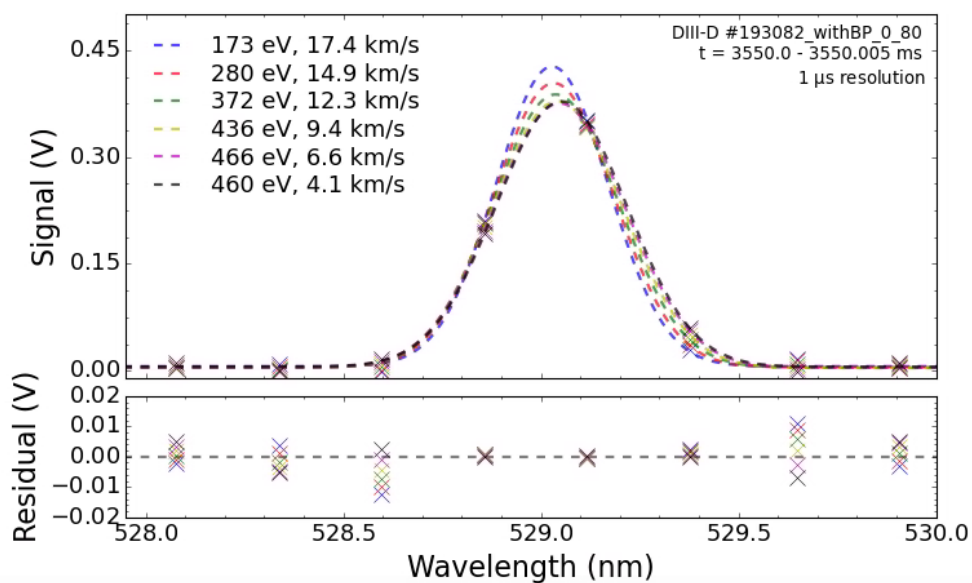
Figure 3.20: Example of Gaussian fits, residuals, and derived quantities from UF-CHERS01 of DIII-D discharge 193082

4 EXPERIMENTAL DETERMINATION OF REYNOLDS STRESS

Self-generated toroidal flow due to turbulent Reynolds stress is important in fusion plasmas since rotation improves confinement and stability. The primary goal of this thesis is to experimentally determine the turbulence-driven Reynolds stress and to examine its role in driving intrinsic rotation in tokamak plasmas. This objective is further elaborated, focusing on two central questions: how is Reynolds stress generated, and can it explain the measured rotation profile? To address these questions, a half-day of experimental time was awarded through a competitive PhD experimental solicitation; this highly specialized experiment allowed for the measurement of turbulence-driven density and velocity fluctuations in dedicated experiments using BES and UF-CHERS.

This chapter presents the experimental determination of Reynolds stress and is structured as follows. Section 4.1 provides an overview of the DIII-D experiments. Section 4.2 evaluates the data quality of the fluctuation measurements. Section 4.3 presents the turbulence characteristics and identifies the changes in the mixture of turbulence modes with varying heating methods. Finally, Section 4.4 determines the Reynolds stress via correlated radial and toroidal velocity fluctuation measurements.

4.1 Experiment Design and Plasma Profiles

Accurate determination of the Reynolds stress relies on high-quality fluctuation measurements from BES and UF-CHERS, which benefit from strong turbulence amplitude and high neutral beam energy. However, the high-energy 150° beam, required by both BES and UF-CHERS, introduces considerable heating power and toroidal torque into the plasma. This significant external torque poses a challenge for extracting residual stress from the measured Reynolds stress, which benefits from having

a near-zero flat rotation profile in the concerned regions, as can be seen from Eqn. (2.35); zeroing out the diffusive and convective terms makes identification of the residual stress term from the turbulent momentum transport much more direct and straightforward.

Fortunately, the rotation profile can be effectively controlled using the balanced beam capability at DIII-D. In a typical scenario with normal plasma current I_p, to counteract the co-current toroidal torque induced by the 150° beam τ_{150}, along with the expected co-current intrinsic torque $\tau_{intrinsic}$, it is necessary to adjust the rotatable 210° beam in the opposite direction and inject a counter-current torque τ_{210}. The relative beam powers must be fine-tuned such that $\tau_{150} + \tau_{intrinsic} = \tau_{210}$, to attain the desired near-zero flat rotation profile.

However, the large amount of heating power from the 150° and 210° beams can easily exceed the L-H transition power threshold. This transition significantly reduces turbulence amplitude, adversely affecting fluctuation measurements. Therefore, to stay under L-mode, the plasma current is reversed, aligning the co-current intrinsic torque in opposition to the 150° beam torque, with $\tau_{150} - \tau_{intrinsic} = \tau_{210}$. Balancing the 150° beam with the combination of the 210° beam and intrinsic torque minimizes the total heating power injected from the beams.

The magnetic field is also reversed to maintain the pitch angle such that the BES and UF-CHERS optical sightlines are well-aligned with the local magnetic pitch angle to ensure optimal spatial resolution perpendicular to the magnetic field. Furthermore, a lower-biased double null (LDN) divertor configuration is employed with the ion grad-B drift direction pointing away from the dominant X-point, which is an unfavorable magnetic configuration that significantly raises the L-H transition power threshold and helps to maintain the plasma in L-mode [80].

Figure 4.1 shows the beam program employed in this experiment. The left source of the 150° beam (150L) is operated at 65 keV as the diagnostics

beam for BES and UF-CHERS, which injects 1.1 *MW* of heating power into the plasma. The 150L is active for 230 ms in every 250 ms cycle for fluctuation measurements. The 20 ms beam-off intervals are used to measure the background signals for UF-CHERS data pre-processing. During these 20 ms beam-off periods, the 30L beam is activated for 10 ms, followed by another 10 ms blip of the 330L beam. These 10 ms beam blips enable CER measurements while maintaining a constant heating power and net co-current torque injection.

A torque scan with the opposite-directed 210R beam is performed at the beginning of the experiment to attain the desired rotation profile. Eventually, a 0.5 *MW* of 210R beam is applied to bring the rotation profile
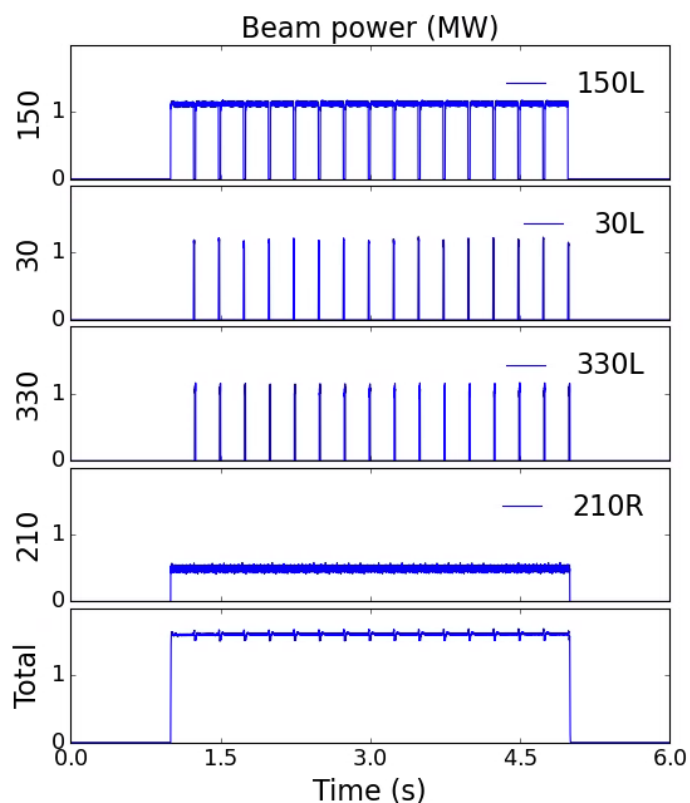
Figure 4.1: Time traces of neutral beams and their heating powers for a representative DIII-D discharge 193082

close to zero, resulting in a total of 1.6 MW of heating power and a net -0.75 ± 0.03 Nm volume integrated counter-current torque being injected into the plasma. The negative sign indicates that it is a counter-current torque, while the positive sign represents the co-current direction. This sign convention remains consistent throughout the thesis.

In addition to beam programs, another crucial aspect of the experiment design is the diagnostics setup. Figure 4.2 illustrates the BES (blue boxes) and UF-CHERS (red boxes) channel arrangements used in this experiment. The 64 BES channels are arranged in an approximately 8×8 configuration, enabling the measurement of 2D density fluctuation images and therefore the application of velocimetry analysis. The two UF-CHERS spatial channels are inserted in the center of the BES array, replacing one of the BES fiber bundles. This ensures that the BES and UF-CHERS measurements are in close proximity and within a radial and poloidal correlation length of the low-wavenumber turbulence being measured.
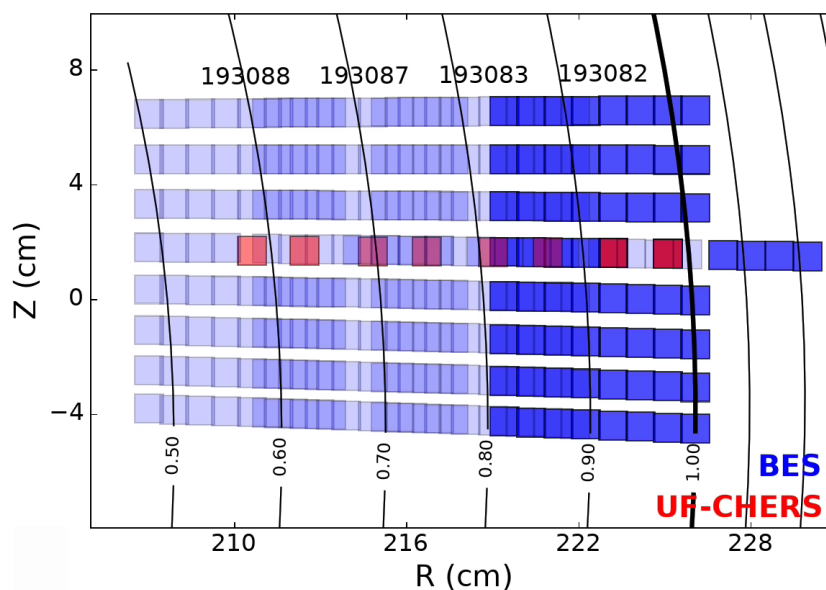
Figure 4.2: BES and UF-CHERS diagnostics channel arrangement for DIII-D discharge 193082 and its repeated shots

Due to the finite radial coverage of BES and UF-CHERS channels, a spatial scan is performed to measure the entire outer region of the plasma core from $\rho = 0.55 - 1.0$ to fully measure and characterize turbulence in the outer half of the radius where intrinsic rotation has been observed to originate. Their viewing locations inside the plasma are radially scanned by remotely controlling a motorized fiber-mounting array between shots. Figure 4.2 shows the radially varying locations of BES and UF-CHERS channels for a representative DIII-D discharge 193082 and its repeated shots during the spatial scan.

Finally, motivated by the observed correlation between intrinsic rotation and turbulence modes in previous experiments, a 0.55 MW of ECH is applied at the second half of the discharge to alter the ion and electron heat fluxes, and thereby the mixture of turbulence modes. The ECH deposition profile is off-axis at $\rho = 0.2 - 0.3$ to increase the electron temperature while maintaining a self-consistent profile shape. Figure 4.3 presents the time traces of major plasma parameters for the DIII-D discharge 193082 and its repeated shots. The repeat shots exhibit good consistency with discharge 193082, with all the important plasma parameters nearly overlapping.

As shown in Fig. 4.3, these discharges feature a reversed plasma current $I_p = -0.8$ MA and a reversed toroidal magnetic field $B_T = 2.0$ T. With the application of ECH, the line-averaged electron density increases from $\bar{n}_e = 2.3 \times 10^{19}$ m^{-3} to 2.8×10^{19} m^{-3}. The stored energy increases from 0.14 MJ to 0.21 MJ. The core electron temperature increases slightly from 2.0 keV to 2.2 keV. Finally, the edge toroidal rotation shifts from near-zero counter-current rotation to 8 km/s co-current rotation.

A long flattop time is maintained to ensure sufficient statistics for calculating ensemble averages of fluctuation measurements. It should be noted that the plasma is still evolving during the first half of the discharge, resulting in slightly different plasma conditions and turbulence features between $1.0 - 2.0$ s and $2.0 - 3.0$ s. To accentuate the contrasts and maintain
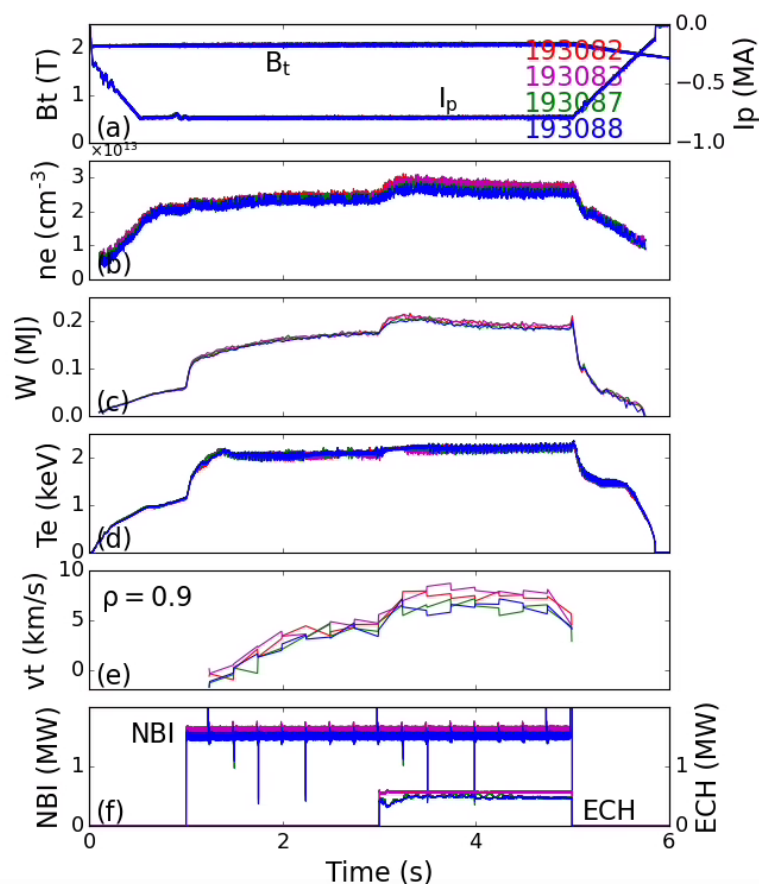
Figure 4.3: Time traces of (a) toroidal magnetic field and plasma current, (b) line-averaged plasma density, (c) stored energy, (d) core electron temperature, (e) edge toroidal rotation, and (f) NBI and ECH heating power for DIII-D discharge 193082 and its repeated shots, 193083, 193087, and 193088

clarity in the figures, we present results from two analysis time windows with distinct plasma conditions and turbulence characteristics: the first from $1.0-1.5$ s, corresponding to the NBI-only stage, and the second from $3.5-4.75$ s, indicative of the NBI+ECH stage (see Appendix B for the intermediate time case between $2.0-3.0$ s).

For simplicity, discharge 193082 is used as a representative discharge to conduct transport analysis using TRANSP. Figure 4.4 shows the plasma profiles, with the blue and red colors representing the NBI-only and

NBI+ECH stages, respectively. The total electron heating is shown in Fig. 4.4(d), with a significant peak at $\rho = 0.2 - 0.3$ due to ECH. As shown in Fig. 4.4(a)$-$(c), the application of ECH elevates the entire electron density and temperature profile in the plasma core and results in steeper gradients near the edge. The ion temperature also increases with the application of ECH, which can be attributed to the collisional coupling between ions and the heated electrons.
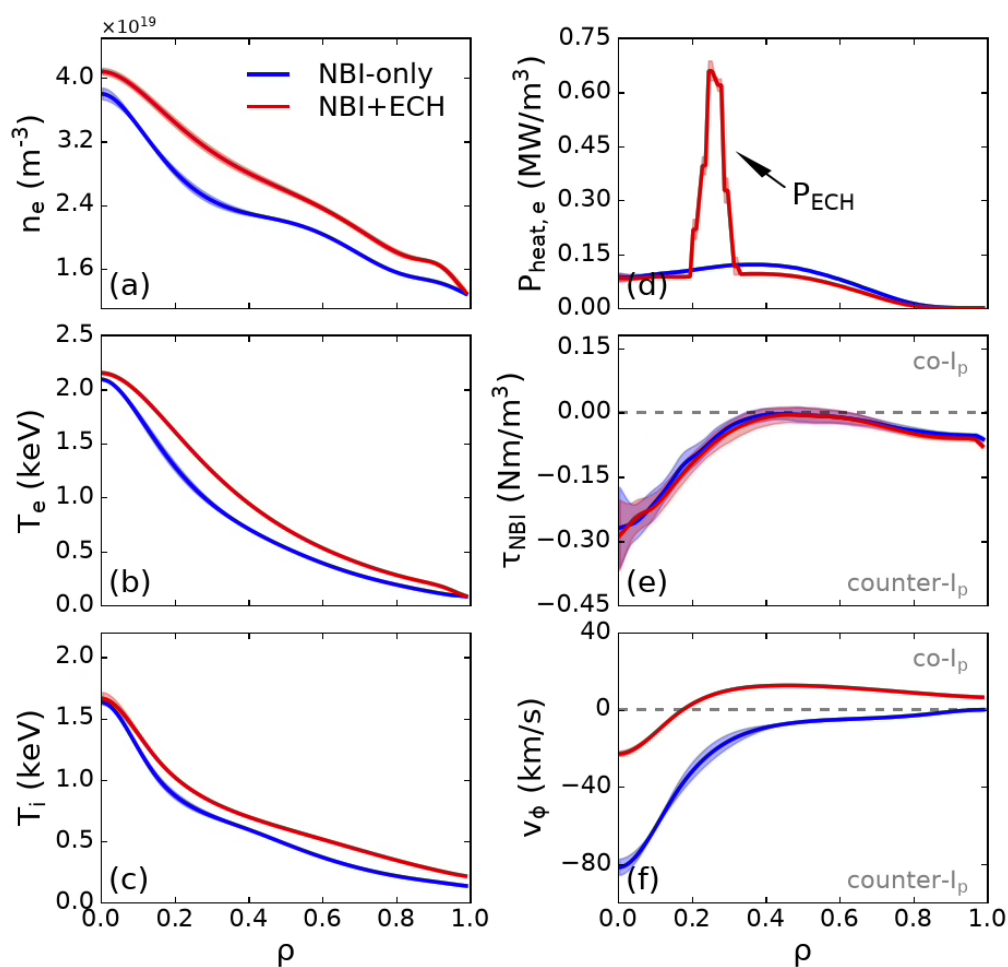
Figure 4.4: Radial profiles of the major plasma parameters, (a) electron density, (b) electron temperature, (c) ion temperature, (d) total electron heating, (e) NBI torque density, and (f) toroidal rotation, for DIII-D discharge 193082

Regarding the toroidal rotation, as shown in Fig. 4.4(e) and 4.4(f), the NBI torque deposition profile, calculated using the transport analysis code TRANSP, remains unchanged within uncertainties when ECH is added. However, despite the consistent external torque, the toroidal rotation drops significantly at the core, shifting from -80 km/s to -20 km/s. Meanwhile, the toroidal rotation in the bulk plasma, with $\rho = 0.2 - 1.0$, reverses direction from counter-current to co-current. Considering that the external torque from NBI is always in the counter-current direction, changes in the turbulence viscosity χ_ϕ can only modify the profile shape without changing the sign of the velocity gradient. The presence of a negative velocity gradient during the NBI+ECH stage strongly suggests the existence of a substantial non-diffusive flux due to the momentum pinch V_{pinch} or residual stress Π_ϕ^{res}.

4.2   Evaluation of Fluctuation Measurements

High-quality fluctuation measurements are essential for determining Reynolds stress. This section provides a thorough examination of the turbulence fluctuation measurements by BES and UF-CHERS. Section 4.2.1 evaluates the density fluctuations measured by BES, identifying important features of the turbulence signals, including their frequency distribution, wavenumber range, and signal-to-noise ratio. This evaluation demonstrates that the BES data quality is sufficient to perform cross-correlation and velocimetry analysis.

Section 4.2.2 discusses the carbon density, temperature and toroidal velocity fluctuations obtained from UF-CHERS, outlining the necessary data processing and fitting procedures. Cross-field spectral analysis is performed between BES and UF-CHERS measurements. These results demonstrate the reliability of the UF-CHERS data and provide valuable information for optimizing the velocimetry input parameters.

Finally, Section 4.2.3 investigates the radial and poloidal velocity fluctuations inferred using the velocimetry analysis. It optimizes two crucial input parameters, the smoothing width and the multi-frame factor, based on information obtained from the previous analysis. Cross-field spectral analysis between the velocimetry inferred velocity fluctuations and BES measured density fluctuations demonstrates the consistency and reliability of the velocimetry results.

4.2.1 Density Fluctuations Measured by BES

As an example, Figure 4.5 presents the cross-spectral analysis results of density fluctuations measured by poloidally adjacent BES channels, BES39 and BES31, at $\rho = 0.96$ during the NBI-only (blue) and NBI+ECH (red) stages. The cross-power spectrum in Fig.4.5(a) is used to assess the data quality and calculate the signal-to-noise ratio. A thorough analysis of the turbulence signal and noise sources for the NBI-only and NBI+ECH stages is shown in Fig.4.6(a) and Fig. 4.6(b), respectively.

In Fig.4.6, the total signal (black dashed) is calculated as the square root of the product of the auto-powers of BES39 and BES31 when NBI is on, $P_{total} = \sqrt{P_{39}P_{31}}$. The turbulence signal (yellow) is estimated from the cross-power between BES39 and BES31, $P_{turb} = P_{39,31}$. Amplifier noise (red) is calculated using the auto-powers of BES39 and BES31 dark measurements, $P_{amp} = \sqrt{P_{39,dark}P_{31,dark}}$. Beam noise (blue) is calculated using cross-powers between BES39, BES31, and a channel that is both radially and poloidally distant, BES01, $P_{beam} = P_{39,01}P_{31,01}/P_{01}$. The total incoherence noise is defined as the suppressed portion of the signal during cross-spectral analysis, $P_{incoherent} = P_{total} - P_{turb}$. Photon noise (magenta) is estimated by subtracting the amplifier noise from the total incoherent noise, $P_{photon} = P_{incoherent} - P_{amp}$.

The discrepancy between the total signal and the summation of all signal and noise sources might be attributed to the underestimated tur-
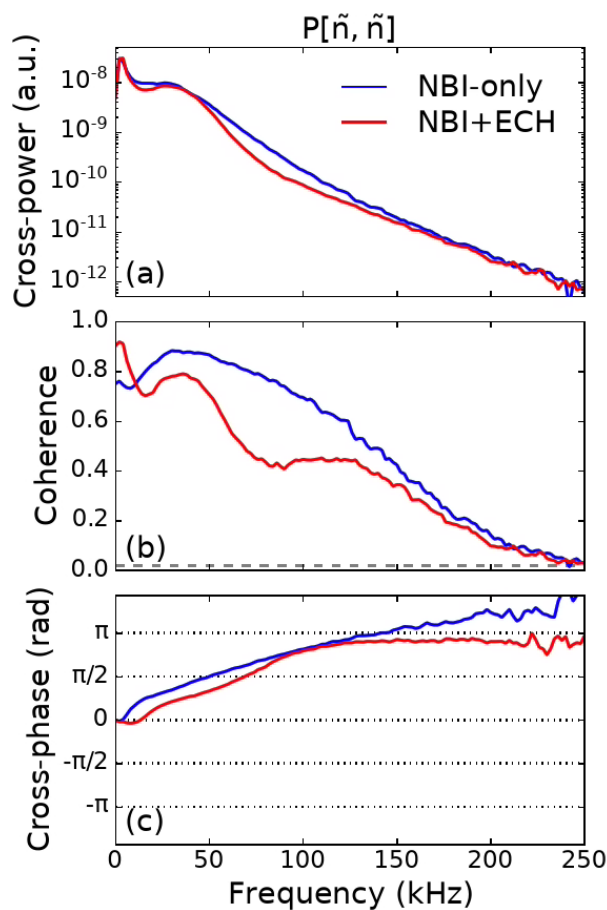
Figure 4.5: Cross-spectral analysis results, including (a) cross-power, (b) coherence, and (c) cross-phase, of density fluctuations between poloidally separated channels BES39 and BES31 for DIII-D discharge 193082

bulence signal due to the finite turbulence poloidal correlation length. Notably, while noise sources may appear significant in the logarithmic representation, they are actually two orders of magnitude smaller than the turbulence signals.

The coherence spectrum in Fig.4.5(b) reveals that the turbulence at $\rho = 0.96$ exhibits a frequency range of $5 - 250$ kHz. A band-pass frequency filter within this range is applied to the BES data before conducting cross-correlation and velocimetry analysis, which effectively suppresses noise
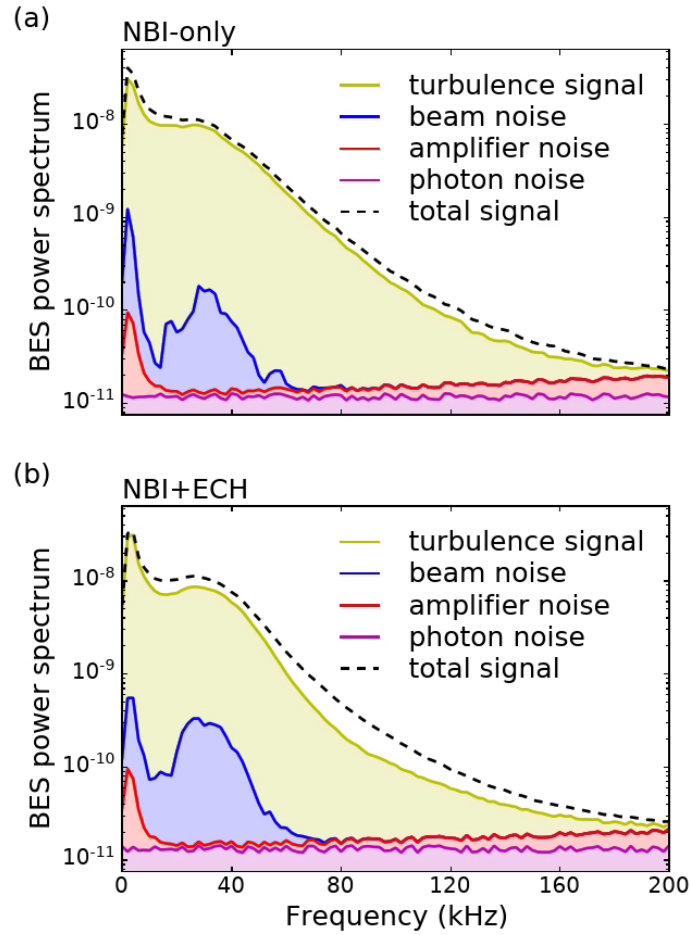
Figure 4.6: Power spectrum of the total signal (dashed), turbulence signal (yellow), and various noise sources including beam noise (blue), amplifier noise (red) and photon noise (magenta), in BES data for DIII-D discharge 193082 during the NBI-only and NBI+ECH stages

and enhances the accuracy of the analysis results. With that, the signal-to-noise ratio (SNR) is calculated as $\mathrm{SNR} = 10 \cdot \log_{10}\left(\frac{P_s}{P_n}\right)$, where P_s represents the turbulence signal and is obtained by integrating the turbulence power spectrum over the previously identified frequency range. P_n represents the total noise and is calculated by summing the frequency-integrated power from all noise sources.

Results show that the frequency-filtered density fluctuations at $\rho = 0.96$ have SNR of 17.4 and 15.7 during the NBI-only and NBI+ECH stages, respectively. Similar analyses are performed on BES channels at other radial locations, showing a typical SNR range of $10 - 17$ between $\rho = 0.9 - 1.0$, which is well above the SNR requirement of the velocimetry analysis ($\text{SNR} \geqslant 10$). The signal-to-noise ratio reduces to $3 - 5$ inside $\rho = 0.9$ as the turbulence intensity drops toward the plasma core, potentially leading to an underestimation of the velocity field amplitude at these locations in velocimetry analysis.

Another restriction when applying velocimetry is the wavenumber limitation ($k \leqslant 2~\text{cm}^{-1}$). The poloidal turbulence wavenumber k_θ is calculated from the cross-phase spectrum in Fig.4.5(c) using the formula $k_\theta = \phi/\Delta z$, where ϕ denotes the cross-phase between two poloidally adjacent channels and $\Delta z = 1.2~\text{cm}$ is the channel separation. As shown in Fig.4.5, the majority of turbulence signal (98% of its power) exhibits cross-phases within the range of 0 to 0.8π, resulting in a poloidal wavenumber range of $k_\theta < 2.0~\text{cm}^{-1}$.

The same procedure can be applied to derive the radial turbulence wavenumber, yielding $k_r < 0.33~\text{cm}^{-1}$. Both the poloidal and radial wavenumbers fall within the required range for velocimetry analysis, enabling a reasonably accurate determination of the 2D flow field. However, the amplitude of poloidal velocity fluctuations at higher frequencies might be underestimated due to their small spatial structure.

4.2.2 Toroidal Velocity Fluctuations From UF-CHERS

Evaluating the UF-CHERS data quality and the derived toroidal velocity fluctuations is essential for accurately determining the toroidal Reynolds stress. As shown in Fig. 4.7, the cross-power spectrum between UF-CHERS central spectral channels TIF13 (529.10 nm) and TIF12 (528.85 nm) indicates that the turbulence signal at $\rho = 0.96$ has a frequency range of

$0 - 80$ kHz during the NBI-only and NBI+ECH stages. A corresponding low-pass filter within this frequency range is applied to the UF-CHERS raw data before fitting it into a Gaussian curve. This suppresses the higher frequency random noise while maintaining the majority of the turbulence signals. Furthermore, since toroidal Reynolds stress involves correlating toroidal and radial velocity fluctuations, the identified frequency range for toroidal fluctuations sets the lower limit of spectral resolution for radial velocity fluctuations inferred from velocimetry analysis.
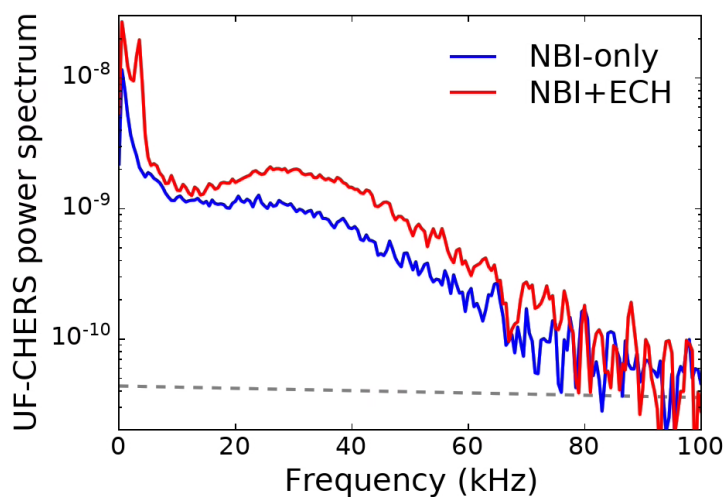
Figure 4.7: Cross-power spectrum between UF-CHERS spectral channels TIF13 and TIF12 (from the second spatial chord at $\rho = 0.96$) for DIII-D discharge 193082 during the NBI-only and NBI+ECH stages

Figure 4.8 compares the UF-CHERS fitting results obtained without a filter and with the $0 - 80$ kHz low-pass filter. The fitted data are collected at $\rho = 0.96$ in DIII-D discharge 193082, from 3550.0 to 3550.005 ms, during the NBI+ECH stage. The residuals are shown at the bottom of the fitting curves, and the derived quantities are included in the legend. The results show that applying the low-pass filter effectively suppresses random noise in the raw data, reduces the fitting residuals, and enhances the accuracy of the derived quantities.
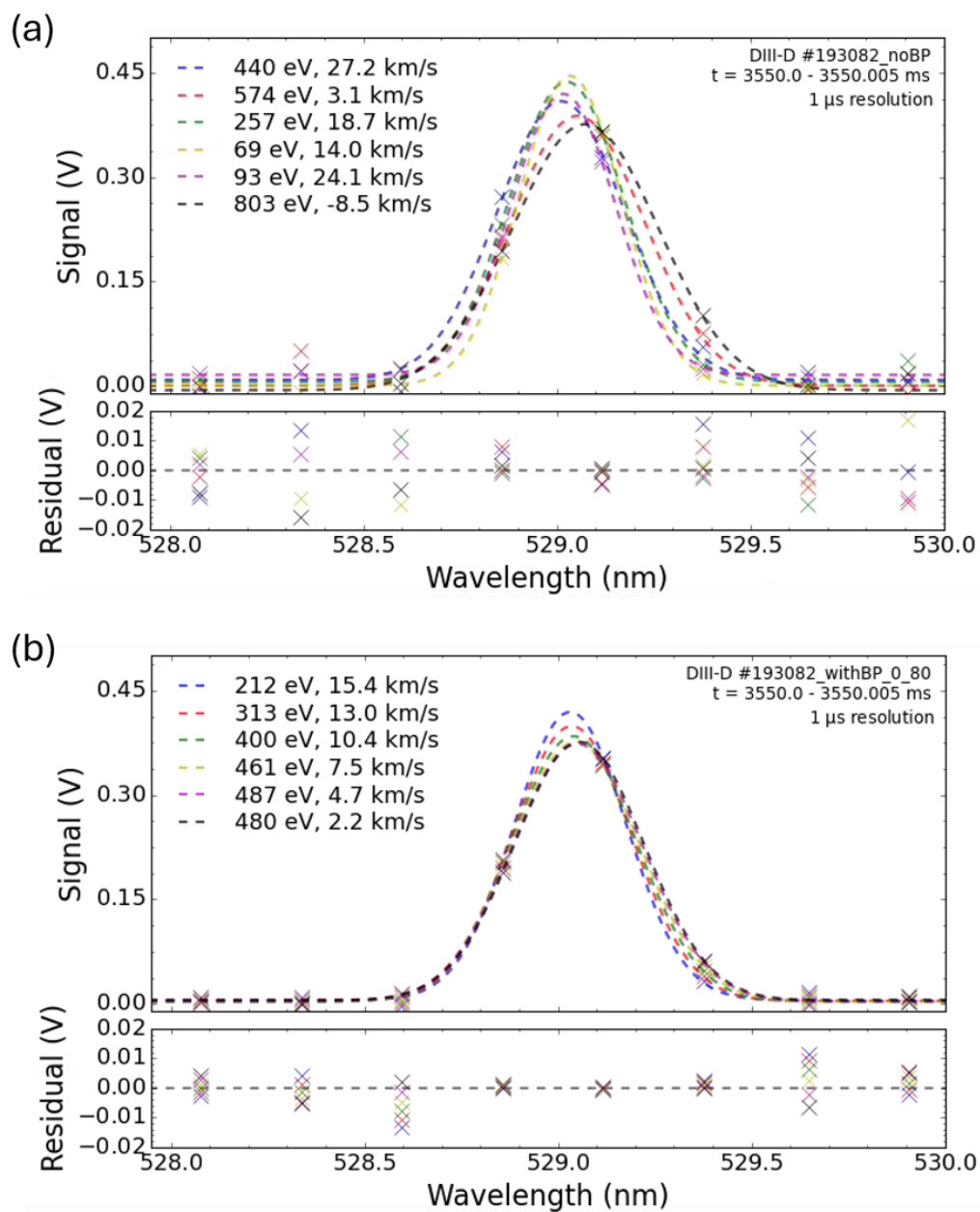
Figure 4.8: Comparison between the 1 μs UF-CHERS fitting results (a) with no filter and (b) with a 0 − 80 kHz low-pass filter. Data is collected from DIII-D discharge 193082 during the NBI+ECH stages at ρ = 0.96

The reliability of the UF-CHERS derived fluctuation quantities is evaluated by performing cross-spectral analysis with the BES data. Figure 4.9 shows the cross-spectral analysis results between density fluctuations measured by BES and carbon density, temperature, and toroidal velocity fluctuations measured by UF-CHERS, at $\rho = 0.96$, during both the NBI-only and NBI+ECH stages. The BES channel and the UF-CHERS channel are viewing the same radial-poloidal plane and are poloidally separated by 1.2 cm. A time shift of 15 µs is applied to the UF-CHERS measurement in this analysis to correct for the time lag introduced by the diagnostic hardware (20 µs) and the finite turbulence propagation velocity (-5 µs), details of which are introduced in a later section.
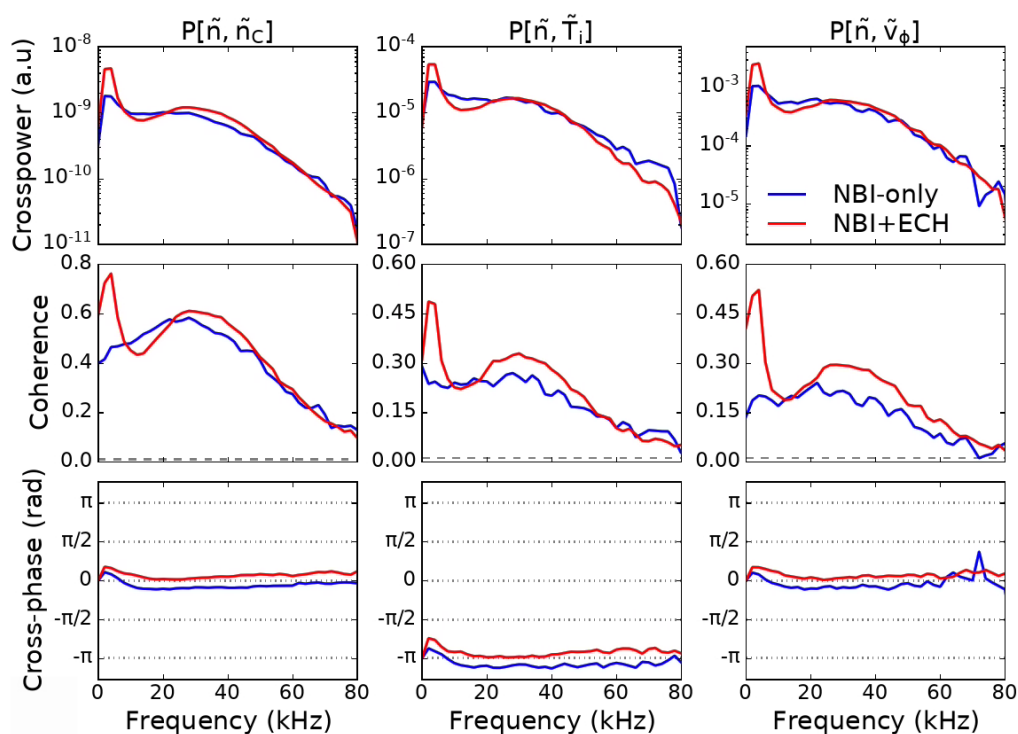
Figure 4.9: Cross-spectral analysis results showing the relationship between density fluctuations measured by BES and carbon density, temperature, and toroidal velocity fluctuations measured by UF-CHERS from DIII-D discharge 193082, at $\rho = 0.96$, during both the NBI-only and NBI+ECH stages

The cross-spectral analysis results between main ion and carbon density fluctuations, as shown in Fig. 4.9, reveal a prominent peak in the cross-power spectrum, a near-zero flat cross-phase, and maximum coherence values of 0.6 and 0.8 during the NBI-only and NBI+ECH stages, respectively. These results indicate that the same local turbulence is measured by both BES and UF-CHERS, suggesting that the main ion and carbon density fluctuations induced by this turbulence are highly correlated and in phase with each other. High coherence values are also observed for carbon temperature and toroidal velocity fluctuations correlated with the BES measurements, demonstrating the good reliability of the UF-CHERS derived fluctuation quantities.

4.2.3 Radial Velocity Fluctuations Inferred by Velocimetry

The previous section has already demonstrated that the data quality of the BES measured turbulence density fluctuations is sufficient for velocimetry analysis. Furthermore, the identified frequency range of $0 - 80$ kHz for toroidal velocity fluctuations establishes the lower limit of the spectral resolution for radial velocity fluctuations inferred from the velocimetry analysis. This information is essential for optimizing velocimetry input parameters, namely the smoothing width and the multi-frame factor, since increasing these parameters reduces the spectral resolution of the result.

This section presents the optimization of the velocimetry input parameters. The smoothing width is defined as the number of points used in a boxcar smoothing function during each iteration. In this analysis, the 8 (radial) $\times$ 8 (poloidal) turbulence image measured by BES is spatially interpolated to a spatial resolution of 40×40. Therefore, a smoothing width of 5 is equivalent to one channel width.

Figure 4.10 shows the auto-power (solid) and cross-power (dashed) spectra of radial velocity fluctuations inferred by the velocimetry analysis, at $\rho = 0.96$ during the NBI+ECH stage of DIII-D discharge 193082. Three

smoothing width values are tested $s = 5, 7$, and 15, corresponding to 1.0, 1.5, and 3.0 channel widths, respectively. The total signal, represented by the auto-power spectrum, is calculated as $P_{total} = \sqrt{P_{39}P_{31}}$, using poloidally separated channels BES39 and BES31. The turbulence signal, estimated by the cross-power spectrum, is calculated as $P_{turb} = P_{39,31}$.
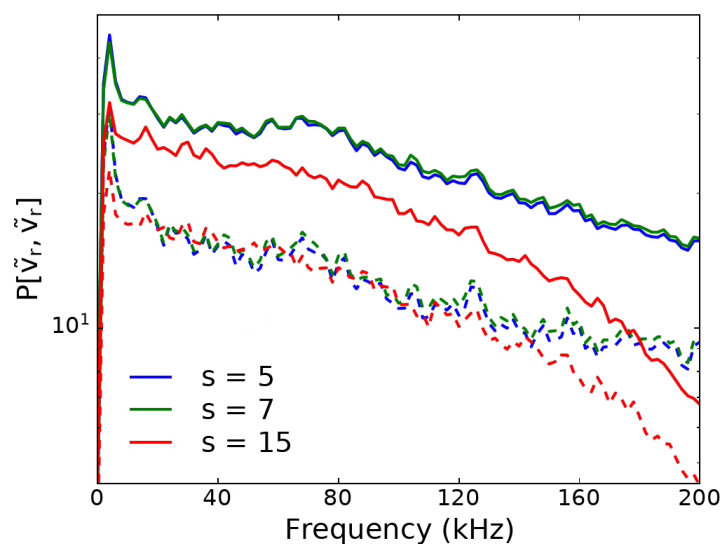
Figure 4.10: Auto-power (solid) and cross-power (dashed) spectra of radial velocity fluctuations inferred by the velocimetry analysis with smoothing widths of $s = 5, 7$, and 15, between poloidally separated channels BES39 and BES31, at $\rho = 0.96$ during $3250 - 3480$ ms in DIII-D discharge 193082

The auto-power and cross-power of the radial velocity fluctuations in Fig. 4.10 demonstrate a high degree of consistency for smoothing factors of $s = 5$ and $s = 7$, suggesting that increasing the smoothing width from 5 to 7 does not significantly alter the velocimetry results. However, a further increase in the smoothing width from 7 to 15 introduces noticeable changes. While it effectively suppresses random noise, it concurrently reduces the detectable turbulence signal from small spatial structures. This results in a decreased turbulence signal at $2 - 5$ kHz (a radially narrow zonal flow structure) and at higher frequencies $f > 120$ kHz (small-scale

turbulence eddies). Since this smoothing width is comparable to the observed turbulence correlation lengths, it also introduces unrealistic high coherence to distant channels, degrading the spatial resolution of the inferred 2D velocity field. Therefore, a smoothing factor of 7 is selected to suppress spurious vector displacements while preserving the essential spatial and spectral resolutions.

With the determined smoothing width, the velocimetry analysis is conducted with various multi-frame factors, $f = 2, 4, 6$, and 8. Since the UF-CHERS detector records data at a sampling rate of 1 MHz, a multi-frame factor of 2 corresponds to a time resolution of 1 µs and a spectral resolution up to 500 kHz. The multi-frame factors of 4, 6, and 8 correspond to spectral resolutions up to 250 kHz, 167 kHz, and 125 kHz, respectively. Figure 4.11 shows the auto-power (solid) and cross-power (dashed) spectra of the velocimetry inferred radial velocity fluctuations with various multi-frame factors. The same channel pair and analysis time window are used.
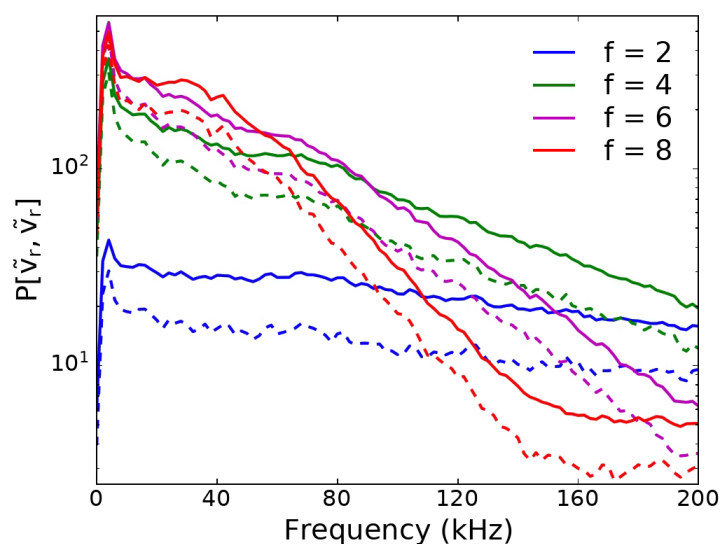
Figure 4.11: Auto-power (solid) and cross-power (dashed) spectra of radial velocity fluctuations inferred by the velocimetry analysis with multi-frame factors of $f = 2, 4, 6$, and 8, between poloidally separated channels BES39 and BES31, at $\rho = 0.96$ during $3250 - 3480$ ms in DIII-D discharge 193082

Results show that higher multi-frame factors further suppress the random noise while reducing the detectable turbulence fluctuations at higher frequencies. In Fig. 4.11, the cross-power of radial velocity fluctuations with $f = 2$ exceeds that with $f = 4$ at 200 kHz, indicating that increasing the multi-frame factor from 2 to 4 improves the detection of the turbulence-driven radial velocity fluctuations and enhances the accuracy of velocimetry results below 200 kHz. However, it also reduces the spectral resolution and averages out turbulence fluctuations above 200 kHz.

Similarly, increasing the multi-frame factor from 4 to 6 further enhances the accuracy of velocimetry results below 100 kHz and reduces the turbulence signal above 100 kHz. As the SNR becomes sufficiently high, this effect gradually saturates and the result shows a clear convergence for turbulence signals below 25 kHz when the multi-frame factor increases from 6 to 8. As discussed in the previous section, the UF-CHERS measured toroidal velocity fluctuation has a frequency range of $0 - 80$ kHz, which sets the lower limit of the spectral resolution for optimizing the velocimetry input parameters. Therefore, a multi-frame factor of 8 is selected to optimize the accuracy of the velocimetry results below 80 kHz.

With the optimized smoothing width and multi-frame factor, velocimetry analysis is performed on DIII-D discharge 193082 and its repeated shots. The reliability of the velocimetry results is evaluated by performing cross-spectral analysis with BES data. Figure 4.12 shows the cross-spectral analysis results between density fluctuations measured by BES and radial and poloidal velocity fluctuations inferred by velocimetry analysis, at $\rho = 0.96$, during the NBI-only and NBI+ECH stages. By correlating with the density fluctuations, we observe prominent cross-power, moderate coherence, and clear cross-phase for the radial and poloidal velocity fluctuations during both the NBI-only and NBI+ECH stages. This demonstrates the good reliability of the velocimetry results.
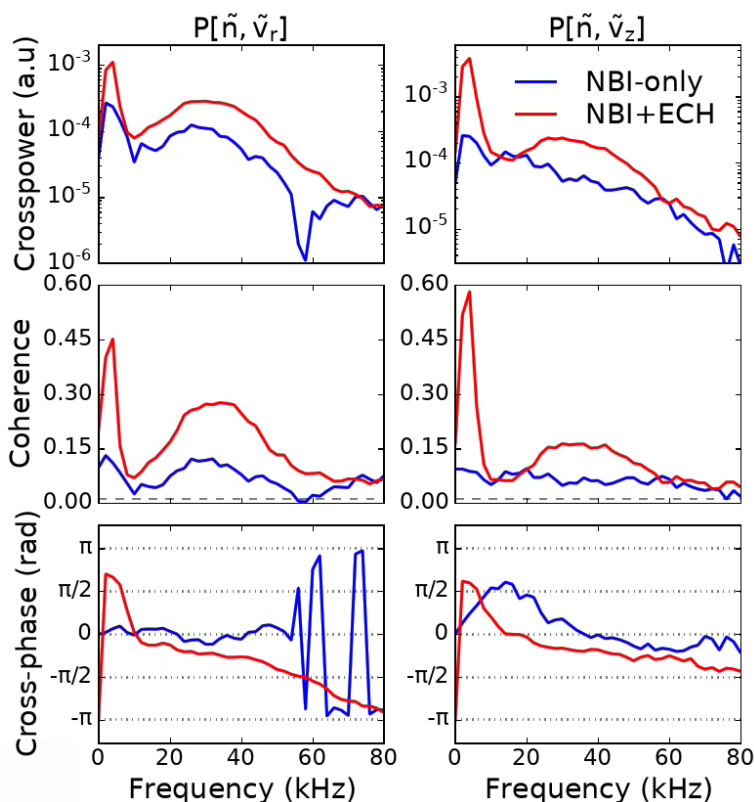
Figure 4.12: Cross-spectral analysis results showing the relationship between density fluctuations measured by BES and radial and poloidal velocity fluctuations inferred by velocimetry analysis from DIII-D discharge 193082, at $\rho = 0.96$, during both the NBI-only and NBI+ECH stages

4.3 Turbulence Characterization

This section identifies the likely dominant turbulence mode and provides a thorough examination of the turbulence characteristics during the NBI-only and NBI+ECH stages. Figure 4.13 shows the cross-spectral analysis results of density fluctuations measured by poloidally adjacent BES channels at three radial locations, $\rho = 0.80, 0.87$, and 0.96. The cross-power and coherence spectra reveal a progressively increasing turbulence amplitude and a broader frequency distribution toward the plasma edge.
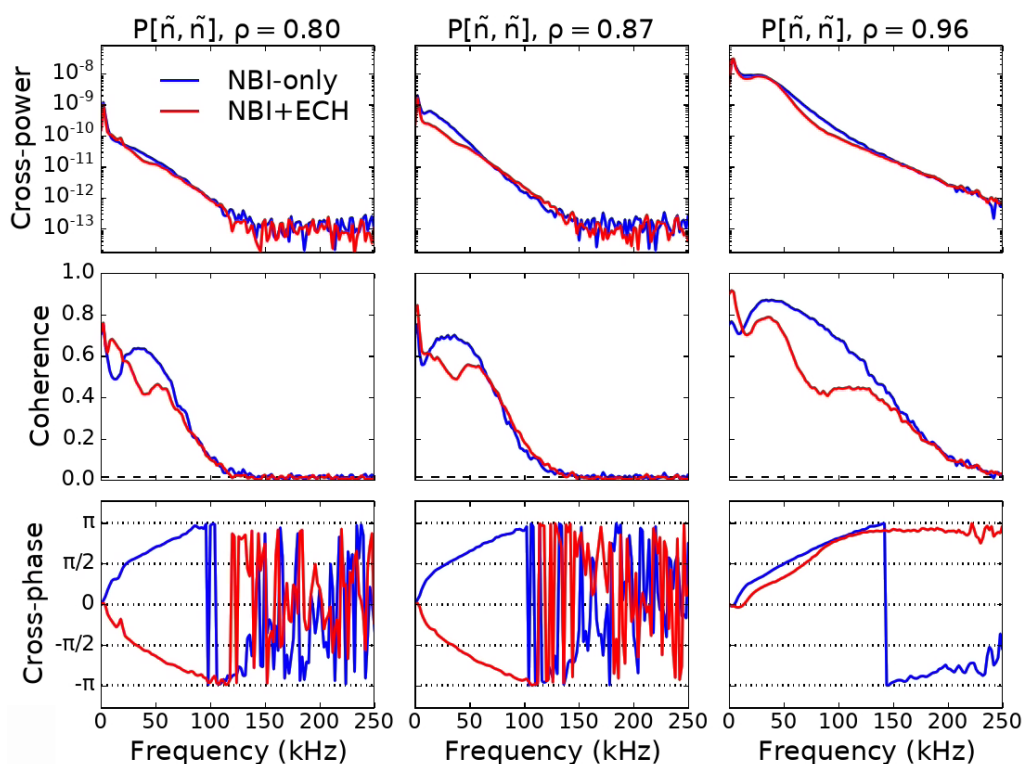
Figure 4.13: Cross-spectral analysis of density fluctuations in BES channel pairs 33/41, 36/44, and 39/31 for DIII-D discharge 193082

The slope of the cross-phase indicates the direction of turbulence propagation. A positive cross-phase slope indicates that the reference channel (top channel) leads in phase. Consequently, turbulence propagates from the reference channel to the target channel with a downward velocity in the lab frame. On the other hand, a negative cross-phase slope indicates that the target channel (bottom channel) leads in phase, and turbulence propagates upward in the lab frame. In this experiment, a reversed magnetic field (counter-clockwise from the top view) is employed, resulting in a downward electron diamagnetic velocity, $\mathbf{v}_e = \nabla P_e \times \mathbf{B}/en_e B^2$, and an upward ion diamagnetic velocity, $\mathbf{v}_i = -\nabla P_i \times \mathbf{B}/en_i B^2$, at the outboard mid-plane where the BES and UF-CHERS diagnostics are located.

As shown in Fig. 4.13, during the NBI-only stage, turbulence propagates predominantly in the electron diamagnetic direction across all radial locations. However, after ECH is applied, at the plasma edge of $\rho = 0.96$, the lower-frequency electron mode at 10 to 150 kHz is suppressed, and a higher-frequency ion mode at 100 to 250 kHz emerges, which is characterized by a second peak in coherence and a flattening of the cross-phase. This flat cross-phase results from the coexistence and overlap of lower-frequency electron-directed modes with a positive slope and higher-frequency ion-directed modes with a negative slope, leading to the superposition of their cross-phases. Inside $\rho < 0.9$, turbulence completely reverses its direction and propagates predominately in the ion diamagnetic direction during the NBI+ECH stage.

The turbulence mode can be more precisely identified by examining the turbulence mode velocity (turbulence advection velocity in the plasma frame). Cross-correlation analysis is performed on BES channels along the poloidal direction to quantify the turbulence propagation velocities. This propagation velocity is the sum of the turbulence mode velocity and the background $E \times B$ velocity of the bulk plasma that the turbulence is riding on. Therefore, the turbulence mode velocity can be derived by subtracting the $E \times B$ velocity from the measured turbulence propagation velocity.

In general, the turbulence propagation velocity refers to the turbulence group velocity. Figure 4.14(a) shows the turbulence group velocity (solid) and phase velocity (dashed) determined using the cross-correlation analysis. The phase velocity is calculated by dividing the channel separation by the time delay derived from the correlation function. In contrast, the group velocity is determined using the time delay derived from the envelope of the correlation function. The turbulence phase velocity refers to the velocity at which individual turbulence eddies propagate through the plasma, whereas the turbulence group velocity describes the collective speed of all turbulence eddies as a packet.
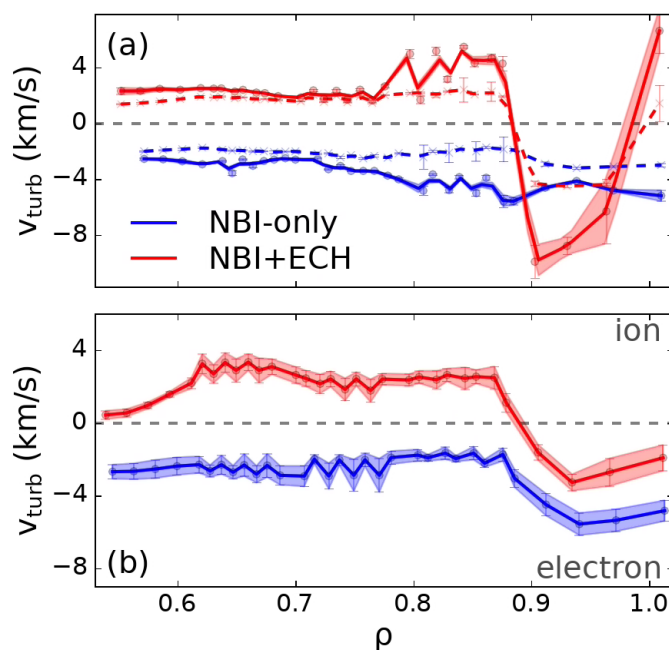
Figure 4.14: (a) Cross-correlation calculated turbulence group velocity (solid) and phase velocity (dashed), (b) velocimetry calculated propagation velocity

As shown in Fig. 4.14(a), the turbulence propagation (group) velocity, calculated through cross-correlation analysis, ranges from approximately -2 to -5 km/s in the electron direction during the NBI-only stage. After ECH is applied, the turbulence propagation velocity in the region $\rho = 0.6 - 0.9$ reverses, reaching $2 - 5$ km/s in the ion direction. These findings align with the cross-spectral analysis results, suggesting a shift in the mixture of turbulence modes with the application of ECH.

Calculating the turbulence propagation velocity using cross-correlation derived time delay is usually accurate when a single turbulence mode is present. However, in cases where multiple turbulence modes coexist, their time delays can overlap, resulting in a weighted average of their respective time delays obtained from the envelope of the correlation function. This effect is similar to the overlapping and superimposed cross-phase in the cross-spectral analysis, as previously described.

The superposition of time delays may introduce inaccuracies in the calculated turbulence propagation velocities, especially when the propagation velocities of different modes are opposed to each other (e.g. ITGs and TEMs). The averaged time delays often result in an overestimation of the turbulence propagation velocity. Meanwhile, discrepancies may arise between the turbulence group velocity and phase velocity since $v_{group} = v_{phase} + k\frac{\partial v_{group}}{\partial k}$ and $\partial v_{group}/\partial k \neq 0$.

As shown in Fig. 4.14(a), significant discrepancies appear at the plasma outer regions during both the NBI-only and NBI-ECH stages due to the coexistence of opposite-direction turbulence modes. The turbulence propagation velocities in this region are overestimated. The velocity jump from 5 km/s to -10 km/s during the NBI+ECH stage at $\rho = 0.85$ is likely a direct result of the averaged time delay between two oppositely directed turbulence modes with comparable contributions.

On the other hand, velocimetry analysis directly tracks turbulence eddies, resolves the net movement of particles, and therefore is able to correctly infer the turbulence propagation velocity in the presence of multiple modes. Figure 4.14(b) presents the time-averaged turbulence propagation velocities derived from the velocimetry analysis. The results exhibits good agreement with the cross-correlation analysis results in the region $\rho = 0.65 - 0.8$, where only one dominant turbulence mode exists. This analysis also provides more accurate results in the region $\rho = 0.8 - 1.0$, where a mixture of opposite-directed turbulence modes is present.

To extract turbulence mode velocity from the propagation velocity, the background $E \times B$ velocity is calculated. The radial electric field is derived from the radial force balance equation, as given in Eqn. (2.6). Measurements of carbon density, toroidal rotation, and poloidal rotation profiles are obtained using tangential and vertical CER. The contributions of these three terms are shown in Fig. 4.15(a)$-$(c). The radial electric field and the derived $E \times B$ velocity are shown in Fig. 4.15(d) and 4.15(e).

Finally, the turbulence mode velocity is determined by subtracting the background $E \times B$ velocity from the turbulence propagation velocity inferred through velocimetry analysis. As shown in Fig. 4.15(f), after ECH is applied, the turbulence mode velocity shifts from the electron diamagnetic direction to the ion diamagnetic direction.
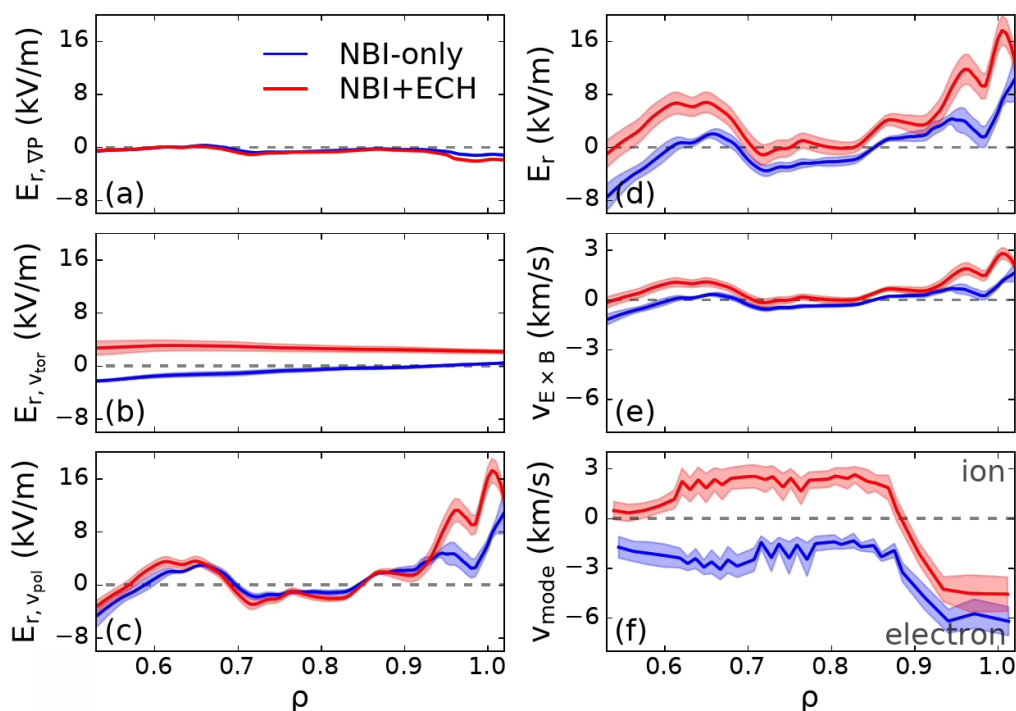
Figure 4.15: Results of (a) the pressure gradient term in E_r, (b) toroidal rotation term in E_r, (c) poloidal rotation term in E_r, (d) radial electric field, (e) $E \times B$ velocity, and (f) turbulence mode velocity, for NBI-only and NBI+ECH stages

By combining the cross-spectral results from Fig. 4.13, we conclude that, following the application of ECH, the lower frequency electron mode is suppressed. A higher frequency ion mode emerges and becomes predominant at $\rho = 0.63 - 0.86$. In the outer region, with $\rho = 0.86 - 1.0$, the turbulence instabilities shift from being predominantly electron modes to a mixture of electron and ion modes.

Other important turbulence characteristics are summarized in Fig. 4.16. The turbulence density fluctuation amplitudes shown in Fig. 4.16(a) are observed to be consistent for both stages and peak towards the plasma edge. The radial correlation length shown in Fig. 4.16(d) generally remains unchanged, exhibiting a local minimum around $\rho = 0.85$ where a mixture of turbulence modes is observed.

Notably, a significant reduction in the correlation time, from 20 μs to 10 μs, and an increase in the poloidal correlation length, from 4 cm to 6 cm, are observed around $\rho = 0.9 - 1.0$ after ECH is applied, as shown in Fig. 4.16(b) and 4.16(c). These changes may be attributed to the emergence of zonal flow structures and/or Geodesic Acoustic Modes (GAM) following the application of ECH, which leads to a stronger poloidal velocity shear in the turbulence mode velocity, elongates the turbulence eddies in the poloidal direction, and accelerates their decorrelation.
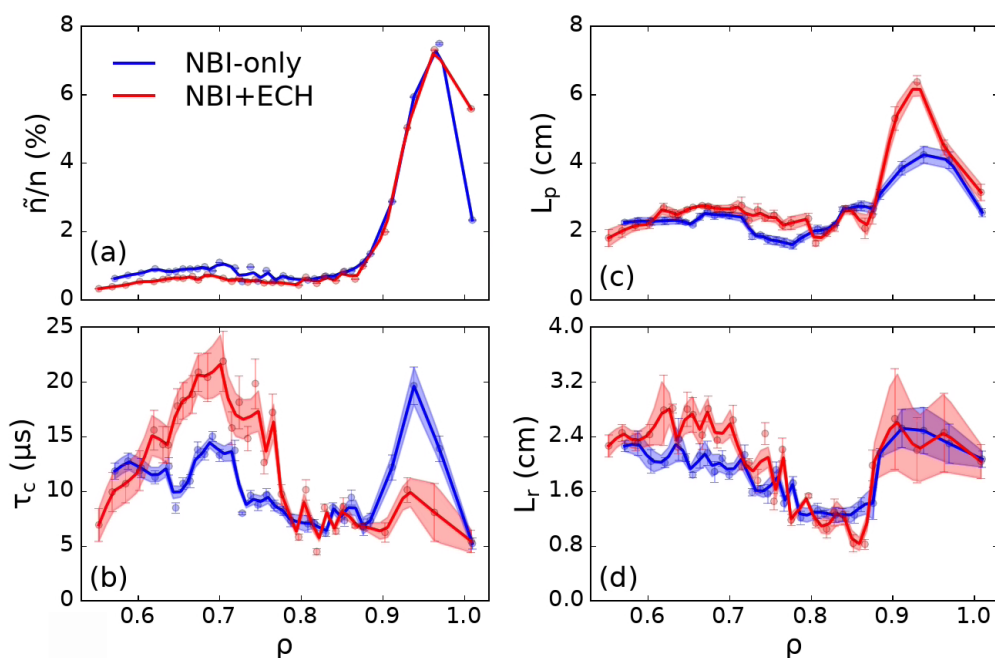
Figure 4.16: Turbulence characteristics: (a) density fluctuation amplitude, (b) correlation time, (c) poloidal correlation length, (d) radial correlation length

4.4   Determination of Reynolds Stress

As introduced in the previous sections, radial velocity fluctuations are obtained from BES velocimetry analysis, and toroidal velocity fluctuation is derived from the Gaussian fits of UF-CHERS data. Therefore, the calculation of toroidal Reynolds stress $\langle \tilde{v}_r \tilde{v}_\phi \rangle$ involves combining results from two distinctive diagnostics and several issues need to be addressed to validate this calculation and ensure its accuracy.

To resolve the local Reynolds stress, BES and UF-CHERS need to measure emissions from the same spatial location at the same time. The spatial alignment is achieved by inserting the two UF-CHERS spatial channels in the middle of the 8×8 BES array. Since UF-CHERS and BES share the same front-end optics, they are viewing at the same radial-poloidal plane. Although there are no BES channels that exactly overlay with the UF-CHERS channels, BES velocimetry will interpolate that point using data from adjacent channels. This interpolation should remain valid as long as the turbulence correlation length is significantly larger than the spatial separation of the BES channels, which is shown to be the case based on the radial and poloidal correlation length measurements from the previous section.

The temporal synchronization is facilitated by the fact that BES and UF-CHERS collect data simultaneously at the same 1 MHz sampling rate, but the digital filter in UF-CHERS introduces a finite time lag on the order of 10 μs. During UF-CHERS data acquisition, the signal is temporally oversampled internally at 10 MHz. A fast-impulse-response (FIR) digital filter is then applied to the oversampled data to anti-alias and suppress signals above approximately 450 kHz, which is then output at the original 1 MHz sampling rate. The consequence of this digital filtering is a finite time delay that must be accounted for, as it could otherwise introduce large and unphysical phase delays between the $10 - 100$ kHz broadband fluctuation data.

This time lag is corrected by aligning the NBI onset time (rising edge of the raw signals) from BES and UF-CHERS with a precision of 1 µs, as shown in Fig. 4.17. For discharges analyzed in this thesis work, the time lag between BES and UF-CHERS raw data is identified to be 20 µs.
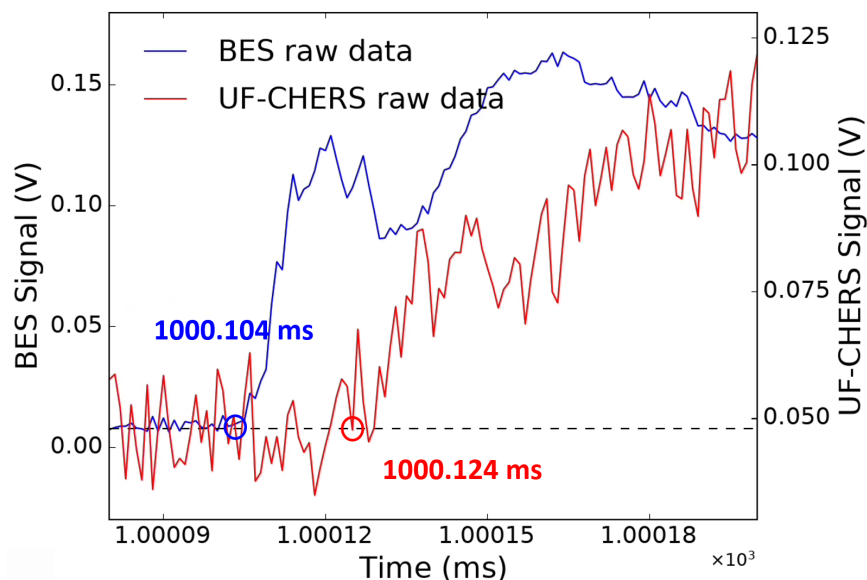
Figure 4.17: Time traces of BES and UF-CHERS raw data from poloidally adjacent channels BES39 and TIF13 (central spectral channel in the second spatial chord)

In addition to spatial alignment and temporal synchronization, it is important to consider that BES and UF-CHERS collect light from different emission sources. BES measures light emitted from neutral beams which are excited by collisions with plasma ions and electrons. For high energy beams with $E_{NBI} \geqslant 40$ keV, ion and impurity collisions tend to dominate the excitation process and electron collisions become negligible [67]. On the other hand, UF-CHERS measures light emitted from low-Z impurity species carbon, which is excited during the charge exchange process with the neutral beam. This means that we are measuring the main ion radial velocity fluctuations $\tilde{v}_r$ and carbon toroidal velocity fluctuations $\tilde{v}_\phi$ to calculate the toroidal Reynolds stress $\langle \tilde{v}_r \tilde{v}_\phi \rangle$.

Given that ion-ion and ion-impurity collision rates are on the order of 100 kHz, it is reasonable to assume thermal equilibrium between the species. Furthermore, since the impurity gyroradii are smaller by a factor of $\sqrt{6}$ than those of deuterium, which in turn are small compared to the eddy structure size ($L \approx 5\rho_i$), and considering they have the same charge-to-mass ratio, the dynamics of the ion response to electrostatic drift wave fluctuations are expected to be similar. Therefore, the calculation of Reynolds stress and other turbulence-driven transport fluxes assumes that the density and velocity fluctuations from main ions and carbon impurities are highly correlated and in phase with each other. Some experimental validations are provided in Fig. 4.9, but a thorough investigation of this assumption is beyond the scope of this thesis.

Figure 4.18 presents the cross-power and cross-phase between radial and toroidal velocity fluctuations measured at $\rho = 0.96$. During the NBI+ECH stage, two distinctive modes are identified. One is at a very low frequency of $2 - 5$ kHz and is suspected to be a zonal flow/GAM due to its frequency range and poloidally extended spatial structure. This low frequency mode has a very large amplitude as shown in the cross-power, but makes little or no contribution to the toroidal Reynolds stress $\langle \tilde{v}_r \tilde{v}_\phi \rangle$ because the cross-phase lies very near $-\pi/2$.

On the other hand, the cross-phase of the higher frequency broad-band mode at 15 to 60 kHz is nearly at zero, indicating that the radial and toroidal velocity fluctuations maximize their contribution to the ensemble average of their product, $\langle \tilde{v}_r \tilde{v}_\phi \rangle$. Figure 4.19 shows the measured toroidal Reynolds stress $\langle \tilde{v}_r \tilde{v}_\phi \rangle$. Upon the application of ECH, a strong toroidal Reynolds stress is observed at the plasma outer core of $\rho = 0.9 - 1.0$, primarily due to this higher-frequency broad-band mode. Notably, although the low frequency zonal flow has no direct contribution to the toroidal Reynolds stress, it may interact with turbulence nonlinearly, acting as a symmetry breaking mechanism that induces the toroidal Reynolds stress [40].
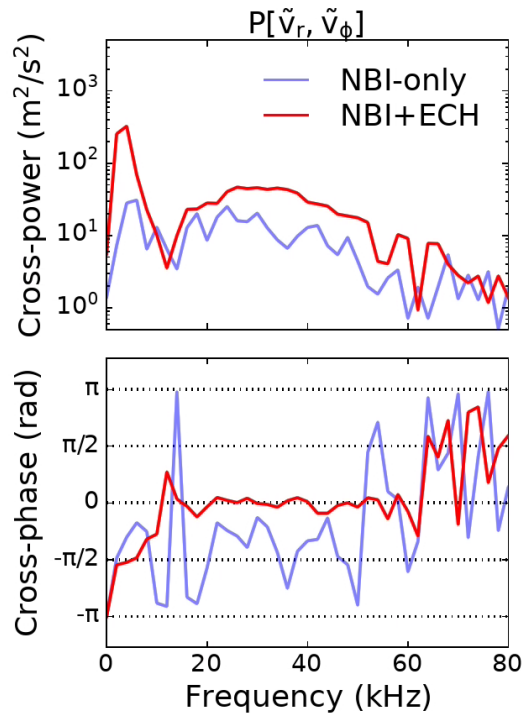
Figure 4.18: Cross-spectral analysis results for radial and toroidal velocity fluctuations at $\rho = 0.96$, for NBI-only (blue) and NBI+ECH (red) stages
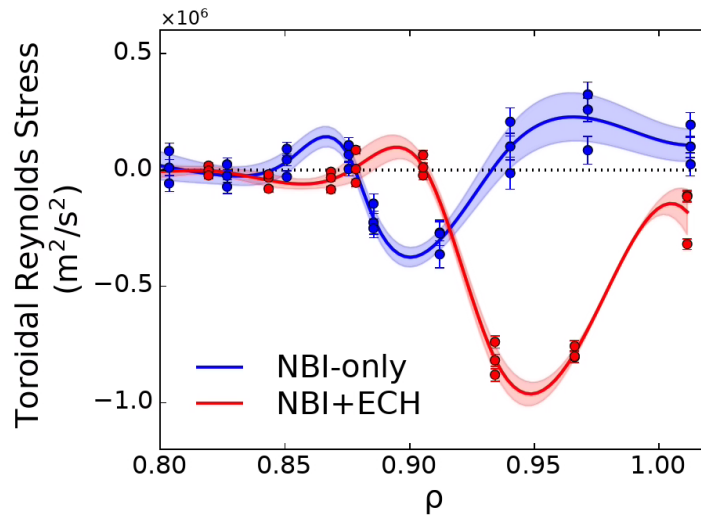
Figure 4.19: Radial profile of momentum fluxes from toroidal Reynolds stress

This low frequency zonal flow is most apparent in the poloidal velocity fluctuation and plays a crucial role in the generation of poloidal Reynolds stress. Figure 4.20 presents the cross-power $P(\tilde{v}_r, \tilde{v}_\theta)$ and cross-phase $\phi(\tilde{v}_r, \tilde{v}_\theta)$ between the radial and poloidal velocity fluctuations at the same radial location of $\rho = 0.96$. Immediately after the application of ECH, the low-frequency mode in the $2 - 5$ kHz range appears, exhibiting a cross-phase close to zero. This alignment in cross-phase maximizes its contribution to the poloidal Reynolds stress, $\langle \tilde{v}_r \tilde{v}_\theta \rangle$. The amplitude of the poloidal velocity fluctuations in the broad-band mode also increases with ECH, resulting in a higher cross-power in general.
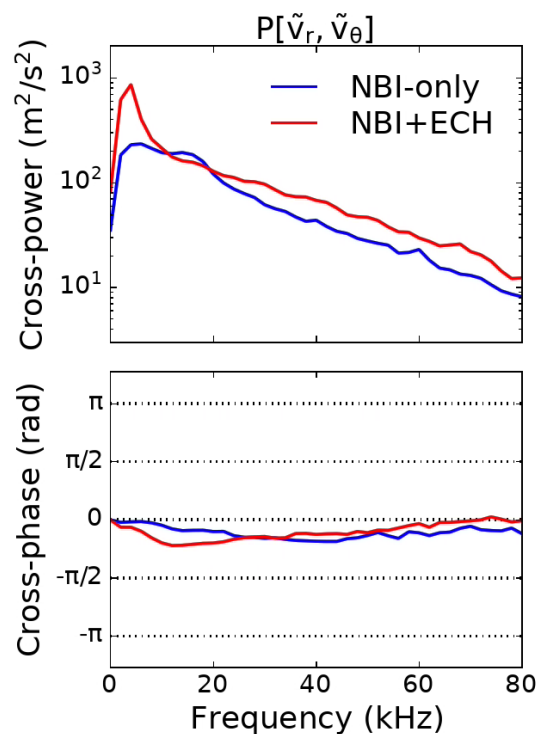
Figure 4.20: Cross-spectral analysis results for radial and poloidal velocity fluctuations at $\rho = 0.96$, for NBI-only (blue) and NBI+ECH (red) stages

Figure 4.21 shows the corresponding poloidal Reynolds stress. Similar to the toroidal Reynolds stress, it is localized at the plasma outer core of

$\rho = 0.9 - 1.0$ and diminishes quickly within $\rho < 0.9$. The magnitude of the poloidal Reynolds stress is almost doubled with the application of ECH. Half of the increase results from the emergence of the low frequency mode at $2 - 5$ kHz. The remaining contribution is attributed to the increased amplitude of fluctuations in the broad-band mode at higher frequencies.
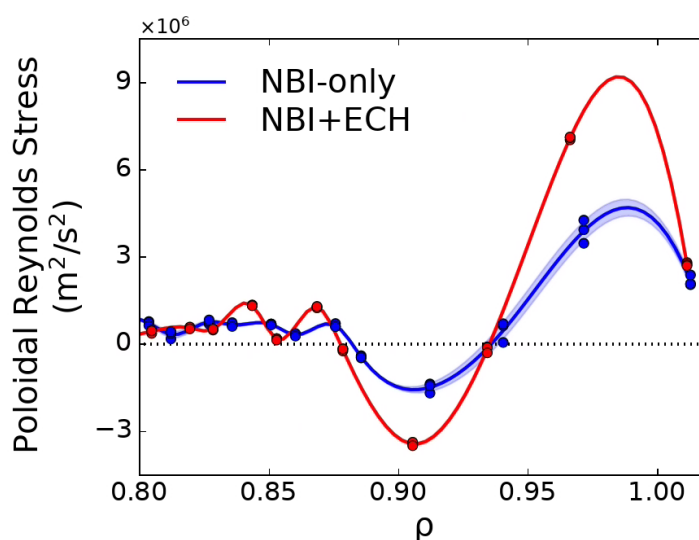
Figure 4.21: Radial profile of momentum fluxes from poloidal Reynolds stress

In conclusion, the experimental determination of toroidal and poloidal Reynolds stress in fusion plasmas is elucidated in this chapter. The combined use of BES and UF-CHERS diagnostics provides a new research capability to study the 3D turbulence velocity field in plasma. This work not only highlights the methodological advancement in measuring turbulent stress but also provides valuable insights into understanding the mechanisms of turbulent stress generation. These experimental findings demonstrate the distinctive roles of broad-band turbulence and zonal flow in the generation of toroidal and poloidal Reynolds stress, illustrate the importance of the cross-phase between velocity fluctuations, and facilitate further research on turbulence-driven intrinsic torque.

5 THE GENERATION OF INTRINSIC TORQUE

Toroidal rotation strongly influences the performance of fusion plasmas since rotation and its radial shear suppress turbulent transport, stabilize MHD modes, and impact the L-H transition power threshold. The turbulence-driven toroidal Reynolds stress $\langle \tilde{v}_r \tilde{v}_\phi \rangle$ is predicted to generate intrinsic toroidal torque via symmetry breaking mechanisms in the stress tensor of the momentum transport equation. To investigate this mechanism, the radial profile of the toroidal Reynolds stress is experimentally determined in the previous chapter using correlated radial and toroidal velocity fluctuation measurements from BES and UF-CHERS.

This chapter presents the major physics results and is structured as follows. Section 5.1 calculates the turbulent momentum flux induced by the measured toroidal Reynolds stress, as well as the turbulence convection and the triplet term. Section 5.2 extracts the residual stress from the measured toroidal Reynolds stress and derives the resulting intrinsic torque. Finally, Section 5.3 reconstructs the rotation profiles using the momentum balance equation, both with and without the derived intrinsic torques, and compares them with the observed rotation profiles.

5.1 Turbulence-driven Momentum Fluxes

In a steady-state axisymmetric toroidal plasma, the radial flux of toroidal momentum Γ_ϕ is given by [26]

$$\Gamma_\phi(r) = \frac{1}{A(r)} \int_0^r \tau(r') \, dV \tag{5.1}$$

where A is the magnetic flux surface area, dV is the differential volume element, and τ denotes various momentum sources. In this experiment, the dominant contribution is from NBI, with $\tau \approx \tau_{NBI}$.

This NBI-driven flux needs to be balanced by the turbulence-driven toroidal momentum flux [26], as given in Eqn. (2.34)

$$\Gamma_\phi(r) = m_i n_i \langle \tilde{v}_r \tilde{v}_\phi \rangle + m_i v_\phi \langle \tilde{n}_i \tilde{v}_r \rangle + m_i \langle \tilde{n}_i \tilde{v}_r \tilde{v}_\phi \rangle \qquad (2.34)$$

which consists of several components, the toroidal Reynolds stress driven flux $m_i n_i \langle \tilde{v}_r \tilde{v}_\phi \rangle$, turbulent convection flux $m_i v_\phi \langle \tilde{n}_i \tilde{v}_r \rangle$, and a nonlinear flux due to the triplet term $m_i \langle \tilde{n}_i \tilde{v}_r \tilde{v}_\phi \rangle$ [40]. In the previous chapter, the toroidal Reynolds stress is experimentally determined using the correlated radial and toroidal velocity fluctuations measured by BES and UF-CHERS. The resulting toroidal momentum flux is presented in Fig. 5.1(a).
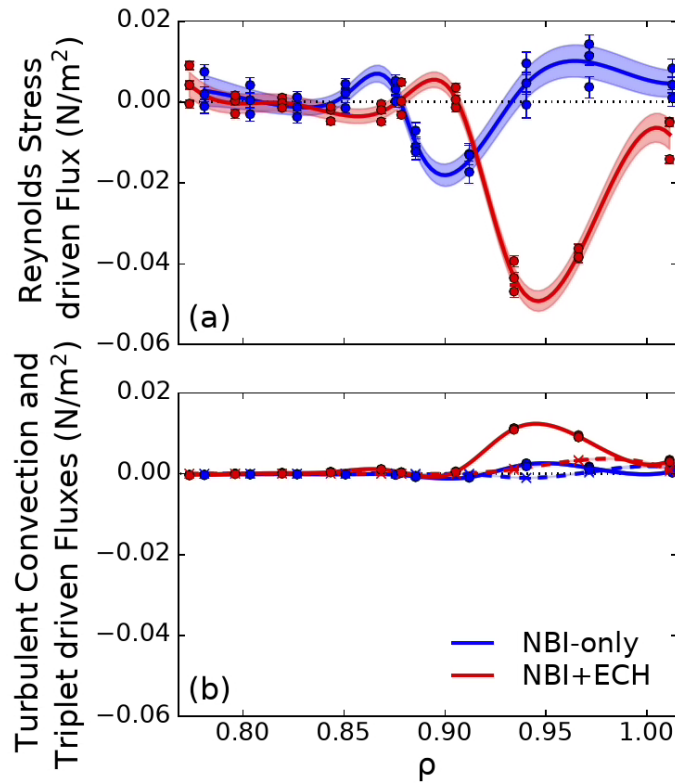
Figure 5.1: Radial profile of toroidal momentum fluxes due to (a) the toroidal Reynolds stress, and (b) the turbulent convection (solid line) and the triplet term (dashed line) during the NBI-only and NBI+ECH stages

As shown in Fig. 5.1(a), after applying ECH, a significant toroidal momentum flux driven by the toroidal Reynolds stress appears at the plasma outer core of $\rho = 0.9 - 1.0$ and peaks at $\rho = 0.95$, primarily due to the higher-frequency broad-band mode as previously described. The radially nonuniform profile results from a combination of the radially varying turbulence amplitude, as shown in Fig. 4.16(a), and the changing cross-phases between the radial and toroidal velocity fluctuations, as demonstrated in Fig. 4.18.

Complementary spectral analyses and calculations have been performed on the correlated density and radial velocity fluctuations to determine the turbulence convection flux and the nonlinear flux due to the triplet term. The results are included in Fig. 5.1(b), where the solid line represents turbulent convection, and the dashed line indicates the triplet term. Notably, both terms are significantly smaller in magnitude compared to the momentum flux driven by the toroidal Reynolds stress. However, the turbulent convection is non-negligible and needs to be considered.

5.2 Extraction of Residual Stress and Intrinsic Torque from the Toroidal Reynolds Stress

As shown in the previous section, the toroidal Reynolds stress $\langle \tilde{v}_r \tilde{v}_\phi \rangle$ is the dominant contribution to the total turbulent momentum flux. It can be further decomposed into a turbulent viscosity χ_ϕ that is proportional to the velocity gradient, a momentum pinch V_{pinch} that is proportional to the velocity itself, and a residual stress Π_ϕ^{Res} [26], as given in Eqn. (2.35)

$$\langle \tilde{v}_r \tilde{v}_\phi \rangle = -\chi_\phi \frac{\partial v_\phi}{\partial r} + V_{pinch} v_\phi + \Pi_\phi^{Res} \qquad (2.35)$$

Residual stress Π_ϕ^{Res} is governed by turbulence and is a complicated function of the density, temperature, pressure, and current gradients [40].

The divergence of the residual stress works effectively as an intrinsic torque, and is responsible for spinning up the plasma from rest in the absence of external momentum input [40].

Residual stress can be extracted from the measured toroidal Reynolds stress by subtracting the velocity dependent terms from Eqn. (2.35). This process is facilitated by achieving a near-zero flat toroidal rotation profile in the outer region of the plasma using both the co- and counter NBI. The turbulent viscosity χ_ϕ can be estimated using the ion thermal diffusivity χ_i and Prandtl number, $Pr = \chi_\phi/\chi_i$. In this study, the ion heat diffusivity χ_i is calculated using transport analysis code TRANSP based on the measured ion temperature profiles and heating sources. Figure 5.2(a) shows the radial profile of the ion thermal diffusivity χ_i calculated by TRANSP, during the NBI-only and NBI+ECH stages.
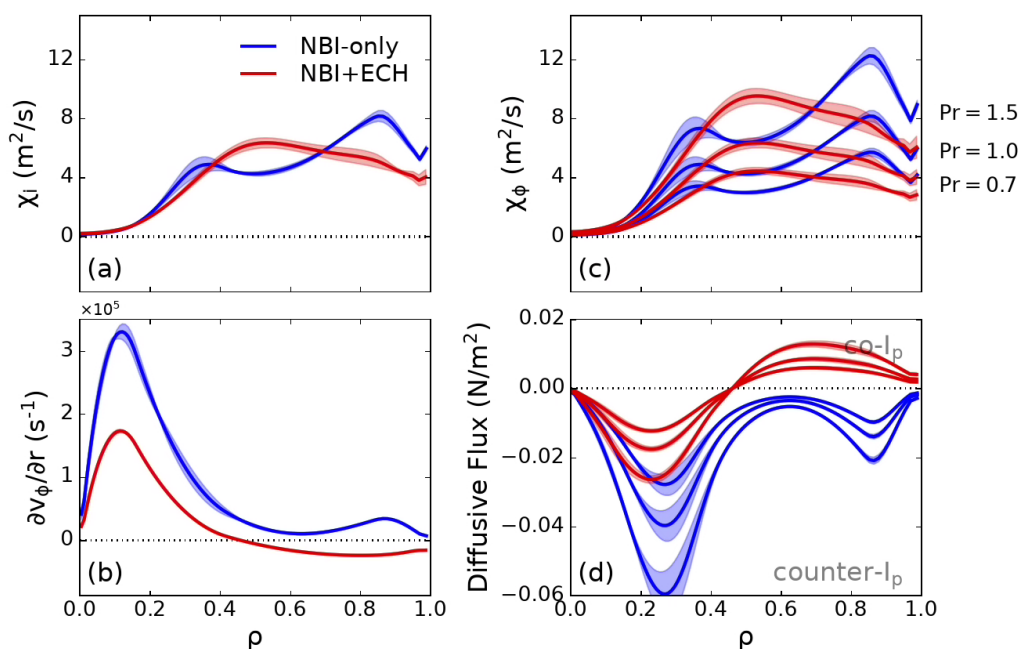
Figure 5.2: Radial profile of (a) the ion thermal diffusivity, (b) turbulent viscosity, (c) toroidal velocity gradients, and (d) the resulting diffusive momentum flux, calculated with various Prandtl numbers of 0.7, 1.0, and 1.5

As discussed in Chapter 2, theory and simulations indicate that the Prandtl number is close to unity in ITG or TEM dominated plasma cores [40, 42, 43]. Experimental measurements of χ_ϕ reveal that the Prandtl number ranges from 0.7 to 2.0 at TFTR [38] and 0.7 to 1.2 at ASDEX-U [44]. Therefore, to assess the influence of turbulent viscosity, we consider Prandtl numbers between 0.7 and 1.5 for this study. Figure 5.2(c) shows the turbulent viscosity χ_ϕ estimated using various Prandtl numbers of $Pr = 0.7$, 1.0, and 1.5, differentiated by solid, dashed, and dotted lines, respectively. The radial gradient of the toroidal velocity, $\partial v_\phi / \partial r$, is shown in Fig. 5.2(b). The velocity gradient driven diffusive toroidal momentum flux, calculated as $-m_i n_i \chi_\phi \partial v_\phi / \partial r$, is shown in Fig. 5.2(d).

The momentum pinch, V_{pinch}, is then estimated from the turbulent viscosity using a physical model based on the turbulent equipartition (TEP) theory [45], as described in Eqn. (2.37).

$$V_{TEP} = 2\chi_\phi \left(-\frac{F + \epsilon r/a}{R} \right) \tag{2.37}$$

where ϵ is the inverse aspect ratio and F represents the poloidal asymmetry of turbulence amplitude. $F = 0$ corresponds to poloidally symmetric flute-like turbulence intensity and $F \sim 1$ corresponds to turbulence with a strongly outward ballooning structure [43].

In this analysis, a range of F values from 0 to 1 are examined. Figures 5.3(a)-(b) and 5.3(c)-(d) present the estimated TEP pinch velocity, V_{TEP}, and the corresponding pinch-induced turbulent momentum flux, $m_i n_i V_{TEP} v_\phi$, with $F = 0$ and $F = 1$, respectively. Notably, the pinch-induced momentum flux constitutes a small portion of the total momentum flux induced by the toroidal Reynolds stress, thereby having minimal impact on the extracted residual stress and intrinsic torque. Examination of the reconstructed rotation profile also reveals that while a larger pinch leads to stronger peaking of toroidal rotation in the core, the results in $\rho = 0.8 - 1.0$ remain mostly unaffected due to the low toroidal velocity.
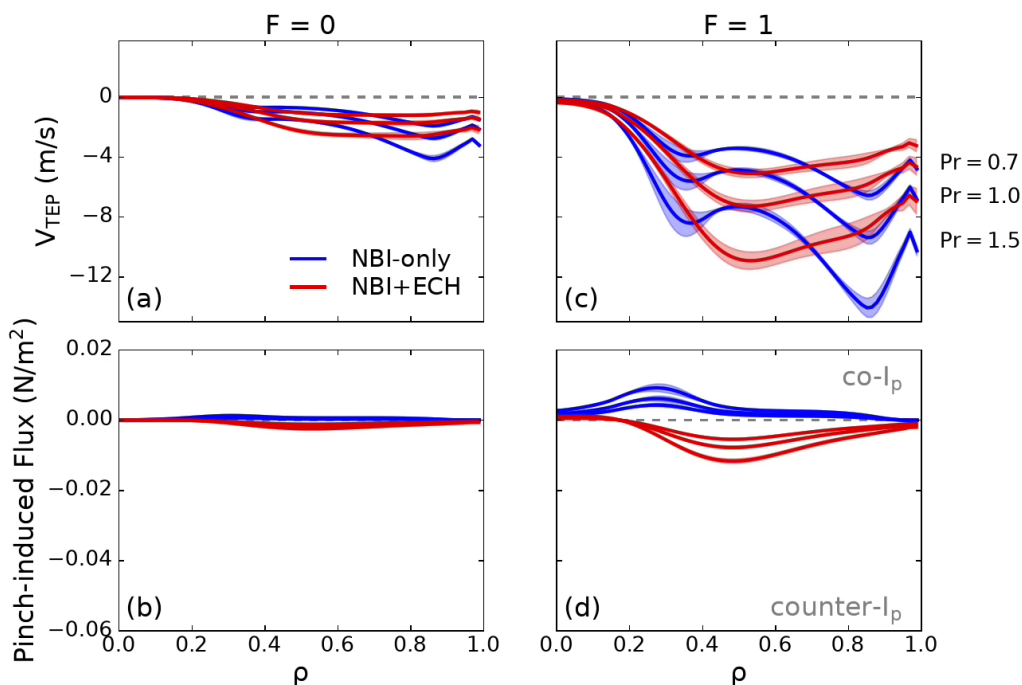
Figure 5.3: Radial profile of (a) the TEP pinch velocity estimated with $F = 0$, and (b) its resulting toroidal momentum flux, as well as (c) the TEP pinch velocity estimated with $F = 1$ and (d) its resulting toroidal momentum flux, calculated with various Prandtl numbers of 0.7, 1.0, and 1.5

With the estimated turbulent viscosity and TEP pinch, the residual stress and its induced momentum flux are extracted from the measured toroidal Reynolds stress. The resulting intrinsic torque is calculated as the negative radial gradient of the momentum flux driven by residual stress, as given in Eqn. (2.42)

$$\tau_{intrinsic} = -\frac{\partial}{\partial r}\left(m_i n_i \Pi_\phi^{Res}\right) \tag{2.42}$$

Figure 5.4(a) shows the radial profile of the momentum flux driven by the residual stress, with the shaded area bounded by the Prandtl number variation from 0.7 to 1.5, F variation from 0 to 1, and Reynolds stress measurement uncertainties. Both the NBI-only and NBI+ECH stages

achieve small rotation and relatively flat rotation profiles, resulting in minimal dependence on the variations in pinch velocity and turbulent viscosity associated with the Prandtl number and F values.

The derived intrinsic torque density is shown in Fig. 5.4(b). During the NBI-only stage, the volume-integrated intrinsic torque (over $\rho = 0.78-1.0$) is nearly zero. In the NBI+ECH stage, a 2.5 Nm torque is observed between $\rho = 0.9 - 0.95$ and -2.1 Nm between $\rho = 0.95 - 1.0$, resulting in a net co-current intrinsic torque of 0.4 ± 0.05 Nm, which is comparable to the -0.75 Nm counter-current NBI torque. Notably, although the net intrinsic torque is nearly zero in the NBI-only stage, it still noticeably alters the local velocity gradient and therefore the reconstructed rotation profile.
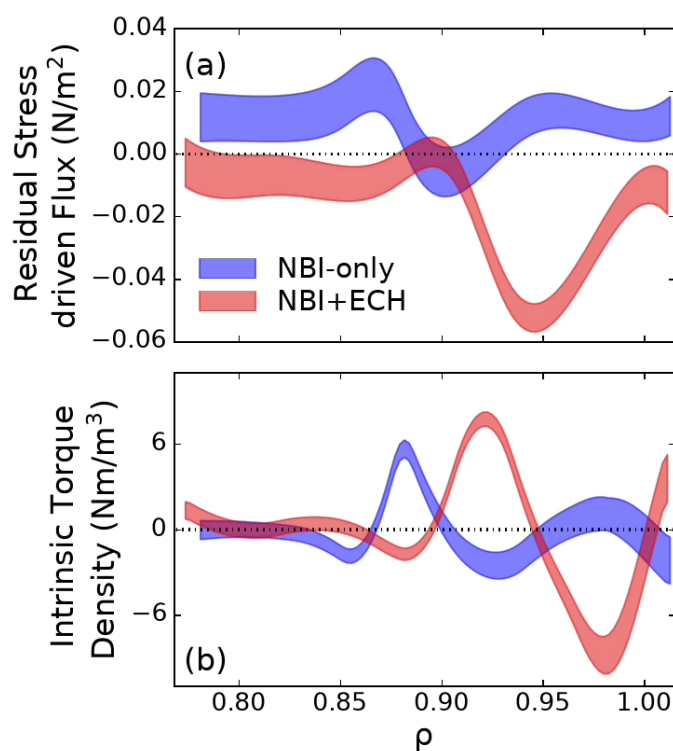
Figure 5.4: Radial profiles of (a) the momentum flux induced by the extracted residual stress, and (b) its resulting intrinsic torque density, evaluated at $Pr = 0.7 - 1.5$, during NBI-only (blue shaded) and NBI+ECH (red shaded) stages

5.3 Comparison Between the Reconstructed and CER Measured Rotation Profiles

To evaluate the impact of the turbulence-driven intrinsic torque, toroidal rotation profiles are reconstructed using the momentum balance equation, as shown in Eqn. (5.2)

$$\frac{1}{A(r)} \int_0^r \tau_{NBI}(r') \, dV = m_i n_i \langle \tilde{v}_r \tilde{v}_\phi \rangle + m_i v_\phi \langle \tilde{n}_i \tilde{v}_r \rangle + m_i \langle \tilde{n}_i \tilde{v}_r \tilde{v}_\phi \rangle \quad (5.2)$$

which is equivalent to

$$\begin{aligned}
\frac{1}{A(r)} &\int_0^r \tau_{NBI}(r') + \tau_{intrinsic}(r') \, dV \\
&= m_i n_i \left(-\chi_\phi \frac{\partial v_\phi}{\partial r} + V_{TEP} v_\phi \right) + m_i v_\phi \langle \tilde{n}_i \tilde{v}_r \rangle + m_i \langle \tilde{n}_i \tilde{v}_r \tilde{v}_\phi \rangle
\end{aligned} \quad (5.3)$$

Among all the terms in Eqn. (5.3), the magnetic flux surface area, A, and the differential volume element, dV, are obtained from the equilibrium reconstruction. The NBI torque deposition profile, τ_{NBI}, is calculated using the transport code TRANSP. The turbulent momentum fluxes induced by the toroidal Reynolds stress, $m_i n_i \langle \tilde{v}_r \tilde{v}_\phi \rangle$, turbulent convection, $m_i v_\phi \langle \tilde{n}_i \tilde{v}_r \rangle$, and the triplet term, $m_i \langle \tilde{n}_i \tilde{v}_r \tilde{v}_\phi \rangle$, are experimentally determined using fluctuation measurements from BES and UF-CHERS. The residual stress is extracted from the measured toroidal Reynolds stress by subtracting the estimated turbulent viscosity and pinch terms (χ_ϕ and V_{TEP}). Finally, the intrinsic torque, $\tau_{intrinsic}$, is derived as the radial gradient of the residual stress, leaving the toroidal velocity, v_ϕ, and its radial gradient, $\partial v_\phi / \partial r$, as the only unknown terms in Eqn. (5.3).

The rotation physics inside the separatrix determines the local velocity gradient but not the rotation itself. Therefore, setting the correct boundary condition is essential in reconstructing the rotation profile, as a change in

the edge rotation can shift the rotation at all radii. The rotation physics at the proximity of the scrape-off layer (SOL) is a complicated subject that involves various mechanisms such as ion-orbit loss, momentum transport by neutrals, radial SOL currents, and other edge-specific physics [81, 82]. In this thesis, we focus on the core rotation, which is treated separately from the SOL rotation. Hence, a complete consideration of the edge rotation physics is beyond the scope of this work.

Figure 5.5 shows the calculated velocity gradients and the reconstructed toroidal rotation profiles at $\rho = 0.78-1.0$. The reconstruction of the velocity profile begins with the measured toroidal rotation at the separatrix, which establishes the essential boundary condition. With this initial condition, the velocity gradient at the separatrix is calculated, thereby determining
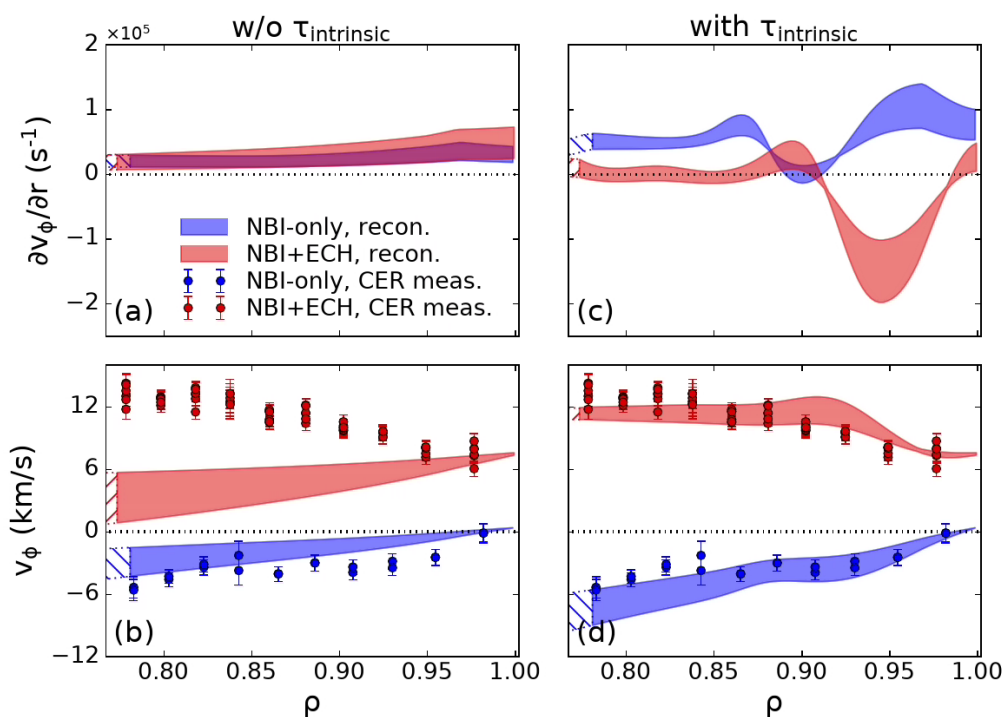
Figure 5.5: Radial profile of the velocity gradients and toroidal rotation at $\rho = 0.8-1.0$, (a)-(b) without and (c)-(d) with the derived intrinsic torque, during NBI-only (blue shaded) and NBI+ECH (red shaded) stages

the toroidal velocity at the next radial position. This process is iterated to reconstruct the entire radial profile of the toroidal rotation. The reconstructed rotation profile (shaded area) is then compared to the CER measurements (data points).

Figure 5.5(a) shows the reconstructed rotation gradient without the inferred intrinsic torque. The calculated velocity gradients for the NBI-only and NBI+ECH stages exhibit significant similarities, which arise from the consistent NBI torque and comparable turbulent viscosity across both stages. Consequently, the reconstructed rotation profiles exhibit comparable magnitudes and similar shapes, as shown in Fig. 5.5(b). Except, in the NBI+ECH stage, the reconstructed profile slightly shifts towards the co-current direction, which is attributed to the different boundary conditions at $\rho = 1.0$.

Figure 5.5(c) shows the reconstructed rotation gradient with the inferred intrinsic torque. Notably, the measured momentum fluxes induced by turbulent convection and the triplet term are also included. Incorporating the intrinsic torque significantly alters the velocity gradients at $\rho = 0.9 - 1.0$. The oppositely directed intrinsic torques result in distinctive rotation profiles being reconstructed for the NBI-only and NBI+ECH stages, shifting the rotation profile slightly towards the counter-current direction during the NBI-only stage and strongly towards the co-current direction during the NBI+ECH stage, as shown in Fig. 5.5(d).

Comparing the reconstructed rotation profiles with CER data reveals that, regardless of the Prandtl number selected within the range of 0.7 to 1.5, or F values between 0 and 1, the NBI torque alone cannot reproduce the observed rotation profile nor account for the change in rotation after ECH is applied. However, by incorporating the derived intrinsic torque into the momentum balance equation, the reconstructed rotation profiles then achieve good agreement with CER data and successfully reproduce the observed changes in rotation profile in response to ECH.

Although the experimentally determined intrinsic torque profile is limited to the radial region of $\rho = 0.78 - 1.0$, it is believed to capture the essential characteristics of the intrinsic torque. Since the magnitude of turbulent stress and the resulting intrinsic torque are closely correlated with the turbulence amplitude, which significantly decreases towards the plasma core, as shown in Fig. 4.16(a), it is reasonable to assume that the intrinsic torque continues to diminish within $\rho = 0.8$. Figure 5.6(a) and 5.6(b) show the complete radial profiles of the reconstructed rotation without and with the measured torque, respectively. The results demonstrate improved agreement with CER data at the inner core when the inferred turbulence-driven intrinsic torques are included.
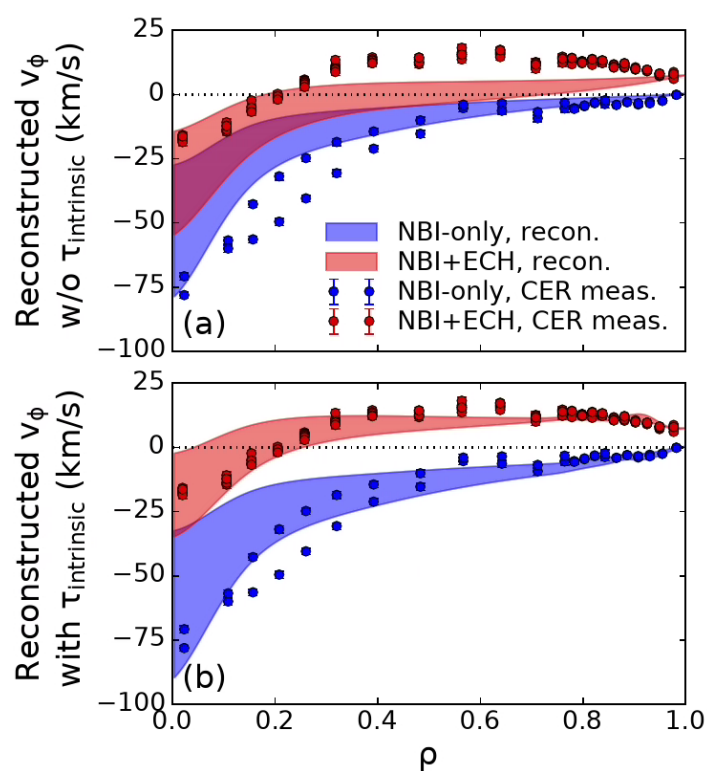
Figure 5.6: Comparison between the CER measurements (data points) and the reconstructed (shaded area) rotation profiles (a) without and (b) with intrinsic torque, during the NBI-only (blue) and NBI+ECH (red) stages.

Notably, the NBI torque density, ion heat diffusivity, and other quantities calculated by TRANSP are flux surface-averaged, while Reynolds stress is measured at the outboard mid-plane. We assume the toroidal Reynolds stress remains constant along the flux surface, but its magnitude likely scales with turbulence intensity, assuming the cross-phase relationship between the 3D turbulence velocity field remains consistent on the flux surface. Therefore, the flux surface-averaged Reynolds stress might be smaller than the measured value, since turbulence tends to be stronger on the low-field side.

This estimation of flute-like turbulence, as applied in the calculations, may be reasonable for an L-mode discharge dominated by electrostatic drift wave instabilities, such as ITG and TEM. However, to fully address the poloidal variation of Reynolds stress, it is necessary to perform 3D global turbulence simulations [83], which is planned for future work but beyond the scope of this thesis.

In conclusion, by adjusting the ion and electron heat fluxes using different combinations of NBI and ECH, we effectively alter the mixture of turbulence modes in the outer region of the plasma from a predominantly electron mode to a more complex mixture of ion and electron modes. This transition results in significant changes in the magnitude and cross-phase relationship of the turbulence-driven velocity field, thereby affecting the toroidal Reynolds stress and its resulting intrinsic torque. Comparing the reconstructed rotation profiles and CER measurements demonstrates the crucial role of intrinsic torque in shaping the rotation profile, validates the theory of turbulence-driven intrinsic torque, and supports the use of turbulence models to predict rotation profiles.

6 SUMMARY AND CONCLUSIONS

Turbulence-driven nonuniform Reynolds stress is predicted to generate intrinsic rotation in plasmas. To investigate this mechanism, turbulent stresses and intrinsic torque are determined in L-mode plasma cores via correlated density and velocity fluctuation measurements in DIII-D. Dedicated experiments are conducted with co- and counter-current NBI to control the net torque input and achieve the desired rotation profiles. ECH is applied to alter the ion and electron heat fluxes and therefore the mixture of turbulence modes. High-quality fluctuation data are obtained using BES and UF-CHERS, demonstrating advanced diagnostics capabilities in measuring the 3D turbulence velocity field.

6.1 Summary of Major Results

This thesis addresses three central physics questions: (1) how Reynolds stress is generated, (2) what characteristics the Reynolds stress profile exhibits, and (3) whether it can explain the measured rotation profile.

To address the first question, high-quality density fluctuation measurements are obtained using BES. Velocimetry analysis is then applied to the 2D density fluctuation images to infer both radial and poloidal velocity fluctuations. UF-CHERS channels are inserted at the center of the BES array and measure the toroidal velocity fluctuations. The cross-spectral analysis results between radial and toroidal velocity fluctuations provide valuable insights into the generation of Reynolds stress.

During the NBI+ECH stage, two distinctive modes are identified. One is at a very low frequency of $2-5$ kHz and is suspected to be a zonal flow and/or GAM structure. This zonal flow has a very large amplitude but makes little or no contribution to the toroidal Reynolds stress because its cross-phase lies closely at $-\pi/2$. On the other hand, the cross-phase of

the higher frequency broad-band mode is nearly at zero, which means that the radial and toroidal velocity fluctuations are in phase with each other and maximize their contribution in $\langle \tilde{v}_r \tilde{v}_\phi \rangle$. These results reveal the distinctive roles of broad-band turbulence and zonal flow in the generation of toroidal Reynolds stress.

Using the Prandtl number and the physics model of the TEP pinch, residual stress is extracted from the measured Reynolds stress by subtracting the velocity-dependent terms. Intrinsic torque is then derived from the radial gradient of the residual stress. During the NBI-only stage, the volume-integrated intrinsic torque is nearly zero. Upon the application of ECH, a strong rotation drive is identified at the plasma edge, resulting in a net co-current intrinsic torque of 0.4 ± 0.05 Nm, which is comparable to the -0.75 Nm counter-current NBI torque.

To evaluate the impact of this turbulence-driven intrinsic torque, toroidal rotation profiles are reconstructed using the momentum balance equation. Results show that, regardless of the Prandtl number chosen between 0.7 and 1.5 and F values in the TEP pinch between 0 and 1, the NBI torque alone cannot reproduce the observed rotation profile nor explain the change in rotation after ECH is applied. However, by incorporating the inferred turbulence-driven intrinsic torque, the velocity gradients near the edge are significantly altered. The reconstructed rotation profiles then show good agreement with CER data and successfully reproduce the observed rotation changes due to ECH.

This thesis work provides the first direct measurement of turbulent stresses in fusion-grade plasma cores and infers the resulting intrinsic torque by integrating experimental data with theoretical physics models. The results show convincing consistency with the current theory of turbulence-driven intrinsic torque and support the use of predictive modeling for intrinsic rotation via turbulence models in ITER and other future magnetic fusion facilities.

6.2   Future Work

In diagnostic development, expanding the current 2-channel UF-CHERS system to 4 channels will benefit the toroidal velocity fluctuation measurements. Additionally, further improvements can be made to the UF-CHERS data analysis techniques to enhance the accuracy of Gaussian fitting and the precision of derived quantities. It is also possible to apply the same cross-spectral and cross-correlation analysis technique to BES measured density fluctuations and UF-CHERS measured temperature fluctuations to directly measure the turbulent heat flux.

In terms of physics research, results from this thesis demonstrate that the generation of Reynolds stress depends on the cross-phase relationship between fluctuating velocities. A natural follow-up question will be understanding the mechanisms that determine the cross-phase between fluctuating velocities under various turbulence modes and plasma conditions. For example, experiments with ohmic-heated plasmas at Alcator C-Mod have found that the intrinsic toroidal rotation scales linearly with the stored energy normalized to the plasma current [16]. This empirical scaling can be studied by performing similar analyses on a set of discharges with lower plasma current in the experiments we conducted.

Another relevant study concerns zonal flow. Although zonal flow does not directly contribute to toroidal Reynolds stress, it may interact nonlinearly with turbulence, acting as a symmetry-breaking mechanism that induces turbulent stress. This nonlinear interaction between zonal flows and turbulence can be investigated via bicoherence analysis of BES and UF-CHERS fluctuation measurements.

Comparing experimentally measured turbulent stress and intrinsic torque with the predictions from gyrokinetic simulations validates the theoretical models and provides a deeper understanding of turbulence dynamics. These simulations also reveal the dominant turbulence modes and how these modes evolve under different plasma conditions. Further-

more, to comprehensively address the poloidal variation of Reynolds stress and its impact on plasma rotation, it is necessary to perform 3D global gyrokinetic turbulence simulations. Some of these simulation efforts are ongoing. Initial results from the linear gyrokinetic simulations have shown promising agreement with experimental observations.

Finally, the good agreement between the reconstructed rotation profiles and the CER measurements supports the use of turbulence models to predict rotation in future magnetic fusion facilities, such as ITER. Therefore, applying and extrapolating these results from the DIII-D tokamak to other machines will help to further validate and extend the current findings. Besides prediction, it is also feasible to utilize the turbulence-driven intrinsic torque to control the rotation profile, thereby improving tokamak performance. For example, strong nonuniform Reynolds stress near the edge can cause large velocity shear and therefore suppress turbulence and turbulent transport, which could possibly be achieved by fine-tuning the heating power and/or density profile.

A ANALYSIS CODES

A.1 TRANSP

TRANSP is a computational code developed by the Princeton Plasma Physics Laboratory (PPPL) to infer the plasma transport processes by analyzing tokamak experimental data [84]. This code is maintained and run at the PPPL, and is accessible for offsite users.
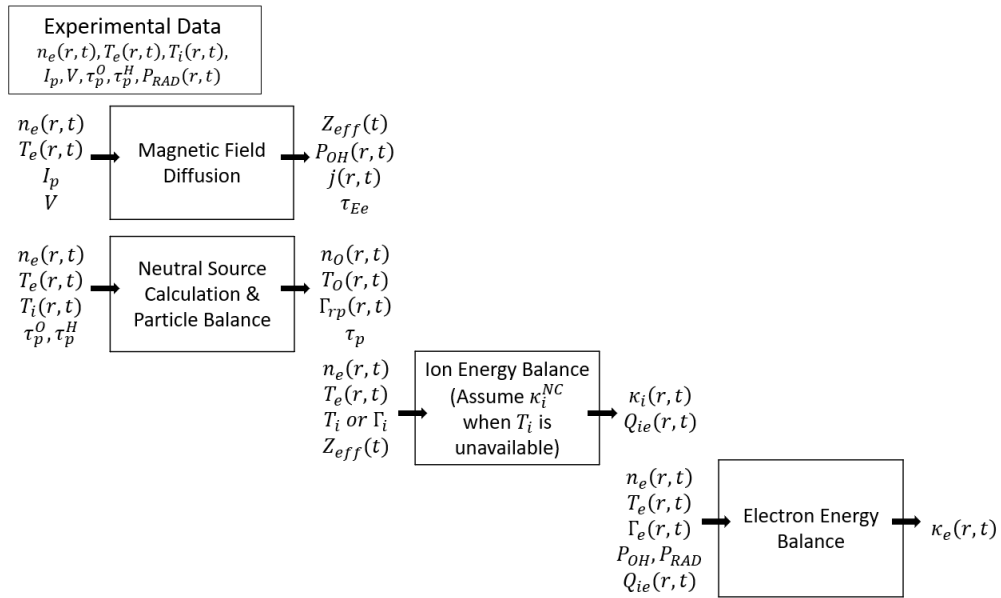
Figure A.1: The general structure of TRANSP, reproduced from [84]

The general structure of this time dependent transport analysis code is shown in Figure A.1. The data inputs include plasma profile measurements of electron density $n_e(r, t)$, electron temperature $T_e(r, t)$, ion temperature $T_i(r, t)$, plasma current I_p, surface voltage V, and the radiated power $P_{RAD}(r, t)$ [84]. The code solves the magnetic field diffusion equation for the poloidal magnetic field $B_\theta(r, t)$, effective charge $Z_{eff}(t)$ and current density $j(r, t)$. With these quantities, the ohmic input power

$P_{OH}(r,t)$, electron energy confinement time τ_{Ee} and the safety factor q are calculated. Neutral density $n_O(r,t)$ and neutral temperature $T_O(r,t)$ are determined from the neutral source calculation. And the radial particle flux $\Gamma_{rp}(r,t)$ and particle confinement time τ_p are determined from the particle conservation equation. The ion heat diffusivity χ_i can be calculated from the ion temperature profile using the ion energy balance or estimated by neoclassical theory when a detailed ion temperature profile is unavailable. Finally, the electron heat diffusivity χ_e is derived from the electron energy balance equation with the inputs from previous calculations. For the purpose of this thesis, TRANSP is applied to reconstruct general plasma profiles from experimental data, derive ion heat diffusivity and calculate NBI torque deposition via the integrated NUBEAM module.

B   ADDITIONAL ANALYSIS

This appendix extends the analyses presented in Chapters 4 and 5, focusing on the intermediate time case (steady NBI-only stage, from $2.0 - 3.0$ s) between the conditions studied in the previous chapters. It aims to provide an additional case analysis for a comprehensive understanding of the turbulence-driven intrinsic torque and its influence on toroidal rotation profiles under varying plasma conditions and turbulence features.

The intermediate time case analysis builds on the experimental framework and analysis workflow established in the previous chapters. It uses
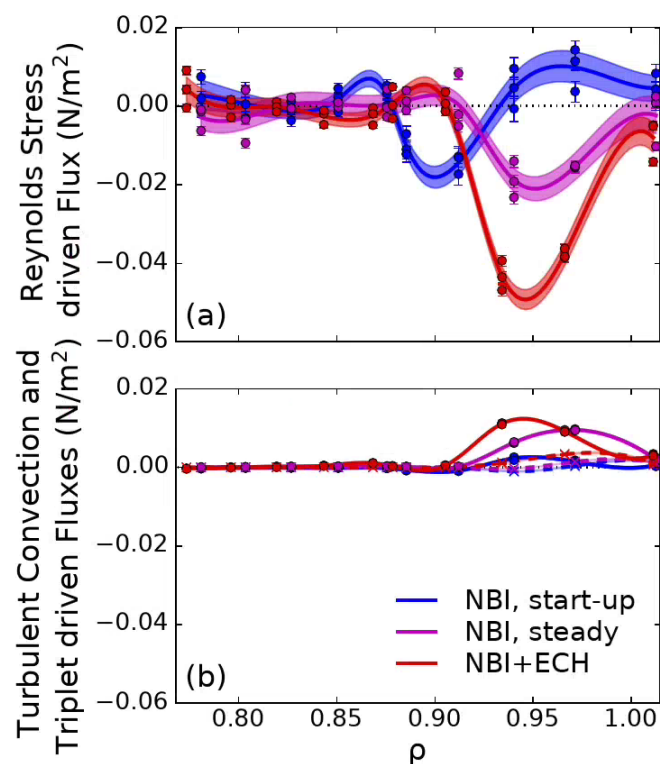
Figure B.1: Radial profile of toroidal momentum fluxes due to (a) the toroidal Reynolds stress, and (b) the turbulent convection (solid line) and the triplet term (dashed line) during the NBI start-up, NBI steady, and NBI+ECH stages

correlated density and velocity fluctuation measurements from the BES and UF-CHERS diagnostics to determine the toroidal Reynolds stress, as shown in Fig. B.1. The residual stress and intrinsic torque are extracted from the measured toroidal Reynolds stress by subtracting all the velocity dependent terms, as shown in Fig. B.2. The volume-integrated intrinsic torque between $\rho = 0.8 - 1.0$ for the intermediate case is near zero.
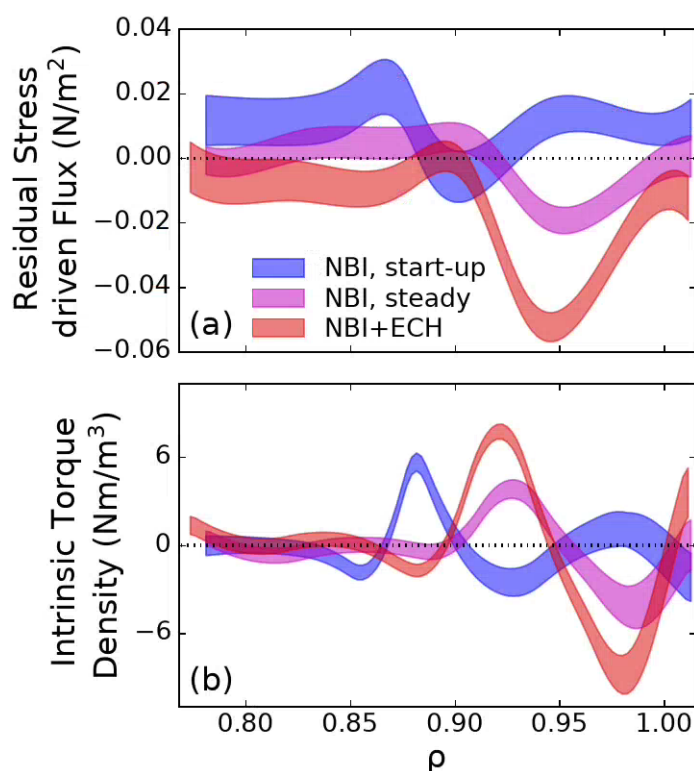
Figure B.2: Radial profiles of (a) the momentum flux induced by the extracted residual stress, and (b) its resulting intrinsic torque density, evaluated at $Pr = 0.7 - 1.5$ and $F = 0 - 1$, during NBI start-up (blue shaded), NBI steady (magenta shaded) and NBI+ECH (red shaded) stages

The toroidal rotation profiles are reconstructed using the momentum balance equation, both with and without the inferred intrinsic torque. Comparisons with the CER data demonstrate slightly better agreement when the inferred turbulence-driven intrinsic torque is incorporated, as

shown in Fig. B.3. In conclusion, the additional analysis of the intermediate case presented in this appendix agrees with the two other cases and reinforces the conclusions drawn in the preceding chapters.
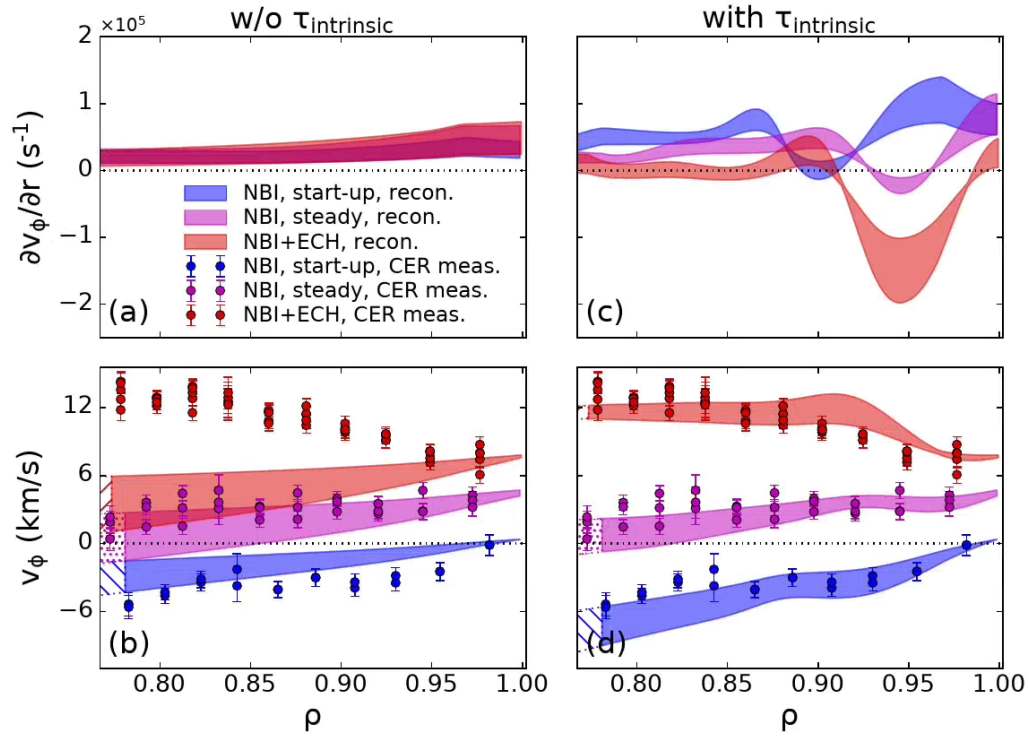
Figure B.3: Radial profile of the velocity gradients and toroidal rotation at $\rho = 0.8 - 1.0$, (a)-(b) without and (c)-(d) with the derived intrinsic torque, during NBI start-up (blue shaded), NBI steady (magenta shaded), and NBI+ECH (red shaded) stages

BIBLIOGRAPHY

---

[1] R.S. Pease. Global energy scenarios and the potential role of fusion energy in the 21st century. *Journal of Nuclear Materials*, 191-194:7–14, 1992. Fusion Reactor Materials Part A.

[2] International Energy Agency. World energy balances 2020. https://www.iea.org/data-and-statistics, 2020.

[3] Kirsten Haupt. Fusion machines: Searching for the perfect shape. https://www.iter.org/newsline/-/3037, 1970.

[4] J. Wesson and D.J. Campbell. *Tokamaks*. International Series of Monogr. OUP Oxford, 2011.

[5] Slavomir Entler, Jan Horacek, Tomas Dlouhy, and Vaclav Dostal. Approximation of the economy of fusion energy. *Energy*, 152:489–497, 2018.

[6] R Aymar, P Barabaschi, and Y Shimomura. The iter design. *Plasma Physics and Controlled Fusion*, 44(5):519, 2002.

[7] P. Batistoni, D. Campling, S. Conroy, D. Croft, T. Giegerich, T. Huddleston, X. Lefebvre, I. Lengar, S. Lilley, A. Peacock, M. Pillon, S. Popovichev, S. Reynolds, R. Vila, R. Villari, and N. Bekris. Technological exploitation of deuterium–tritium operations at jet in support of iter design, operation and safety. *Fusion Engineering and Design*, 109-111:278–285, 2016. Proceedings of the 12th International Symposium on Fusion Nuclear Technology-12 (ISFNT-12).

[8] Kikuchi Mitsuru. A review of fusion and tokamak research towards steady-state operation: A jaea contribution. *Energies*, 3, 11 2010.

[9] L. Schmitz. The role of turbulence–flow interactions in l- to h-mode transition dynamics: recent progress. *Nuclear Fusion*, 57(2):025003, jan 2017.

[10] P. W. Terry. Suppression of turbulence and transport by sheared flow. *Rev. Mod. Phys.*, 72:109–165, Jan 2000.

[11] K. H. Burrell. Role of sheared E × B flow in self-organized, improved confinement states in magnetized plasmas. *Physics of Plasmas*, 27(6):060501, 06 2020.

[12] G.R. McKee, P. Gohil, D.J. Schlossberg, J.A. Boedo, K.H. Burrell, J.S. deGrassie, R.J. Groebner, R.A. Moyer, C.C. Petty, T.L. Rhodes, L. Schmitz, M.W. Shafer, W.M. Solomon, M. Umansky, G. Wang, A.E. White, and X. Xu. Dependence of the l- to h-mode power threshold on toroidal rotation and the link to edge turbulence dynamics. *Nuclear Fusion*, 49(11):115016, sep 2009.

[13] S. Suckewer, H. P. Eubank, R. J. Goldston, E. Hinnov, and N. R. Sauthoff. Toroidal plasma rotation in the princeton large torus induced by neutral-beam injection. *Phys. Rev. Lett.*, 43:207–210, Jul 1979.

[14] B. A. Grierson, C. Chrystal, S. R. Haskey, W. X. Wang, T. L. Rhodes, G. R. McKee, K. Barada, X. Yuan, M. F. F. Nave, A. Ashourvan, and C. Holland. Main-ion intrinsic toroidal rotation across the itg/tem boundary in diii-d discharges during ohmic and electron cyclotron heating. *Physics of Plasmas*, 26(4):042304, 2019.

[15] M. Yoshida, Y. Sakamoto, M. Honda, Y. Kamada, H. Takenaga, N. Oyama, H. Urano, and the JT-60 Team. Core and edge toroidal rotation study in jt-60u. *Nuclear Fusion*, 52(2):023024, feb 2012.

[16] J. E. Rice, J. W. Hughes, P. H. Diamond, Y. Kosuga, Y. A. Podpaly, M. L. Reinke, M. J. Greenwald, Ö. D. Gürcan, T. S. Hahm, A. E. Hubbard, E. S. Marmar, C. J. McDevitt, and D. G. Whyte. Edge temperature gradient as intrinsic rotation drive in alcator c-mod tokamak plasmas. *Phys. Rev. Lett.*, 106:215001, May 2011.

[17] W. D. Lee, J. E. Rice, E. S. Marmar, M. J. Greenwald, I. H. Hutchinson, and J. A. Snipes. Observation of anomalous momentum transport in tokamak plasmas with no momentum input. *Phys. Rev. Lett.*, 91:205003, Nov 2003.

[18] W.M. Solomon, K.H. Burrell, A.M. Garofalo, A.J. Cole, R.V. Budny, J.S. deGrassie, W.W. Heidbrink, G.L. Jackson, M.J. Lanctot, R. Nazikian, H. Reimerdes, E.J. Strait, and M.A. Van Zeeland and. Advances in understanding the generation and evolution of the toroidal rotation profile on DIII-d. *Nuclear Fusion*, 49(8):085005, jul 2009.

[19] P.H. Diamond, Y. Kosuga, Ö.D. Gürcan, C.J. McDevitt, T.S. Hahm, N. Fedorczak, J.E. Rice, W.X. Wang, S. Ku, J.M. Kwon, G. Dif-Pradalier, J. Abiteboul, L. Wang, W.H. Ko, Y.J. Shi, K. Ida, W. Solomon, H. Jhang, S.S. Kim, S. Yi, S.H. Ko, Y. Sarazin, R. Singh, and C.S. Chang. An overview of intrinsic torque and momentum transport bifurcations in toroidal plasmas. *Nuclear Fusion*, 53(10):104019, sep 2013.

[20] Y. Kosuga, P. H. Diamond, and Ö. D. Gürcan. On the efficiency of intrinsic rotation generation in tokamaks. *Physics of Plasmas*, 17(10):102313, 2010.

[21] G. R. McKee, R. J. Fonck, M. W. Shafer, I. U. Uzun-Kaymak, and Z. Yan. Wide-field turbulence imaging with beam emission spectroscopya). *Review of Scientific Instruments*, 81(10):10D741, 10 2010.

[22] G. R. McKee, R. J. Fonck, D. K. Gupta, D. J. Schlossberg, M. W. Shafer, C. Holland, and G. Tynan. Turbulence velocimetry of density fluctuation imaging data. *Review of Scientific Instruments*, 75(10):3490–3492, 2004.

[23] D. D. Truong, G. R. McKee, Z. Yan, K. Jaehnig, G. R. Winz, R. J. Fonck, and B. Geiger. Ion temperature and rotation fluctuation measurements with ultra-fast charge exchange recombination spectroscopy (UF-CHERS) in the DIII-D tokamak. *Review of Scientific Instruments*, 92(5):053513, 05 2021.

[24] K. H. Burrell and J. D. Callen. Turbulence-driven flow dynamics in general axisymmetric toroidal geometry. *Physics of Plasmas*, 28(6):062502, 06 2021.

[25] J. D. Callen, A. J. Cole, and C. C. Hegna. Toroidal flow and radial particle flux in tokamak plasmas. *Physics of Plasmas*, 16(8):082504, 08 2009.

[26] K. Ida and J.E. Rice. Rotation and momentum transport in tokamaks and helical systems. *Nuclear Fusion*, 54(4):045001, mar 2014.

[27] F.L. Hinton and M.N. Rosenbluth. The mechanism for toroidal momentum input to tokamak plasmas from neutral beams. *Physics Letters A*, 259(3):267–275, 1999.

[28] Alexei Pankin, Douglas McCune, Robert Andre, Glenn Bateman, and Arnold Kritz. The tokamak monte carlo fast ion module nubeam in the national transport code collaboration library. *Computer Physics Communications*, 159:157–184, 06 2004.

[29] Weston M. Stacey. *Neoclassical Transport*, chapter 9, pages 205–250. John Wiley & Sons, Ltd, 2005.

[30] E A Belli and J Candy. Kinetic calculation of neoclassical transport including self-consistent electron and impurity dynamics. *Plasma Physics and Controlled Fusion*, 50(9):095010, jul 2008.

[31] W. A. Houlberg, K. C. Shaing, S. P. Hirshman, and M. C. Zarnstorff. Bootstrap current and neoclassical transport in tokamaks of arbitrary collisionality and aspect ratio. *Physics of Plasmas*, 4(9):3230–3242, 09 1997.

[32] Weston M. Stacey. *Turbulent Transport*, chapter 11, pages 267–284. John Wiley & Sons, Ltd, 2005.

[33] W. Horton. Drift waves and transport. *Rev. Mod. Phys.*, 71:735–778, Apr 1999.

[34] G. R. Tynan, A. Fujisawa, and G. McKee. A review of experimental drift turbulence studies. *Plasma Physics and Controlled Fusion*, 51(11):113001, Oct 2009.

[35] H. Biglari, P. H. Diamond, and P. W. Terry. Influence of sheared poloidal rotation on edge turbulence. *Physics of Fluids B: Plasma Physics*, 2(1):1–4, 1990.

[36] K. H. Burrell. Effects of E×B velocity shear and magnetic shear on turbulence and transport in magnetic confinement devices. *Physics of Plasmas*, 4(5):1499–1518, 05 1997.

[37] H. Y. Yuh, S. M. Kaye, F. M. Levinton, E. Mazzucato, D. R. Mikkelsen, D. R. Smith, R. E. Bell, J. C. Hosea, B. P. LeBlanc, J. L. Peterson, H. K. Park, and W. Lee. Suppression of electron temperature gradient turbulence via negative magnetic shear in nstx. *Phys. Rev. Lett.*, 106:055003, Feb 2011.

[38] S. D. Scott, P. H. Diamond, R. J. Fonck, R. J. Goldston, R. B. Howell, K. P. Jaehnig, G. Schilling, E. J. Synakowski, M. C. Zarnstorff, C. E. Bush, E. Fredrickson, K. W. Hill, A. C. Janos, D. K. Mansfield, D. K. Owens, H. Park, G. Pautasso, A. T. Ramsey, J. Schivell, G. D. Tait, W. M. Tang, and G. Taylor. Local measurements of correlated momentum and heat transport in the tftr tokamak. *Phys. Rev. Lett.*, 64:531–534, Jan 1990.

[39] M. Yoshida, Y. Kamada, H. Takenaga, Y. Sakamoto, H. Urano, N. Oyama, and G. Matsunaga. Role of pressure gradient on intrinsic toroidal rotation in tokamak plasmas. *Phys. Rev. Lett.*, 100:105002, Mar 2008.

[40] P.H. Diamond, C.J. McDevitt, Ö.D. Gürcan, T.S. Hahm, W. X. Wang, E.S. Yoon, I. Holod, Z. Lin, V. Naulin, and R. Singh. Physics of non-diffusive turbulent transport of momentum and the origins of spontaneous rotation in tokamaks. *Nuclear Fusion*, 49(4):045002, mar 2009.

[41] Sanae-I. Itoh. Anomalous viscosity due to drift wave turbulence. *Physics of Fluids B: Plasma Physics*, 4(4):796–803, 04 1992.

[42] I. Holod and Z. Lin. Gyrokinetic particle simulations of toroidal momentum transport. *Physics of Plasmas*, 15(9):092302, 09 2008.

[43] P. H. Diamond, C. J. McDevitt, Ö. D. Gürcan, T. S. Hahm, and V. Naulin. Transport of parallel momentum by collisionless drift wave turbulence. *Physics of Plasmas*, 15(1):012303, 01 2008.

[44] R M McDermott, C Angioni, R Dux, A Gude, T Pütterich, F Ryter, G Tardini, and the ASDEX Upgrade Team. Effect of electron cyclotron resonance heating (ecrh) on toroidal rotation in asdex upgrade h-mode discharges. *Plasma Physics and Controlled Fusion*, 53(3):035007, jan 2011.

[45] T. S. Hahm, P. H. Diamond, O. D. Gurcan, and G. Rewoldt. Nonlinear gyrokinetic theory of toroidal momentum pinch. *Physics of Plasmas*, 14(7):072302, 07 2007.

[46] Ö. D. Gürcan, P. H. Diamond, and T. S. Hahm. Turbulent equipartition and homogenization of plasma angular momentum. *Phys. Rev. Lett.*, 100:135001, Apr 2008.

[47] A. G. Peeters, C. Angioni, and D. Strintzi. Toroidal momentum pinch velocity due to the coriolis drift effect on small scale instabilities in a toroidal plasma. *Phys. Rev. Lett.*, 98:265003, Jun 2007.

[48] C F B Zimmermann, R M McDermott, E Fable, C Angioni, B P Duval, R Dux, A Salmi, U Stroth, T Tala, G Tardini, T Pütterich, the ASDEX Upgrade, and EUROfusion MST1 Teams. Analysis and modelling of momentum transport based on nbi modulation experiments at asdex upgrade. *Plasma Physics and Controlled Fusion*, 64(5):055020, apr 2022.

[49] Y. Ohtani, M. Yoshida, M. Honda, and E. Narita. Application of transient transport analysis method for modulation experiment. *AIP Advances*, 11(8):085306, 08 2021.

[50] Jong-Kyu Park, Ronald E. Bell, Stanley M. Kaye, Wayne M. Solomon, Benoit P. LeBlanc, Ahmed Diallo, Jonathan E. Menard, and Shigeyuki Kubota and. Intrinsic rotation generation in NSTX ohmic h-mode plasmas. *Nuclear Fusion*, 53(6):063012, may 2013.

[51] J.E. Rice, J. Citrin, N.M. Cao, P.H. Diamond, M. Greenwald, and B.A. Grierson. Understanding loc/soc phenomenology in tokamaks. *Nuclear Fusion*, 60(10):105001, sep 2020.

[52] B P Duval, A Bortolon, A Karpushov, R A Pitts, A Pochelon, and A Scarabosio and. Bulk plasma rotation in the TCV tokamak in the absence of external momentum input. *Plasma Physics and Controlled Fusion*, 49(12B):B195–B209, nov 2007.

[53] J. E. Rice, M. J. Greenwald, Y. A. Podpaly, M. L. Reinke, P. H. Diamond, J. W. Hughes, N. T. Howard, Y. Ma, I. Cziegler, B. P. Duval, P. C. Ennever, D. Ernst, C. L. Fiore, C. Gao, J. H. Irby, E. S. Marmar, M. Porkolab, N. Tsujii, and S. M. Wolfe. Ohmic energy confinement saturation and core toroidal rotation reversal in alcator c-mod plasmas. *Physics of Plasmas*, 19(5):056106, 2012.

[54] J. E. Rice, I. Cziegler, P. H. Diamond, B. P. Duval, Y. A. Podpaly, M. L. Reinke, P. C. Ennever, M. J. Greenwald, J. W. Hughes, Y. Ma, E. S. Marmar, M. Porkolab, N. Tsujii, and S. M. Wolfe. Rotation reversal bifurcation and energy confinement saturation in tokamak ohmic l-mode plasmas. *Phys. Rev. Lett.*, 107:265001, Dec 2011.

[55] A. Lebschy, R.M. McDermott, C. Angioni, B. Geiger, D. Prisiazhniuk, M. Cavedon, G.D. Conway, R. Dux, M.G. Dunne, A. Kappatou, T. Pütterich, U. Stroth, E. Viezzer, and the ASDEX Upgrade Team. Measurement of the complete core plasma flow across the loc–soc transition at asdex upgrade. *Nuclear Fusion*, 58(2):026013, dec 2017.

[56] N. M. Cao, J. E. Rice, P. H. Diamond, A. E. White, M. A. Chilenski, P. C. Ennever, J. W. Hughes, J. Irby, M. L. Reinke, P. Rodriguez-Fernandez, and Alcator C-Mod Team. Evidence and modeling of turbulence bifurcation in L-mode confinement transitions on Alcator C-Mod. *Physics of Plasmas*, 27(5):052303, 05 2020.

[57] J E Rice. Experimental observations of driven and intrinsic rotation in tokamak plasmas. *Plasma Physics and Controlled Fusion*, 58(8):083001, jul 2016.

[58] Z. Yan, M. Xu, P. H. Diamond, C. Holland, S. H. Müller, G. R. Tynan, and J. H. Yu. Intrinsic rotation from a residual stress at the boundary of a cylindrical laboratory plasma. *Phys. Rev. Lett.*, 104:065002, Feb 2010.

[59] Z. Yan, G. R. Tynan, C. Holland, M. Xu, S. H. Müller, and J. H. Yu. Shear flow and drift wave turbulence dynamics in a cylindrical plasma device. *Physics of Plasmas*, 17(3):032302, 03 2010.

[60] S. H. Müller, J. A. Boedo, K. H. Burrell, J. S. deGrassie, R. A. Moyer, D. L. Rudakov, and W. M. Solomon. Experimental investigation of the role of fluid turbulent stresses and edge plasma flows for intrinsic rotation generation in diii-d h-mode plasmas. *Phys. Rev. Lett.*, 106:115001, Mar 2011.

[61] J. L. Luxon, T. C. Simonen, R. D. Stambaugh, and DIII-D Team. Overview of the diii-d fusion science program. *Fusion Science and Technology*, 48(2):807–827, 2005.

[62] Laszlo Bardoczi, Robert Haye, E Strait, Nikolas Logan, Sterling Smith, Nathan Richner, and James Callen. Direct preemptive stabilization of $m, n = 2, 1$ neoclassical tearing modes by electron cyclotron current drive in the diii-d low-torque iter baseline scenario. *Nuclear Fusion*, 63, 08 2023.

[63] Raymond P. Seraydarian and Keith H. Burrell. Multichordal charge-exchange recombination spectroscopy on the DIII-D tokamak. *Review of Scientific Instruments*, 57(8):2012–2014, 08 1986.

[64] D. M. Ponce-Marquez, B. D. Bray, T. M. Deterly, C. Liu, and D. Eldon. Thomson scattering diagnostic upgrade on DIII-Da). *Review of Scientific Instruments*, 81(10):10D525, 10 2010.

[65] B. Tobias, C. W. Domier, T. Liang, X. Kong, L. Yu, G. S. Yun, H. K. Park, I. G. J Classen, J. E. Boom, A. J. H. Donné, T. Munsat, R. Nazikian, M. Van Zeeland, R. L. Boivin, and Jr. Luhmann, N. C. Commissioning of electron cyclotron emission imaging instrument on the DIII-D tokamak and first dataa). *Review of Scientific Instruments*, 81(10):10D928, 10 2010.

[66] E. J. Strait. Magnetic diagnostic system of the DIII-D tokamak. *Review of Scientific Instruments*, 77(2):023502, 02 2006.

[67] R. J. Fonck, P. A. Duperrex, and S. F. Paul. Plasma fluctuation measurements in tokamaks using beam-plasma interactions. *Review of Scientific Instruments*, 61(11):3487–3495, 11 1990.

[68] R. J. Fonck, G. Cosby, R. D. Durst, S. F. Paul, N. Bretz, S. Scott, E. Synakowski, and G. Taylor. Long-wavelength density turbulence in the tftr tokamak. *Phys. Rev. Lett.*, 70:3736–3739, Jun 1993.

[69] D. R. Smith, H. Feder, R. Feder, R. J. Fonck, G. Labik, G. R. Mc-Kee, N. Schoenbeck, B. C. Stratton, I. Uzun-Kaymak, and G. Winz. Overview of the beam emission spectroscopy diagnostic system on the National Spherical Torus Experimenta). *Review of Scientific Instruments*, 81(10):10D717, 10 2010.

[70] X. Qin, G. McKee, Z. Yan, B. Geiger, R. Ke, K. Jaehnig, L. Morton, Y. Wu, T. Wu, and M. Xu. Integrated 2D beam emission spectroscopy diagnostic at the Huan-Liuqi-2A (HL-2A) tokamak. *Review of Scientific Instruments*, 93(10):103535, 10 2022.

[71] Jr. Kriete, David M. *Influence of Applied Magnetic Perturbations on Turbulence-Flow Dynamics Across the L-H Transition in the DIII-D Tokamak*. PhD thesis, University of Wisconsin-Madison, 2020. Copyright - Database copyright ProQuest LLC; ProQuest does not claim copyright in the individual underlying works; Last updated - 2020-11-02.

[72] R. J. Fonck, R. Ashley, R. Durst, S. F. Paul, and G. Renda. Low-noise photodiode detector for optical fluctuation diagnostics. *Review of Scientific Instruments*, 63(10):4924–4926, 10 1992.

[73] G. McKee, R. Ashley, R. Durst, R. Fonck, M. Jakubowski, K. Tritz, K. Burrell, C. Greenfield, and J. Robinson. The beam emission spectroscopy diagnostic on the DIII-D tokamak. *Review of Scientific Instruments*, 70(1):913–916, 01 1999.

[74] G. Cosby. *Elimination of Common-mode Plasma-induced Beam Density Fluctuations from BES Turbulence Measurements*. PhD thesis, University of Wisconsin-Madison, 1992.

[75] M. W. Shafer, R. J. Fonck, G. R. McKee, and D. J. Schlossberg. Spatial transfer function for the beam emission spectroscopy diagnostic on diii-d. *Review of Scientific Instruments*, 77(10):10F110, 2006.

[76] D. Truong. *Experimental Study of Turbulent Multi-field Ion Fluctuations with Ultra Fast Charge Exchange Recombination Spectroscopy in the DIII-D Tokamak*. PhD thesis, University of Wisconsin-Madison, 2020.

[77] Georges Quénot, Jaroslaw Pakleza, and Tomasz Kowalewski. Particle Image Velocimetry with Optical Flow. *Experiments in Fluids*, 25(3):177–189, 1998.

[78] D. M. Kriete, G. R. McKee, R. J. Fonck, D. R. Smith, G. G. Whelan, and Z. Yan. Extracting the turbulent flow-field from beam emission spectroscopy images using velocimetry. *Review of Scientific Instruments*, 89(10):10E107, 09 2018.

[79] D. D. Truong, R. J. Fonck, and G. R. McKee. Optimization and application of cooled avalanche photodiodes for spectroscopic fluctuation measurements with ultra-fast charge exchange recombination spectroscopy. *Review of Scientific Instruments*, 87(11):11E551, 09 2016.

[80] C. Fenzi, G. R. McKee, R. J. Fonck, K. H. Burrell, T. N. Carlstrom, and R. J. Groebner. Effect of ion grad-B drift direction on density fluctuation poloidal flow and flow shear. *Physics of Plasmas*, 12(6):062307, 05 2005.

[81] T Stoltzfus-Dueck. Intrinsic rotation in axisymmetric devices. *Plasma Physics and Controlled Fusion*, 61(12):124003, nov 2019.

[82] Weston M. Stacey and Brian A. Grierson. Interpretation of rotation and momentum transport in the diii-d edge plasma and comparison with neoclassical theory. *Nuclear Fusion*, 54(7):073021, may 2014.

[83] Frédéric Schwander, Eric Serre, Hugo Bufferand, Guido Ciraolo, and Philippe Ghendrih. Global fluid simulations of edge plasma turbulence in tokamaks: a review. *Computers Fluids*, 270:106141, 2024.

[84] R.J. Hawryluk. An empirical approach to tokamak transport. In B. Coppi, G.G. Leotta, D. Pfirsch, R. Pozzoli, and E. Sindoni, editors, *Physics of Plasmas Close to Thermonuclear Conditions*, pages 19–46. Pergamon, 1981.